



저작자표시-비영리-변경금지 2.0 대한민국

이용자는 아래의 조건을 따르는 경우에 한하여 자유롭게

- 이 저작물을 복제, 배포, 전송, 전시, 공연 및 방송할 수 있습니다.

다음과 같은 조건을 따라야 합니다:



저작자표시. 귀하는 원저작자를 표시하여야 합니다.



비영리. 귀하는 이 저작물을 영리 목적으로 이용할 수 없습니다.



변경금지. 귀하는 이 저작물을 개작, 변형 또는 가공할 수 없습니다.

- 귀하는, 이 저작물의 재이용이나 배포의 경우, 이 저작물에 적용된 이용허락조건을 명확하게 나타내어야 합니다.
- 저작권자로부터 별도의 허가를 받으면 이러한 조건들은 적용되지 않습니다.

저작권법에 따른 이용자의 권리는 위의 내용에 의하여 영향을 받지 않습니다.

이것은 [이용허락규약\(Legal Code\)](#)을 이해하기 쉽게 요약한 것입니다.

[Disclaimer](#)

Doctor of Philosophy

**Enhancement of Functional Properties in Complex Oxides
via Spatial-Inversion Symmetry Control**

Department of Physics and Energy Harvest-Storage Research Center (EHSRC),

University of Ulsan, Ulsan 44610, Republic of Korea

Muhammad Sheeraz

Enhancement of Functional Properties in Complex Oxides via Spatial-Inversion Symmetry Control

Supervisor: Tae Heon Kim

A Dissertation submitted to the Graduate School of the University of Ulsan in
partial Fulfillment of the requirements for the Degree of

Doctor of Philosophy

February 2021

by

Muhammad Sheeraz

Department of Physics, and Energy Harvest-Storage Research Center (EHSRC),

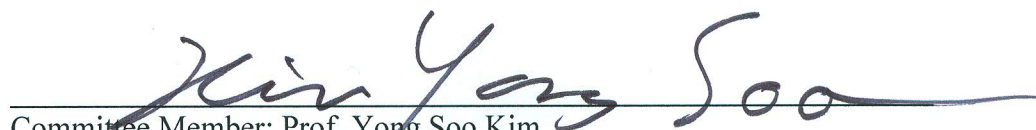
University of Ulsan, Ulsan 44610, Republic of Korea

Enhancement of Functional Properties in Complex Oxides via Spatial-Inversion Symmetry Control

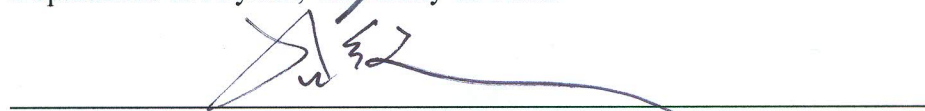
This is to declare that the dissertation
Submitted by Muhammad Sheeraz is approved officially.



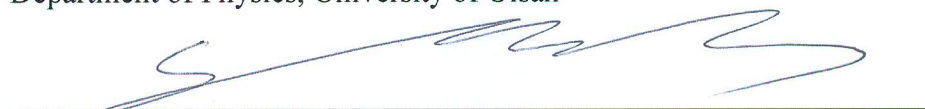
Committee Chair: Prof. Young-Han Shin
Department of Physics, University of Ulsan



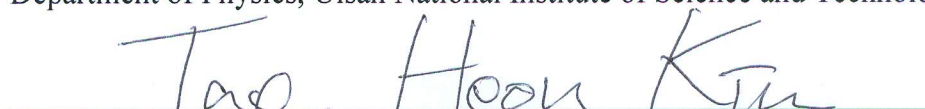
Committee Member: Prof. Yong Soo Kim
Department of Physics, University of Ulsan



Committee Member: Prof. Sanghoon Kim
Department of Physics, University of Ulsan



Committee Member: Prof. Yoon Seok Oh
Department of Physics, Ulsan National Institute of Science and Technology



Committee Member and Supervisor: Prof. Tae Heon Kim
Department of Physics, University of Ulsan

Department of Physics, and Energy Harvest-Storage Research Center (EHSRC),

University of Ulsan, Ulsan 44610, Republic of Korea

February 2021

Abstract

Spatial inversion symmetry is defined as a single point in a crystal symmetry where, upon placing a mirror, its reflection will look the same as the original.

The control of the inversion symmetry breaking is of great importance for enhancing the functional properties in oxide materials due to the fundamental scientific development and promising device applications. In the case of complex oxides, manipulating the inversion symmetry can lead to enhancement of the ionic displacement (spontaneous electric-polarization) upon the structural phase transition, resulting in an enhancement in the functional properties, like piezoelectricity, ferroelectricity, flexoelectricity, and multi-ferroelectricity. In this thesis, using various complex oxide materials using different experimental approaches such as anion doping, stress at the grain boundary of two different materials, interfacial strain to enhance functional properties in the complex oxides with controlled spatial inversion symmetry.

We controlled the spatial inversion symmetry in the perovskite $\text{Pb}(\text{Zr}, \text{Ti})\text{O}_3$ via quantitatively sulfur substitution at the apical oxygen site. By substituting the sulfur at the apical oxygen site, a structural phase transition from the monoclinic $\text{Pb}(\text{Zr}, \text{Ti})\text{O}_3$ to tetragonal $\text{Pb}(\text{Zr}, \text{Ti})\text{O}_{3-x}\text{S}_x$ is noticed in the reciprocal space mapping (RSM), resulting in an enhancement in ferroelectricity. The origin of the enhanced ferroelectric polarization is explained via Raman spectroscopy. The sulfur (S) makes a strong covalent bond with the titanium (Ti) element (Ti 3d-S 3p) compared with the Ti 3d-O 2p bonding due to the lower electronegativity of the sulfur element than the oxygen atom. The strong covalency of the Ti-S (apical) bonding lifted the spatial inversion symmetry uniformly in PZT oxysulfide.

In this study, by adding the ferroelectric $\text{Bi}_{1/2}(\text{Na}_{0.78},\text{K}_{0.22})_{1/2}\text{TiO}_3$ (BNKT) particles (volume percent fraction) to the relaxor $0.72\text{Bi}_{1/2}\text{Na}_{1/2}\text{TiO}_3\text{-}0.28\text{SrTiO}_3$ (BNT-28ST), the spatial inversion symmetry in perovskite BNT-28ST is uniformly lifted resulting in a high piezoelectric response at a low applied field in the BNT-28ST/BNKT ceramic composite. At a given applied electric field in BNT-28ST/BNKT composite, the BNKT ferroelectric particles compressively stressed the BNT-28ST relaxor ceramic and lifted the spatial inversion symmetry. Consequently, a structural transition from the pseudocubic BNT-28ST to tetragonal is identified with the spatial inversion symmetry controlled, leading to the high piezoelectric response under the low applied electric field in the BNT-based ceramic composite.

In the Al-doped SrMnO_3 , we aimed to produce the ferroelectric polarization in 6H-hexagonal SrMnO_3 ceramics with controlled spatial inversion symmetry. The origin of the ferroelectric/polar-ordering in the hexagonal oxides (like YMnO_3) is strongly connected to the buckling/tilting of a trigonal MnO_5 bipyramid rather than the off-centering displacement in perovskites. Herein, we constructed the hexagonal SrAl_2O_4 grains locally in the proximity to the 4H-hexagonal SrMnO_3 grains by doping the Aluminum (Al) to the SrMnO_3 ceramic. Using the interfacial strain mechanism, a 6H-hexagonal polymorph is realized in the SrMnO_3 polymorph identified in the x-ray diffraction analysis and Raman spectroscopy results. We plan to generate the ferroelectric ordering by octahedral tilting in a 6H-hexagonal SrMnO_3 oxide. Then, the inversion symmetry in 6H-hexagonal SrMnO_3 is expected to be broken and generate a new polar symmetry.

A free-standing epitaxial SrRuO_3 (SRO) membrane with nanoscale thickness is synthesized. The heteroepitaxial sacrificial layer of SrCuO_2 (SCO) followed by an encapsulated SRO film is grown on the SrTiO_3 (001) substrate via pulsed-laser deposition (PLD) technique. A

free-standing SRO epitaxial-membrane is attained by chemical etching of the sacrificial SCO layer in the acidic potassium chloride (KCl) solution. The structural, chemical, surface, and electrical characterization of the SrRuO₃ epitaxial membrane were demonstrated via x-ray diffraction (XRD), scanning electron microscopy (SEM) measurements, Atomic force microscopy (AFM), and the four-prob method.

A better understanding of the enhanced functional properties in complex oxides can play a promising role in device applications like non-volatile memories, actuators, and flexible electronics.

Table of Contents

Abstract.....	i
Table of Contents.....	iv
List of Figures.....	vii
List of Tables.....	xiii
Chapter 1. Introduction	1
1.1. Spatial inversion symmetry in condensed matters.....	1
1.2. Significance of inversion-symmetry control in complex oxides.....	2
1.3. How to control spatial inversion symmetry	5
1.3.1. Anion doping/substitution.....	5
1.3.2. Inversion symmetry breaking induced by ferroelectric seeds	5
1.3.3. Misfit strain in the proximity of grain boundaries	6
1.3.4. Engineering of flexibility (stretching, bending) in freestanding membranes	6
1.4. Motivation: Enhancing functional properties in complex oxides	6
1.4.1. Proper ferroelectricity in oxysulfides.....	6
1.4.2. High piezoelectricity at low field.....	8
1.4.3. Improper ferroelectricity in hexagonal materials.....	11
1.4.4. Control of electrical conductivity in SrRuO ₃ free-standing films	13
References.....	14
Chapter 2. Experimental detail (method)	16
2.1. Synthesis of the perovskite oxysulfides by method A	16
2.2. Synthesis of the perovskite oxysulfides by method B	18
2.3. Fabrication of the relaxor/ferroelectric composites	21

2.4. Al-doped SrMnO ₃ ceramics by solid-state reaction route	23
2.5. Fabrication of free-standing membranes by chemical etching of sacrificial layers ..	25
References.....	29
Chapter 3. Enhanced ferroelectricity in perovskite oxysulfides.....	30
3.1. Perovskite oxysulfides ABO _{3-x} S _x	30
3.2. Inversion symmetry control by sulfur doping.....	30
3.3. Challenges and realization of perovskite oxysulfides.....	31
3.4. Theoretical predictions of a sulfurization effect on Pb(Zr _{0.5} Ti _{0.5})O ₃	33
3.5. Experimental methods.....	36
3.6. Characterization of the sulfurized perovskites	38
3.7. Results: Enhancement of ferroelectricity and Bandgap reduction.....	46
3.8. Discussion: Origin of enhanced ferroelectricity in perovskite oxysulfides	50
3.9. Implications.....	52
References.....	53
Chapter 4. Stress-driven high electro-strain in BNT-based ceramics at a low applied field	56
4.1. Bismuth based perovskites oxides.....	56
4.2. Inversion symmetry breaking by ferroelectric particles.....	57
4.3. Sample characterization	57
4.4. Results: Explanation of high electro-strain at a low driving field.....	61
4.5. Discussion: Strain coupling mechanism in BNT-based composite ceramics	64
4.6. Device applications	71
References.....	72
Chapter 5. Realization of 6H-hexagonal polymorph in Al-doped SrMnO₃ oxide	75
5.1. Crystallographic structure of SrMnO ₃ oxide and structural phase transition in SrMnO ₃	75

5.2. Hypothetical realization of 6H-hexagonal polymorph.....	77
5.3. Inversion symmetry manipulation by interfacial strain.....	79
5.4. Results: Structural and chemical analyses	79
5.5. Discussion: Origin of the realized 6H-hexagonal polymorph in our Al-doped SrMnO ₃ ceramics.....	86
5.6. Further interest	91
References	92
Chapter 6. Fabrication of freestanding single-crystalline perovskite films.....	95
6.1. Importance of freestanding films	95
6.2. Inversion symmetry breaking by mechanical stress.....	95
6.3. Strategy.....	96
6.4. Experimental methods.....	97
6.5. Results.....	100
6.6. Discussion	102
6.7. Potential applications	102
References	103
Chapter 7. Summary	105
Appendix A: Experimental methods.....	108
Appendix B: Manual for x-ray diffraction techniques in the beamline of the Pohang Accelerator Laboratory.....	117
Publication List	132
Patent List.....	123
Acknowledgments	124

List of Figures

Figure 1.1. Spatial inversion symmetry for the up and down electric polarization in a single unit perovskite structure.	2
Figure 1.2. Schematic of the significance of the inversion symmetry control.	4
Figure 1.3. Enhancement of ferroelectric polarization via sulfur substitution at the apical oxygen site. (a) A perovskite material, (b) inversion symmetry breaking in perovskite by sulfur substitution forming the oxysulfide.....	8
Figure 1.4. Schematic representation of the symmetry breaking in relaxor-ferroelectric composites. (a) Relaxor ferroelectric composite at zero electric field, (b) at a maximum electric field.....	10
Figure 1.5. Schematic view of hexagonal YMnO ₃ structure. The Atomic displacement from the non-ferroelectric (centrosymmetric) ordering to the ferroelectric (non-centrosymmetric) structure is shown by arrows.....	12
Figure 2.1. Method A: Solution synthesis and thin-film fabrication. (a) Synthesis of the thiourea solution. (b) Fabrication of the sulfurized Pb(Zr _{0.52} Ti _{0.48})O ₃ using the top layer thiourea solution.	17
Figure 2.2. Method B: Control of sulfur-doping level in PZT oxysulfide Pb(Zr _{0.52} Ti _{0.48})O _{3-x} S _x . (a) Synthesis technique of the Pb(Zr _{0.52} Ti _{0.48})O _{3-x} S _x oxysulfide using thiourea powder at increasing mole concentration. (b) The deposition of Pb(Zr _{0.52} Ti _{0.48})O _{3-x} S _x oxysulfide on the SrRuO ₃ (10 nm, bottom electrode)/SrTiO ₃ (001).....	19
Figure 2.3. Cross-sectional images of the (a) pure PZT and (b) sulfur doped PZT (PZT-xS, x = 0.02).....	19
Figure 2.4. The topochemical microstructural conversion of the NBiT15 particles of the structure plate-type BNKT particles.....	22
Figure 2.5. The schematic illustration of the achieved 6H SrMnO ₃ polymorph via solid-state reaction method.	25
Figure 2.6. Preparation of the aqueous solution of KI (8 mg) + HCl (10 ml) + H ₂ O (100 ml). (b) Etching of the sacrificial layer (LSMO or SCO) via the aqueous solution of KI (8 mg) + HCl (10 ml) + H ₂ O (100 ml) and then the SrRuO ₃ membrane is transferred to the other substrate for other measurements.....	28

Figure 3.1. Perovskite oxysulfides, the sulfur substitution at the apical or equatorial oxygen position.	30
Figure 3.2. Theoretical calculations of the sulfurization effect on $\text{Pb}(\text{Zr}_{0.5}\text{Ti}_{0.5})\text{O}_3$. (a) Atomic structure of tetragonal $\text{Pb}(\text{Zr}_{0.5}\text{Ti}_{0.5})\text{O}_3$ with a uniform distribution of Ti and Zr. Three distinguishable oxygen sites relative to Ti are denoted. (b) The variations of the c/a ratio and the bandgap (E_g) with PBEsol and HSE06 exchange-correlation functionals. (c) The spontaneous polarization P along the z -direction at the sulfur substitution ratio $N_S/(N_O + N_S)$ of tetragonal $\text{Pb}(\text{Zr}_{0.5}\text{Ti}_{0.5})\text{O}_{3-x}\text{S}_x$	35
Figure 3.3. Band structure and density of states calculation. (a) and (b) The band structures of the tetragonal $\text{Pb}(\text{Zr}_{0.5}\text{Ti}_{0.5})\text{O}_3$ and oxysulfide $\text{Pb}(\text{Zr}_{0.5}\text{Ti}_{0.5})\text{O}_{3-x}$ ($x = 0.25$). (c) and (d) The total density of states and atomic-orbital projected density of states for tetragonal $\text{Pb}(\text{Zr}_{0.5}\text{Ti}_{0.5})\text{O}_3$ and oxysulfide $\text{Pb}(\text{Zr}_{0.5}\text{Ti}_{0.5})\text{O}_{3-x}\text{S}_x$ ($x = 0.25$). The Fermi energy is taken to be zero.....	36
Figure 3.4. Crystallinity and elemental analysis of a sulfurized $\text{Pb}(\text{Zr}_{0.52}\text{Ti}_{0.48})\text{O}_3$ film on SrRuO_3 (10 nm)/ SrTiO_3 (001) substrate. (a) High-resolution transmission electron microscopy image (HRTEM) of a sulfurized PZT film grown on a $\text{SrRuO}_3/\text{SrTiO}_3$ (001) substrate (scale bar: 10 nm), (b) SAED pattern of the PZT at the interface, (c) the dotted yellow color line represents the film thickness through which the composition analysis is carried out. (d-g) Elemental map analysis of the O, Pb, Ru, and Sr, respectively.	39
Figure 3.5. The structure characterization of the pure and sulfurized PZT films on SrRuO_3 (10 nm)/ SrTiO_3 (001) substrate. (a) Out-of-plane θ - 2θ XRD pattern of pure PZT and sulfurized PZT on SRO/STO substrate. (b) and (c) The enlarged (001) and (002) peaks of pure and sulfurized PZT films.	40
Figure 3.6. X-ray photoelectron spectroscopy (XPS) measurements of a sulfurized $\text{Pb}(\text{Zr}_{0.52}\text{Ti}_{0.48})\text{O}_3$ film. (a) The S K-edge XPS spectrum of a sulfurized PZT film. The red and blue solid curves correspond to the fitting curves of the oxidation states of S^{2-} and S^{4+} , respectively. The solid red curve represents the sulfur (S^{2-}) substitution to an oxygen site, while the blue solid curve shows the presence of SO_2 molecule on the surface of the film. (b) The elemental composition as a function of the depth for the sulfurized PZT film grown on the Pt(111)/ $\text{TiO}_2/\text{SiO}_2/\text{Si}(100)$ substrate. (c) The O K-	

edge XPS spectra of pure and sulfurized PZT films. (d) Electron probe micro-analyzer (EPMA) measurement of the pure and sulfurized PZT film grown on the Pt(111)/TiO ₂ /SiO ₂ /Si(100) substrate.	43
Figure 3.7. The structural analyses of PZT oxysulfide (Pb(Zr _{0.52} Ti _{0.48})O _{3-x} S _x) films on SrRuO ₃ /SrTiO ₃ substrates. (a-e) High-resolution RSMs of sulfur-doped PZT (Pb(Zr _{0.52} Ti _{0.48})O _{3-x} S _x , where $x = 0.01, 0.02, 0.03, 0.04,$ and 0.05) films around the (103) Bragg peaks of SrTiO ₃ (001) substrate. (f) The L -scan profiles (along the red dotted line in Figure 3.7(a) at $H = 0.96$ in the RSMs of Figures 3.7(a)-(e)). (g) The sulfur-doping level dependence of the in-plane (a_{PZT}) and out-of-plane (c_{PZT}) lattice parameters extracted from the RSM plots.	45
Figure 3.8. Enhancement of ferroelectric polarization in sulfurized Pb(Zr _{0.52} Ti _{0.48})O ₃ films. (a) Polarization (P)-electric field (E) hysteresis loops of pure and sulfurized PZT films on SrRuO ₃ /SrTiO ₃ (001) substrate. (b)-(e) Piezoresponse force microscopy (PFM) images, (b) and (c) out of plane amplitude (R) and (d) and (e) phase (θ) mapping images of the pure and sulfurized PZT films, respectively at the DC bias of ± 7 V. (f) The comparison of the polarization hysteresis loops against the electric field of the pure PZT and PZT oxysulfide ($x = 0.01, 0.02, 0.03, 0.04, 0.05$) on the SrRuO ₃ (10 nm)/SrTiO ₃ substrate. (g) Remnant polarization of PZT oxysulfide as increasing sulfur doping level measured at 600 kV/cm.	47
Figure 3.9. (a) Measuring setup for the polarization in sulfurized PbTiO ₃ films. (b) Polarization (P)-electric field (E) hysteresis loops of pure and sulfurized PTO films on Pt(111)/TiO ₂ /SiO ₂ /Si(100) substrate.	48
Figure 3.10. The electronic band-gap measurements of pure and sulfurized Pb(Zr _{0.52} Ti _{0.48})O ₃ films. (a) The bandgap measurement of pure and sulfurized PZT films on SrRuO ₃ /SrTiO ₃ (001) substrates using ellipsometry. Here, $(E\alpha)^2$, where E and α is the photon energy and the absorption coefficient, respectively, was plotted as a function of the photon energy (eV). (b) ultraviolet-visible spectrometry of pure and sulfurized PZT films on fluorine-doped tin oxide (FTO) coated glass substrates.	49
Figure 3.11. The Raman spectroscopy of pure and sulfurized Pb(Zr _{0.52} Ti _{0.48})O ₃ films. Room temperature Raman spectra of pure and sulfurized PZT films in the wavenumber	

	ranges (a) 25 to 400 cm^{-1} and (b) 470 to 670 cm^{-1} . (c) Schematic demonstration of the structural transition via sulfur doping in PZT films.....	51
Figure 4.1.	The FE–SEM images of (a) $\text{Na}_{0.5}\text{Bi}_{4.5}\text{Ti}_4\text{O}_{15}$ (NBT15) particles (b) plate–type $\text{Bi}_{1/2}(\text{Na}_{0.78}\text{K}_{0.22})_{1/2}\text{TiO}_3$ (BNKT) perovskite particles, XRD patterns of (c) NBT15 particles and (d) plate–type BNKT particles.....	58
Figure 4.2.	(a) XRD patterns of the of BNT–28ST/BNKT (0, 5, 10, and 15 vol.%) composites and pure BNKT ceramic in the 2θ range of 10–70°, (b) the enlarge (200) peak of the corresponding composites and pure BNKT. Figure 4.2 FE–SEM images of BNT–28ST/BNKT (0, 5, 10, and 15 vol.%) composites. The small size BNT–28ST relaxor particles are surrounding the large size ferroelectric particles.	60
Figure 4.3.	(a) Polarization, (b) bipolar, and (b) unipolar strain hysteresis loops of BNT–28ST/BNKT composites (0 vol.% to 15 vol.%.). Extracted values of (d) polarization (P_{max} , P_r , and $P_{\text{max}}-P_r$), (e) coercive field (E_c), and (f) poling field (E_{pol}) with respect to plate–type BNKT content in vol.%. The bipolar and unipolar strain hysteresis loops were measured at the frequency of 0.2 Hz at room temperature. Schematic for the poling field (E_{pol}) is in the inset of Fig. 4(f). The poling field (E_{pol}) is marked with a black dashed line in all composited BNT–28ST/BNKT samples according to the schematic figure.	63
Figure 4.4.	(a) The applied electric field for two cycles as a function of time for the measured parameters. The electric–field-induced electromechanical strain of (b) ferroelectric BNKT particles and (c) relaxor BNT–28ST. (d) The difference in strain responses ($S_{FE} - S_{RE}(\%)$) extracted from the unipolar strain as a function of field, (e) the field-dependent residual (longitudinal) stress (MPa). (f) The virgin strain response of the ferroelectric BNKT plate type particles and the relaxor BNT–28ST during the first cycle of the applied electric field, (g) the collective strain response of the 10 vol.% composite sample during the first and second cycle of the applied field, and (h) calculated residual (longitudinal) stress (MPa) after poling state as a function of BNKT content (vol.%).	67
Figure 4.5.	Schematic of strain coupling mechanism (a) before poling, (b) under the applied field, and (c) after poling. The tensile strain motif in the figure (b) and (c) is presented by the red color for elongated strain and blue as a compressive strain.	70

- Figure 4.6. A schematic of a multilayer piezoelectric actuator under the electric field at zero and maximum electric field. 71
- Figure 5.1. (a) In cubic perovskite SrMnO₃ structure, only corner-sharing can be observed. (b) An alternating face- and corner-sharing can be realized in 4H-hexagonal SrMnO₃ polymorph along the c-axis. (c) In the 6H-hexagonal SrMnO₃ polymorph, the degree of corner-sharing is raised from 4H-hexagonal SrMnO₃, so that each face-sharing dimer is monitored by a corner-shared octahedron [1-3]. The schematic illustration of the SrMnO₃ polymorphs under high pressure and high temperature [7-9]. ...76
- Figure 5.2. (a) XRD patterns of pure and Al-doped SrMnO₃ ceramics with various doping concentrations (x). The powder XRD scans of the 4H SrMnO₃ (green lines), 6H SrMnO₃ (blue lines), cubic-SrMnO₃ (cyan lines), SrAl₂O₄ (black lines), and MnO₂ (purple lines) are provided for comparison [17-19]. The enlarge XRD patterns in the 2θ range from (b) 27 to 30°, (c) 32 to 34°, (d) 46 to 50°..... 81
- Figure 5.3. Rietveld refinement of XRD patterns of (a) pure SrMnO₃ and (b,c) Al-doped ($x = 0.10$, and 0.20) SrMnO₃ ceramics. The XRD fitted lines of the observed experimental (Y_{obs}), calculated (Y_{cal}), and the difference between observed and experimental ($Y_{obs}-Y_{cal}$) XRD profiles are represented by black, red, and blue lines. The Bragg position of the 4H SrMnO₃, 6H SrMnO₃, and SrAl₂O₄ are represented via purple, olive, and orange color tick lines, respectively..... 83
- Figure 5.4. The maximum XPS intensity of the Al $2p$ edges as a function of Al doping content (x). 85
- Figure 5.5. Backscattered FE-SEM surface images of the as-sintered Al-doped ($x = 0.01, 0.10$, and 0.20) SrMnO₃ ceramic pellets. The black spots (SrAl₂O₄ grains) were encircled with blue colors in the back-scattered SEM images. (b) and (d) Elemental mapping results of the Al₂O₃ (1, 10, and 20%) doped SrMnO₃ target surfaces in (a) respectively, using EDS. 86
- Figure 5.6. (a) Room-temperature Raman spectra of pure and Al-doped SrMnO₃ ceramics with various doping concentrations (x) in the wavenumber range from 200 to 900 cm⁻¹. The reference Raman spectral peaks of the 4H SrMnO₃ (green lines), SrAl₂O₄ (blue lines), and 6H BaTiO₃ (black lines) are also plotted. The enlarged Raman peaks are provided

in the wavenumber range from (b) 300 to 420 cm^{-1} , 570 to 650 cm^{-1} , and (c) 700 to 820 cm^{-1} [28,29]. 89

Figure 6.1. The preparation process of the SrCuO_2 target via a conventional solid-state reaction method. 98

Figure 6.2. (a) The x-ray diffraction (XRD) analysis of the epitaxially grown SrRuO_3 (SRO) film on the SrTiO_3 (001) substrate. (b) The thickness (23.3 nm) of the SRO film is estimated by the x-ray Reflectometry (XRR) analysis. (c) Surface topography of the as-synthesized epitaxial SRO film. 99

Figure 6.3. (a) The x-ray diffraction (XRD) analysis of the epitaxially grown SrRuO_3 (SRO)/ SrCuO_2 (SCO) on the SrTiO_3 (001) substrate. (b) The etching of the SrCuO_2 film layer and transfer of the SrRuO_3 film. (c) The XRD of the as-transferred film on a $\text{Pt}(111)/\text{TiO}_2/\text{SiO}_2/\text{Si}(100)$ substrate. A clear (001) and (002) diffraction of the transferred SRO film can be seen in Figure 6.3 (c). 101

List of Tables

Table 2.1. Descriptions of two different sulfurization methods with their pros and cons.	20
Table 5.1. The calculated lattice parameters of the 4H SrMnO ₃ , 6H SrMnO ₃ , and SrAl ₂ O ₄ phase via Rietveld refinement of XRD patterns in the pure (0.00) SrMnO ₃ and Al-doped (0.10, and 0.20) SrMnO ₃ ceramic samples.	84
Table 5.2. Total energy calculation of the 4H SrMnO ₃ , 6H SrMnO ₃ , and vacancy defects (strontium (Sr) and oxygen (O) vacancy) in each corresponding SrMnO ₃ polymorph.	90

Chapter 1

Introduction

1.1 Spatial inversion symmetry in condensed matters

Spatial inversion symmetry is defined as a single point in a crystal symmetry where, upon placing a mirror, its reflection will look the same as the original. Consider a point x in crystal symmetry, if we take its inverse ($-x$) from the center of the crystal symmetry, its reflection will be the same as point x as shown in Figure 1.1(a).

In the functional oxides, considering the perovskite unit structure, when the ionic displacement between cation and anion produce the spatial inversion symmetry is lifted in a unit cell of the perovskite, as illustrated in Figure 1.1(b). If the spatial inversion operator (i.e., electric field, E) is applied to the same perovskite unit cell, the positive (cations) and negative (oxygen) ions will change their position and as a result, the polarization direction reverses. This is only possible in non-centrosymmetric materials, while in centrosymmetric (i.e., the inversion-symmetry is un-broken) the ionic displacement is not possible.

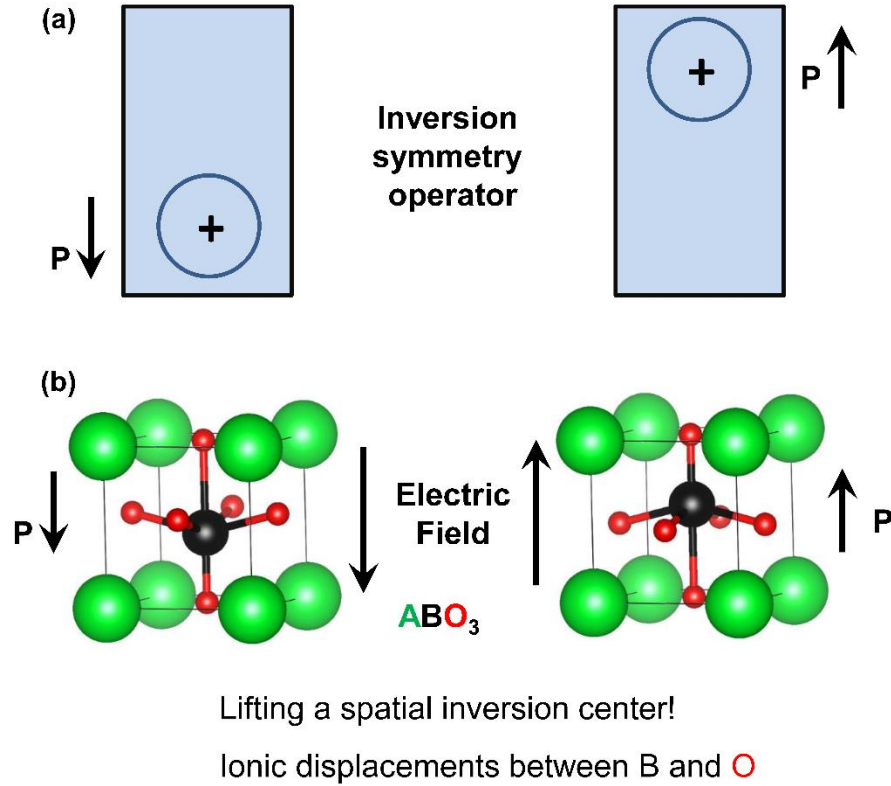


Figure 1.1 Spatial inversion symmetry for the up and down electric polarization in a single unit perovskite structure.

1.2 Significance of inversion-symmetry control in complex oxides

The inversion symmetry control in complex oxides is of significant importance for realizing the unusual functional phenomena due to the fundamental scientific development and promising device applications. The inversion symmetry breaking is an essential requirement for many technological phenomena such as piezoelectricity, ferroelectricity, flexoelectricity, multi-ferroelectricity, and photovoltaic [1,2,3]. In the case of the piezoelectricity in oxides, which arises from the breaking/manipulation of the spatial-inversion symmetry in the atomic structure, resulting in a strong coupling amongst the electric-polarization and the mechanical pressure and has initiated a broad range of practical applications in actuators, capacitors, and a transducer, etc [1,2,4].

Therefore, the creation of materials where inversion symmetry can be manipulated by design may be the ultimate route towards controlling well-known phenomena and functional properties.

In complex oxides, the octahedral-coordination of transition metal (B-sites) cations splits the $3d$ -orbitals into a degenerated states, a triplet t_{2g} ($xy/yz/xz$), and a doublet e_g ($x^2-y^2/3z^2-r^2$) symmetries [5,6]. The degeneracy of the e_g (x^2-y^2 and $3z^2-r^2$) orbitals can be broken further by lowering the crystal field symmetry. Half-filling of the e_g orbital is a key driving force for breaking the crystal symmetry in a material. In such a case, the Jahn-Teller (JT) distortion of the octahedra BO_6 coordination polyhedron producing asymmetric B-O bonds that break the ($x^2-y^2/3z^2-r^2$) degeneracy, thus changing their electron occupancy and leading to orbital ordering eventually responsible for the understanding the physics in complex oxides [5,6].

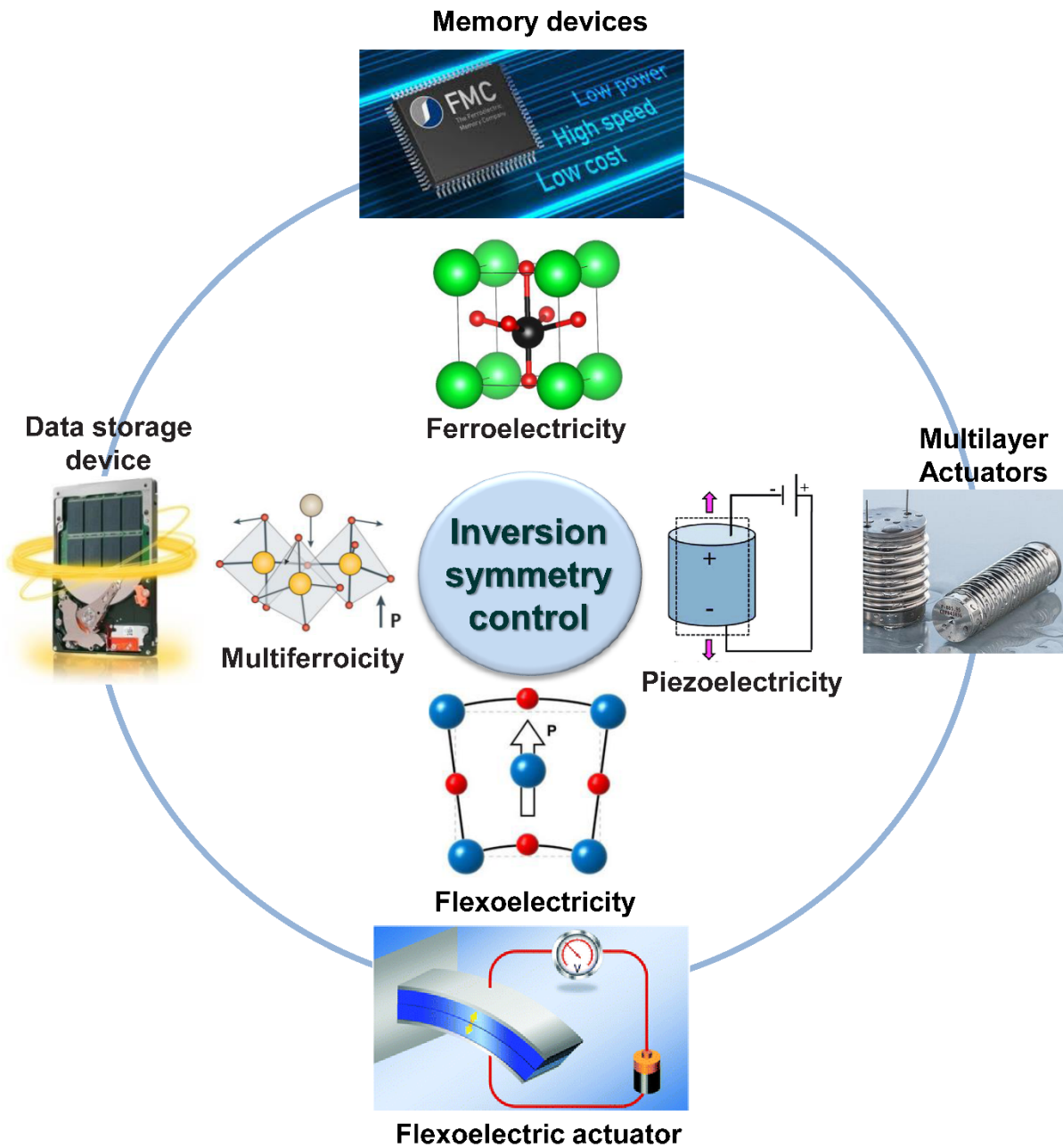


Figure 1.2 Schematic of the significance of the inversion symmetry control.

1.3 How to control spatial inversion symmetry

1.3.1 Anion doping/substitution

Anion substitution (sulfur, nitrogen, fluorine, etc) could be utilized to break/engineer the spatial-inversion symmetry in complex oxides [7-10]. To control the spatial inversion symmetry in perovskite oxides with enhancement in functional properties, anion substitution at apical oxygen is an energetically favorable position [7,8]. Considering the sulfur doping in perovskite structure (ABO_3), it has been predicted theoretically that if the sulfur is doped at the apical oxygen site, the ionic displacement between the cation and anion will be further lifted spatially due to strong covalency between the B-site cation with apical sulfur (B-S) bonding rather than B-O (apical) [7,8].

1.3.2 Inversion symmetry breaking induced by ferroelectric seeds

In complex oxides, the ferroelectric (non-centrosymmetric) seeds can be used to lift the inversion symmetry in relaxor (centrosymmetric) materials by constructing their composite [11-13]. Initially, at zero applied electric field, the relaxor-particles are surrounding in the proximity of the large-size ferroelectric seeds [11-13]. When the electric field (E) is applied, at the grain boundary of the relaxor-ferroelectric composite, the ferroelectric particles completely switched and begin to stress the relaxor particles compressively. Due to this compressive stress, the inversion symmetry of the relaxor particle breaks upon the structural transition, resulting in high functional properties [13].

1.3.3 Misfit strain in the proximity of grain boundaries

Misfit strain is the difference between the stress-free dimensions of two or more constituents that are bonded together. Misfit strain in the proximity of the grain boundaries of the complex oxides, is considered to be another alternative route to enhance the functional properties with control spatial inversion symmetry. If a system is designed, where the grains of the two isosymmetric (cubic, tetragonal, or hexagonal, etc) structures with dissimilar lattice constant co-exist. Then, at the grain boundary, one structure will stress (compressive or tensile) another due to the lattice mismatch between the two structures and can break the inversion symmetry.

1.3.4 Engineering of flexibility (stretching, bending) in freestanding membranes

Free-standing membranes with the possibility of no thickness limitation and its extreme flexibility provided opportunities to engineer the functional properties in complex oxide by controlling the spatial inversion symmetry [14-17]. Free-standing epitaxial membranes are sustainable to extreme strain (8%) and extremely flexible to bend up to 80° (bending angle) [14,15]. The extreme dynamic (biaxial and uniaxial) strain and flexibility demonstrate that the complex oxide membranes can also bear the maximum strain gradient. Therefore, a strain gradient [using the scanning probe microscope] can be applied to break the inversion symmetry of the centrosymmetric complex oxide membranes resulting in flexoelectricity [14-17].

1.4 Motivation: Enhancing functional properties in complex oxides

1.4.1 Proper ferroelectricity in oxysulfides

Proper ferroelectrics, the ferroelectrics in which there exist two equivalent polarization states due to the spatial inversion symmetry breaking. The electric dipole formed due to the ionic

displacement within the 3D network of the transition-metal oxides polyhedra (MO_6) in the perovskite structure and can be reversed upon the application of the applied electric field.

Perovskite oxysulfides $\text{ABO}_{3-x}\text{S}_x$, where the apical or equilateral oxygen atom in the octahedra of the perovskite materials is partially substituted by sulfur element [7,8]. Theoretically, it has been predicted that a ferroelectric-polarization in the perovskite oxides could be further enhanced by sulfur doping [7,8]. Due to the larger ionic radius of the sulfur atom than that of the oxygen atom, the inversion symmetry of the perovskite material can be manipulated, resulting in the perovskite unit cells become more elongated along the c -axis. The polar displacements of a Ti atom can be further promoted by increasing the sulfur concentration [7,8].

We controlled the spatial inversion symmetry in the perovskite $\text{Pb}(\text{Zr,Ti})\text{O}_3$ via quantitatively sulfur substitution at the apical oxygen site. By substituting the sulfur at the apical oxygen site, a structural phase transition from the monoclinic $\text{Pb}(\text{Zr,Ti})\text{O}_3$ to tetragonal $\text{Pb}(\text{Zr,Ti})\text{O}_{3-x}\text{S}_x$ as schematized in Figure 1.3. The sulfur (S) makes a strong covalent bond with the titanium (Ti) element (Ti $3d$ -S $3p$) compared with the Ti $3d$ -O $2p$ bonding due to the lower electronegativity of the sulfur element than the oxygen atom. The strong covalency of the Ti-S (apical) bonding lifted the spatial inversion symmetry uniformly in PZT oxysulfide as shown in Figure 1.3.

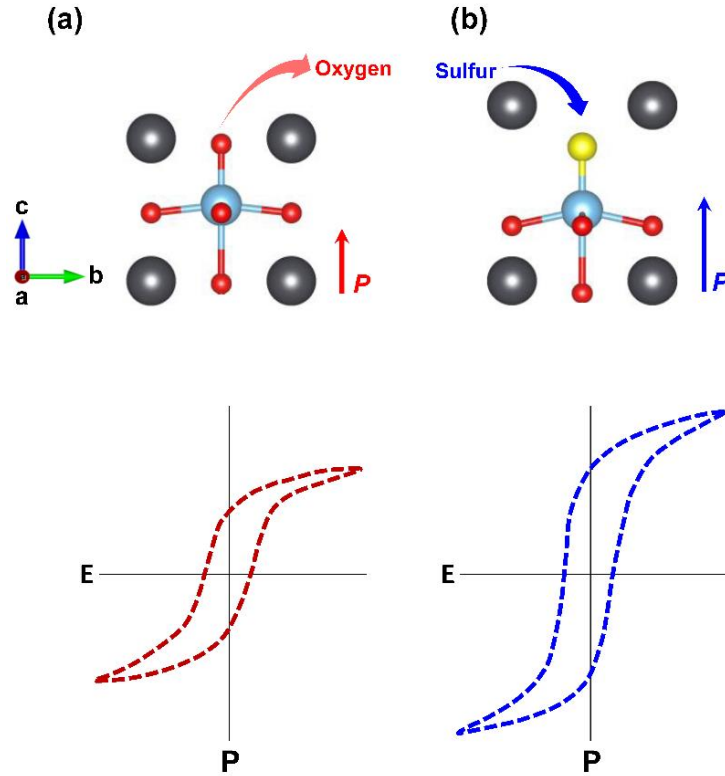


Figure 1.3 Enhancement of ferroelectric polarization via sulfur substitution at the apical oxygen site. (a) A perovskite material, (b) inversion symmetry breaking in perovskite by sulfur substitution forming the oxysulfide.

1.4.2 High piezoelectricity at low field

The large strain hysteresis and electro-strain at a high applied electric field restrict the utilization of the bismuth-based (i.e., $\text{Bi}_{1/2}\text{Na}_{1/2}\text{TiO}_3$; BNT) materials for the practical actuating application. Many efforts, such as compositional tuning, relaxor-ferroelectric composite, and textured ceramics by the templated grain growth (TGG) have been placed to achieve high strain at a low applied electric field [11-13]. The large normalized strain at a low driving field in bismuth-based composite ceramics is proposed to have occurred either due to the polarization-coupling mechanism or residual stress between the relaxor/ferroelectric composites [18,19]. All these

approaches led to the common conclusion that adding an appropriate amount of ferroelectric seeds can significantly improve the strain level at a low driving field.

In this study, by adding the ferroelectric $\text{Bi}_{1/2}(\text{Na}_{0.78},\text{K}_{0.22})_{1/2}\text{TiO}_3$ (BNKT) particles (volume percent fraction) to the relaxor the $0.72\text{Bi}_{1/2}\text{Na}_{1/2}\text{TiO}_3\text{-}0.28\text{SrTiO}_3$ (BNT-28ST), the spatial inversion symmetry in perovskite BNT-28ST is uniformly lifted resulting in a high piezoelectric response at a low applied field in the BNT-28ST/BNKT ceramic composite. Initially, at a zero electric field, the relaxor (BNT-28ST) which is centrosymmetric is surrounding the large-size ferroelectric BNKT (non-centrosymmetric) particles as illustrated in Figure 1.4(a). At a given applied electric field in BNT-28ST/BNKT composite, the BNKT ferroelectric particles compressively stressed the BNT-28ST relaxor ceramic and lifted the spatial inversion symmetry of the relaxor BNT-28ST ceramic. Consequently, a structural transition from the pseudocubic BNT-28ST to tetragonal is identified with the spatial inversion symmetry controlled, leading to the high piezoelectric response at the low (applied/driving) electric field in the BNT-based ceramic composite as provided in Figure 1.4(b).

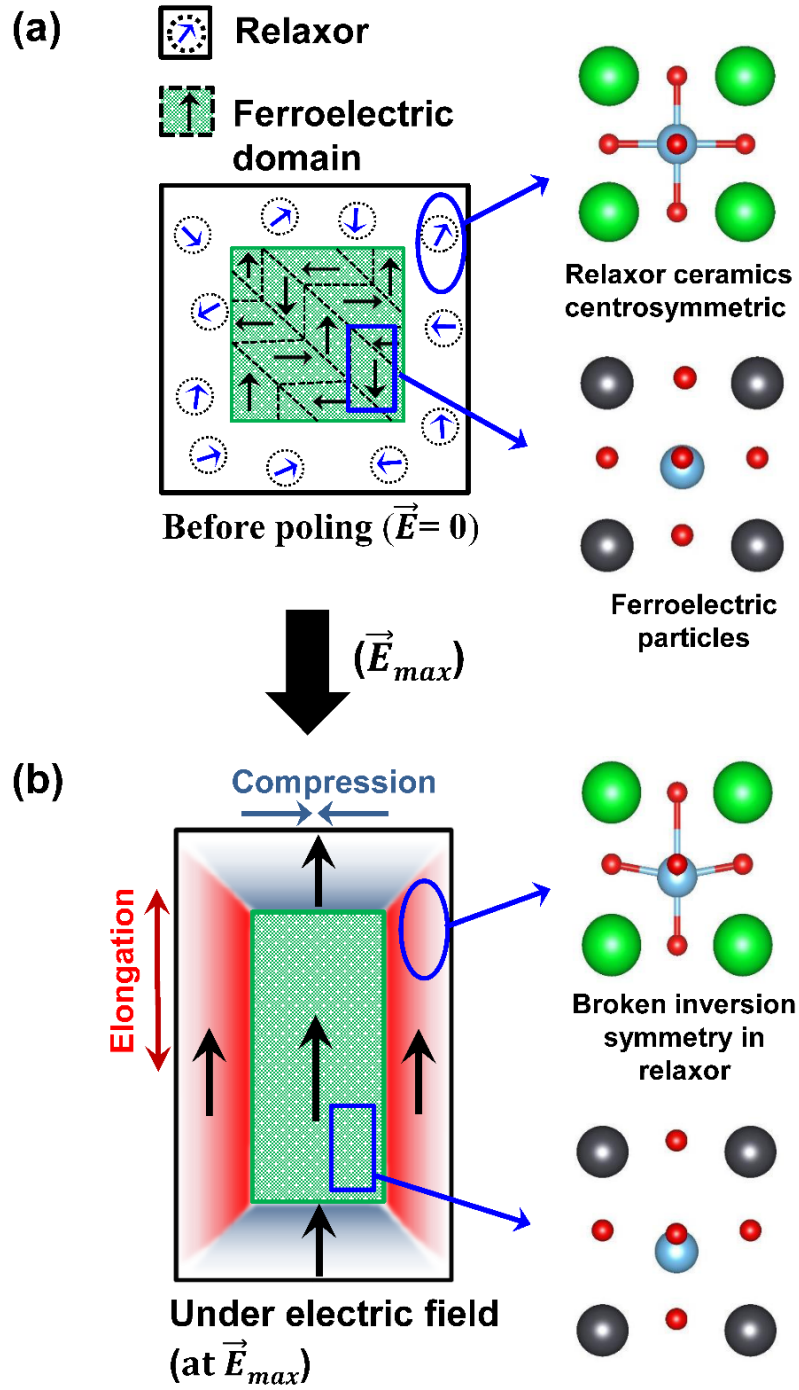


Figure 1.4 Schematic diagram of the symmetry breaking in relaxor-ferroelectric composites. (a) Relaxor ferroelectric composite at a zero electric field, (b) at a maximum electric field.

1.4.3 Improper ferroelectricity in hexagonal materials

Improper ferroelectricity, the ferroelectricity induced due to the collaboration of the two or more non-polar structural parameters [20,21]. This kind of ferroelectric ordering emerges geometrically from the tilting and deformation of the trigonal MnO_5 bipyramid in the hexagonal materials, such as ferroelectric YMnO_3 (space group: $P6_3cm$) with a T_c at ~ 1270 K [20,21]. The origin of the improper ferroelectricity is different from the proper ferroelectricity which comes from the off-centering (ionic displacement) of a transition metal (cation) in the regular perovskite ferroelectrics is the ligand-field hybridization ($\text{Ti } 3d\text{-O } 2p$) of the transition-metal (B-site) cation and its surrounding oxygen (O-site) anions, like BaTiO_3 , PbTiO_3 , and $\text{Pb}(\text{Zr,Ti})\text{O}_3$.

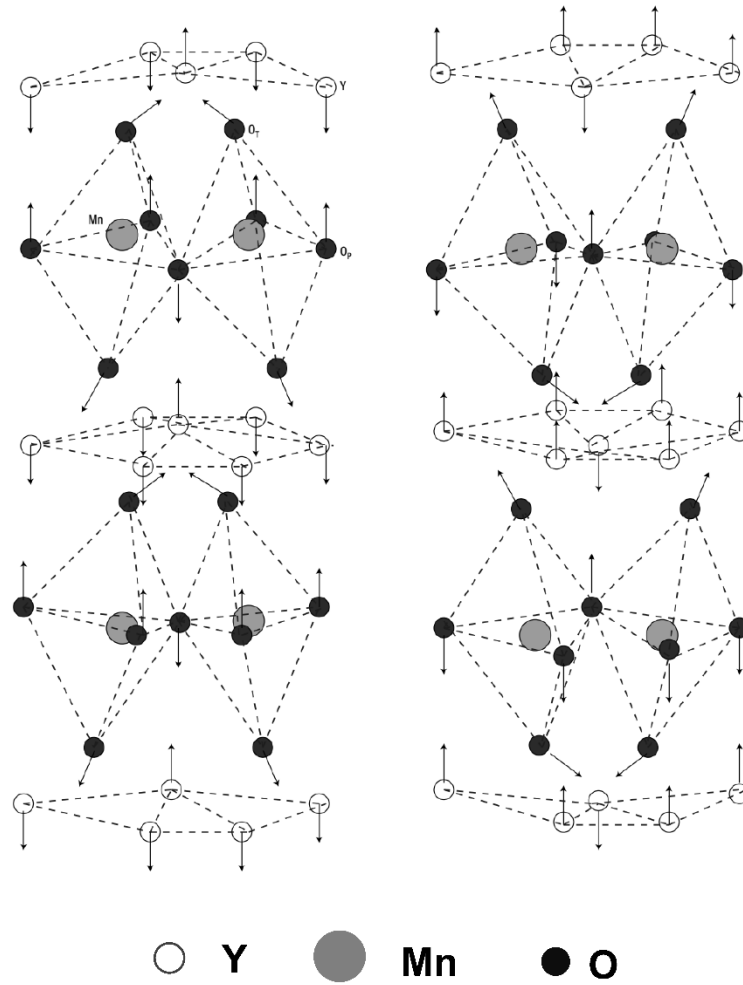


Figure 1.5 Schematic view of hexagonal YMnO_3 structure. The Atomic displacement from the non-ferroelectric (centrosymmetric) ordering to the ferroelectric (non-centrosymmetric) structure is shown by arrows [20].

In the Al-doped SrMnO_3 , we aimed to produce the ferroelectric polarization in 6H-hexagonal SrMnO_3 ceramics with controlled spatial inversion symmetry. Herein, we constructed the hexagonal SrAl_2O_4 grains locally in the proximity to the 4H-hexagonal SrMnO_3 grains by doping the Aluminum (Al) to the SrMnO_3 ceramic. Using the interfacial strain mechanism, a 6H-hexagonal polymorph is realized in the SrMnO_3 polymorph identified in the x-ray diffraction analysis and Raman spectroscopy measurements. We plan to generate the ferroelectric ordering

by octahedral tilting in a 6H-hexagonal SrMnO₃ oxide. Then, the inversion symmetry in 6H-hexagonal SrMnO₃ is expected to be broken and generate a new polar symmetry.

1.4.4 Control of electrical conductivity in SrRuO₃ free-standing films

The symmetry of the centrosymmetric complex oxides materials can be manipulated by applying external stimuli (i.e., stretching or bending) that lower the symmetry or even break the inversion symmetry [14-17]. Recently, the development in the freestanding complex oxide membranes has presented appealing possibilities to address the challenges (strain-driven-defect formation during film growth at high temperature [14-17]) and open a new degree-of-freedom to advance the properties of the material. The metal-to-insulator transition in single-crystalline La_{0.7}Ca_{0.3}MnO₃ membranes under the extreme tensile [uniaxial (8%) and biaxial (5%)] strain by manipulating the inversion symmetry of the La_{0.7}Ca_{0.3}MnO₃ [14]. Moreover, room-temperature ferroelectricity in SrTiO₃ membranes at 2% uniaxial strain is also observed [15]. In this work, we are motivated to synthesize the high-quality SrRuO₃ free-standing membrane down to 2-dimensions (2D) limit and then break the inversion symmetry under the application of the external stimuli (i.e., bending, strain) [16,17]. The electronic ground state can be modified by breaking the inversion symmetry of the oxide material, thus, resulting in interesting conducting properties.

References

- [1] N. Sai, B. Meyer, and D. Vanderbilt, *Phys. Rev. Lett.* **84**, 5636 (2000).
- [2] H. N. Lee, H. M. Christen, M. F. Chisholm, C. M. Rouleau, and D. H. Lowndes, *Nature* **433**, 395 (2005).
- [3] V. M. Fridkin, *Crystallography Reports* **46**, 654 (2001).
- [4] D. Xiao, and L. Gu, *Nano Select* **1**, 183 (2020).
- [5] S. Blundell, *Magnetism in Condensed Matter* (Oxford Univ. Press, Oxford, 2001).
- [6] B. Goodenough, John, *Magnetism and the Chemical Bond* (Interscience-Wiley, New York, 1963).
- [7] J. A. Brehm, H. Takenaka, C. W. Lee, I. Grinberg, J. W. Bennett, M. R. Schoenberg, and A. M. Rappe, *Phys. Rev. B* **89**, 195202 (2014).
- [8] G. Amarsanaa, D. Odkhoo, C. W. Ahn, and I. W. Kim, *J. Appl. Phys.* **116**, 194105 (2014).
- [9] N. Vonrüti and U. Aschauer, *Phys. Rev. Lett.* **120**, 046001 (2018).
- [10] E. J. Moon, A. K. Choquette, A. Huon, S. Z. Kulesa, D. Barbash, and S. J. May, *APL Mater.* **3**, 062511 (2015).
- [11] S. T. Zhang, A. B. Kounga, E. Aulbach, T. Granzow, W. Jo, H. J. Kleebe, and J. Rödel, *J. Appl. Phys.* **103**, 034107 (2008).
- [12] C. W. Ahn, C. H. Hong, B. Y. Choi, H. P. Kim, H. S. Han, Y. Hwang, K. Wang, J. F. Li, J. S. Lee, I. W. Kim, and W. Jo, *J. Kor. Phys. Soc.* **68**, 1481 (2016).
- [13] C. W. Ahn, G. Choi, I. W. Kim, J. S. Lee, K. Wang, Y. Hwang, and Wook Jo, *NPG Asia Mater.* **9**, e346 (2017).
- [14] S. S. Hong, M. Gu, M. Verma, V. Harbola, B. Y. Wang, D. Lu, A. Vailionis, Y. Hikita, R. Pentcheva, J. M. Rondinelli, and H. Y. Hwang, *Science* **368**, 71 (2020).

- [15] R. Xu, J. Huang, E. S. Barnard, S. S. Hong, P. Singh, E. K. Wong, T. Jansen, V. Harbola, J. Xiao, B. Y. Wang, S. Crossley, D. Lu, S. Liu, and H. Y. Hwang *Nat. Commun.* **11**, 3141 (2020).
- [16] D. Lee, *APL Mater.* **8**, 090901 (2020).
- [17] S. Das, B. Wang, T. R. Paudel, S. M. Park, E. Y. Tsymbal, L. Q. Chen, D. Lee, and T. W. Noh, *Nat. Commun.* **10**, 537 (2019).
- [18] A. Khaliq, M. Sheeraz, A. Ullah, J. S. Lee, C. W. Ahn, and I. W. Kim, *Sens. Actuators A Phys.* **258**, 174 (2017).
- [19] H. Zhang, C. Groh, Q. Zhang, W. Jo, K. G. Webber, and J. Rödel, *Adv. Electron. Mater.* **1**, 1500018 (2015).
- [20] B. B. V. Aken, T. T. M. Palstra, A. Filippetti, and N. A. Spaldin *Nat. Mater.* **3**, 164 (2004).
- [21] J. -H. Lee, P. Murugavel, H. Ryu, D. Lee, J. Y. Jo, J. W. Kim, H. J. Kim, K. H. Kim, Y. Jo, M. -H. Jung, Y. H. Oh, Y. -W. Kim, J. -G. Yoon, J. -S. Chung, and T. W. Noh, *Adv. Mater.* **18**, 3125 (2006).

Chapter 2

2. Experimental detail (method)

2.1 Synthesis of the perovskite oxysulfides by method A

To synthesize a sulfurized PZT thin film with high crystallinity (Figure 2.1), a pure PZT thin film was first fabricated using the sol-gel method. Initially, the 0.4 mole/liter of the $\text{Pb}(\text{Zr}_{0.52}\text{Ti}_{0.48})\text{O}_3$ solution was purchased from the Korea Coating materials and Components Co., Ltd. (KCMC). In the synthesis design strategy, the 0.2 mole liter⁻¹ of $\text{Pb}(\text{Zr}_{0.52}\text{Ti}_{0.48})\text{O}_3$ solution was obtained by dissolving the PZT solution in an equal volume ratio to the acetic acid/2-methoxyethanol mixture solvent. The PZT precursor solution was deposited on SrRuO_3 (10 nm)/ SrTiO_3 (001) substrate using spin-coating (speed) at 3000 rpm for 30 s. The wet thin films after each spin coating were dried at 450 °C for 7 min using the hot plate. Afterward, the thin films were heated at 650 °C for 3 min using a box furnace. These steps (spin coating, drying, and heat treatment) were repeated 4 times to synthesized pure PZT thin film. The PZT thin film was finally crystallized by annealing at 650 °C for 30 min in an oxygen atmosphere. To sulfurize the perovskite PZT thin film we use the following two methods.

For the sulfurization of the as-fabricated PZT film, we prepared a thiourea ($\text{CH}_4\text{N}_2\text{S}$) solution as a precursor by dissolving thiourea powder into a mixed solvent consisting of ethanol (8 ml) and water (2 ml). Then, it was continuously stirred for 24 hrs. The thiourea solution was spin-coated on the pure PZT surface [3000 rpm for 30 s], the thiourea-coated PZT film was cured on a hot plate [450 °C for 7 min], and it was annealed in a box furnace for crystallization [650 °C for 33 min]. During the last thermal annealing process, sulfur ions in the surface thiourea layer were diffused inside the PZT film.

In this sulfurization method, we methodologically separate the sulfurization process from the oxide film growth. We first prepare a pure PZT film using a chemical solution (sol-gel) technique. Next, a thiourea solution is spin-coated on the surface of the as-deposited PZT film as a precursor for sulfur doping. Lastly, we thermally annealed the thiourea-covered PZT film to diffuse the sulfur atoms inside the PZT film. Thus, the spatial distribution of sulfur dopants is inhomogeneous, not uniform.

In principle, method A is compatible with other film deposition techniques such as pulsed laser deposition (PLD) and molecular beam epitaxy (MBE) techniques. Thus, it is highly possible to sulfurize an oxide thin film easily, although it is grown by PLD, not the sol-gel method. However, it is very difficult to control the sulfur doping concentration using this method A.

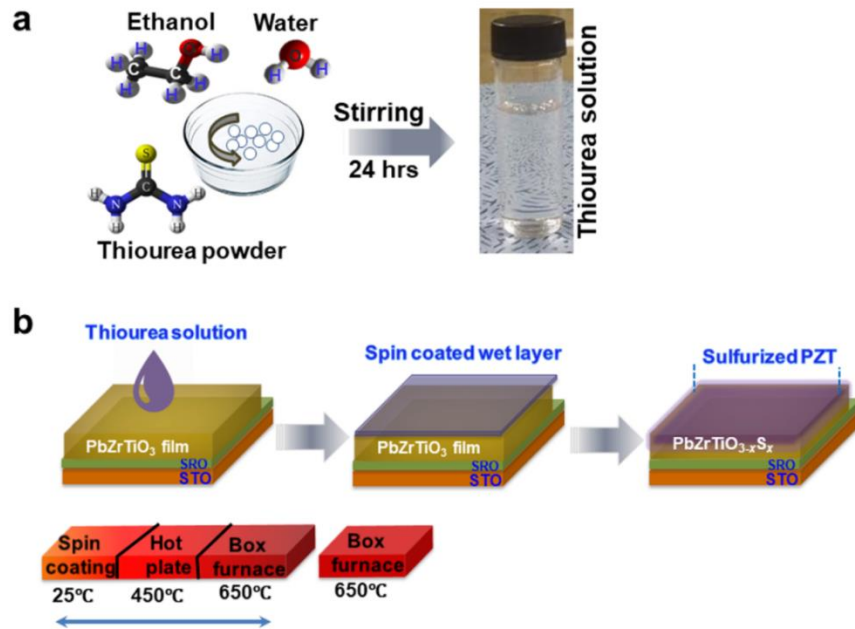


Figure 2.1 Method A: Solution synthesis and thin-film fabrication. (a) Synthesis of the thiourea solution. (b) Fabrication of the sulfurized $\text{Pb}(\text{Zr}_{52}\text{Ti}_{148})\text{O}_3$ using the top layer thiourea solution.

2.2 Synthesis of the perovskite oxysulfides by method B

To control the sulfur-doping concentration in perovskite oxysulfide $\text{Pb}(\text{Zr}_{0.52}\text{Ti}_{0.48})\text{O}_{3-x}\text{S}_x$ thin films precisely (Figure 2.2), we first prepared a diluted PZT solution ($0.2 \text{ mole liter}^{-1}$) by dissolving a commercial PZT solution in the equal volume of the acetic acid/2-methoxyethanol mixture solvent. The thiourea powder with various mole concentrations ($x = 0.01, 0.02, 0.03, 0.04, 0.05$) were added to the diluted PZT solution. And, we kept stirring the thiourea-dissolved PZT solution for 24 hrs continuously. Then, the oxysulfide solution was spin-coated on a SrRuO_3 (10 nm)/ SrTiO_3 (001) film [3000 rpm for 30 s], the spin-coated oxysulfide layer was cured on a hot plate [450 °C for 7 min], and it was annealed in a box furnace [650 °C for 3 min]. As done in the fabrication of pure PZT films, these three steps of the spin-coating, curing, and thermal-annealing were repeated four times to deposit a PZT oxysulfide film with a particular thickness. For the crystallization, we also annealed the as-deposited PZT oxysulfide film at 650 °C for in the box furnace for 30 min.

The thickness of the pure and sulfur-doped PZT films (grown on the Pt(111)/ TiO_2 / SiO_2 /Si(100) substrates) was measured using a field emission scanning electron microscope (FE-SEM) with the energy dispersive spectroscopy (EDS) detector as shown in Figure 2.3. By monitoring the Pb M-edge signals in the raw EDS data, we mapped out the PZT film layer spatially. The average thickness of the pure and sulfur-doped PZT film is nearly $170 \pm 10 \text{ nm}$.

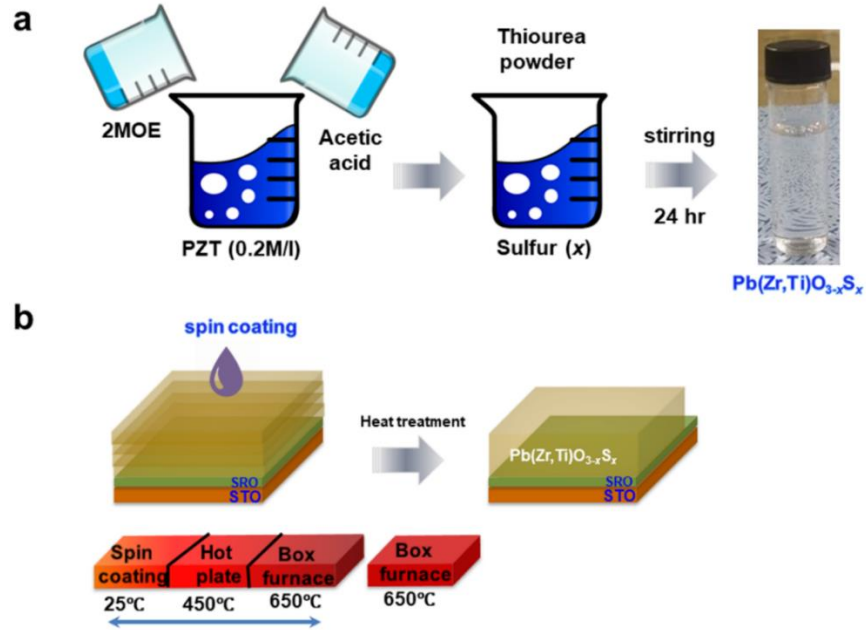


Figure 2.2 Method B: Control of sulfur-doping level in PZT oxysulfide $\text{Pb}(\text{Zr}_{0.52}\text{Ti}_{0.48})\text{O}_{3-x}\text{S}_x$. (a) Synthesis technique of a $\text{Pb}(\text{Zr}_{0.52}\text{Ti}_{0.48})\text{O}_{3-x}\text{S}_x$ oxysulfide using thiourea powder at increasing mole concentration. (b) The deposition of a $\text{Pb}(\text{Zr}_{0.52}\text{Ti}_{0.48})\text{O}_{3-x}\text{S}_x$ oxysulfide on the SrRuO_3 (10 nm, bottom electrode)/ SrTiO_3 (001).

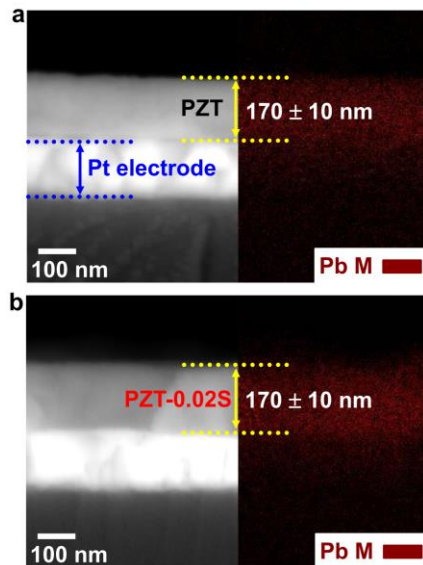


Figure 2.3 Cross-sectional images of the (a) pure PZT and (b) sulfur doped PZT ($\text{PZT}-x\text{S}$, $x = 0.02$).

In contrast with method A, method B is very useful to manipulate the sulfur content in sulfur-doped oxide thin films. In this method, we first prepare an oxysulfide sol-gel solution by dissolving thiourea powders in a pristine oxide solution according to the mole concentration. Next, the as-prepared oxysulfide solution is spin-coated on a substrate and cured. Finally, it is thermally annealed for crystallization. The comparison between Method A and Method B with pros and cons are given in Table 2.1.

Table 2.1. Descriptions of two different sulfurization methods, and pros and cons of each method.

Sulfurization technique	Description	Pros	Cons
Method A	<ul style="list-style-type: none"> • The sulfurization process is decoupled from the film fabrication. • A thiourea ($\text{CH}_4\text{N}_2\text{S}$) solution is separately used for sulfurization. • Sulfur atoms are diffused into the as-deposited oxide thin film by thermal annealing process. 	<ul style="list-style-type: none"> • In principle, this method A is compatible with other film deposition techniques such as pulsed laser deposition (PLD) and molecular beam epitaxy (MBE). 	<ul style="list-style-type: none"> • It is difficult to control the sulfur doping level precisely. • The spatial distribution of sulfur dopants is not uniform.
Method B	<ul style="list-style-type: none"> • An oxysulfide sol-gel solution is prepared by dissolving thiourea powders in undoped oxide sol-gel solution. • By manipulating the mole concentration of the dissolved thiourea powder, it is achievable to control the sulfur doping level in the oxysulfide sol-gel solution. 	<ul style="list-style-type: none"> • Precise control of sulfur doping level is attainable. 	<ul style="list-style-type: none"> • This sulfurization technique is only applicable to a chemical-solution-based method.

2.3 Fabrication of the relaxor/ferroelectric composites

A relaxor $0.72\text{Bi}_{1/2}\text{Na}_{1/2}\text{TiO}_3\text{-}0.28\text{SrTiO}_3$ (BNT-28ST) was chosen as a base material due to its high normalized strain response [1]. To generate a stress-induced high electrostrain at a reasonably low driving field (i.e., via reducing the E_{pol}), the ferroelectric plate-type $\text{Bi}_{1/2}(\text{Na}_{0.78}\text{K}_{0.22})_{1/2}\text{TiO}_3$ (BNKT) particles were applied to the BNT-28ST powders. We introduced the ferroelectric plate-type BNKT particles due to a high linear strain response (~ 293 pm/V) among the BNT-BKT system [2,3]. These ferroelectric plate-type BNKT particles were first synthesized by a two-step molten-salt method and then mixed with the relaxor BNT-28ST powder in various volume proportions (5, 10, and 15 vol.%) to prepare the BNT-28ST/BNKT (relaxor/ferroelectric) composite ceramics.

The relaxor $0.72\text{Bi}_{1/2}\text{Na}_{1/2}\text{TiO}_3\text{-}0.28\text{SrTiO}_3$ (BNT-28ST) and ferroelectric plate-type $\text{Bi}_{1/2}(\text{Na}_{0.78}\text{K}_{0.22})_{1/2}\text{TiO}_3$ (BNKT) particles were prepared using raw materials: Bi_2O_3 , TiO_2 , SrCO_3 , and Na_2CO_3 (99.9%, High Purity Chemicals, Saitama, Japan), and K_2CO_3 ($\geq 99\%$, Sigma-Aldrich). The BNT-28ST composition was synthesized by a conventional solid-state-reaction. Plate-type BNKT particles were synthesized following the two-step molten salt method. Initially, layered structure $\text{Na}_{1/2}\text{Bi}_{4.5}\text{Ti}_4\text{O}_{15}$ (NBT15) particles were synthesized using the chemical reaction (1). Afterward, the perovskite structure plate-type BNKT particles were obtained by the topochemical microstructural conversion method using NBT15 particles as templates as given by the chemical reaction (2), as shown in Figure 2.4 [4,5].



The pure BNT-28ST powder was calcined at 850°C for 2h. Then, plate-type BNKT particles at different volume ratios (5, 10, and 15 vol.%) were added to the BNT-28ST powder

and continuously stirred in ethanol for 24 h to obtain the composite. The composites were formed into green disks of 10 mm in diameter at a pressure of 100 MPa. These solid discs were sintered at 1150°C for 2 h and silver paste was used as an electrode on both faces of the pellets. The electroded samples were baked at 700°C for 30 min in a box furnace to measure electrical properties.

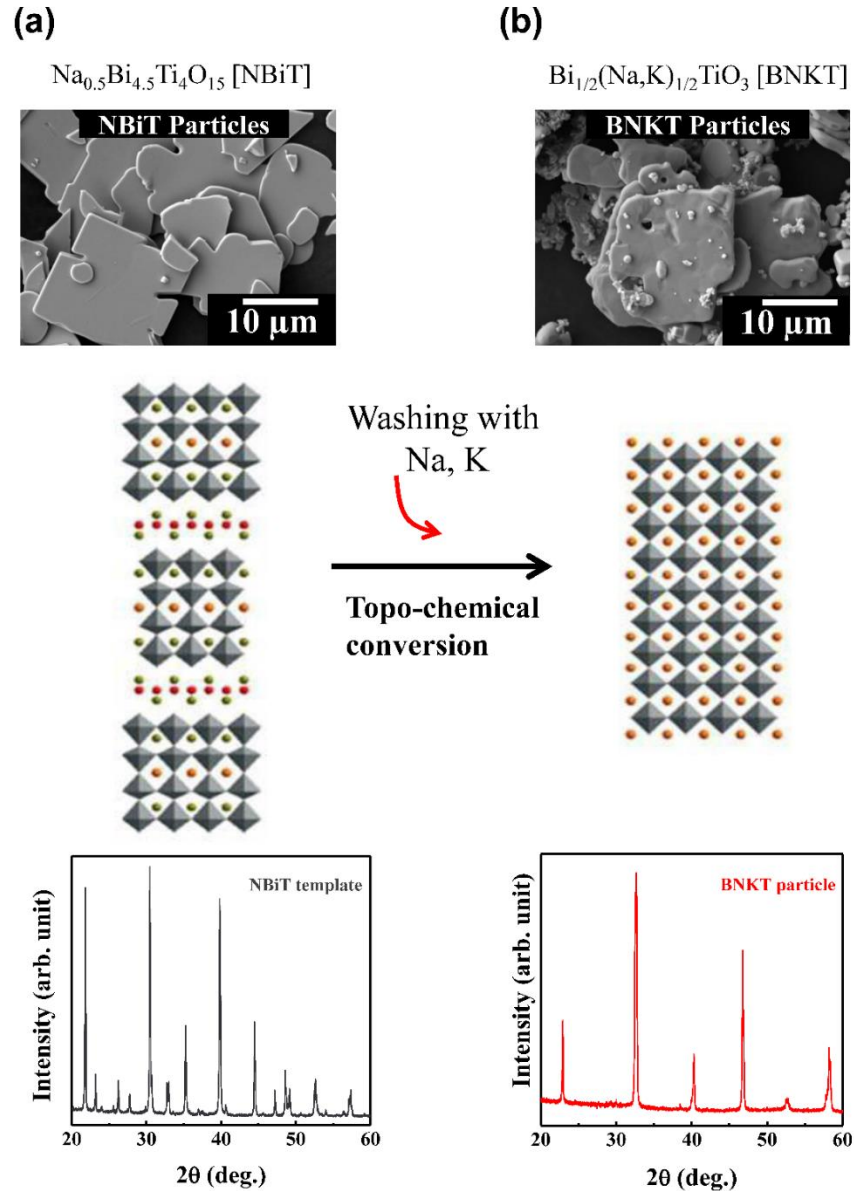


Figure 2.4 The topochemical microstructural conversion of the NBiT15 particles of the structure plate-type BNKT particles.

2.4 Al-doped SrMnO₃ ceramics via solid-state-reaction method

In the design strategy, to realize the 6H-hexagonal ($P6_3/mmc$) SrMnO₃ polymorph, we constructed the hexagonal SrAl₂O₄ ($P6_322$) grains locally in the proximity to the 4H-hexagonal ($P6_3/mmc$) SrMnO₃ grains by doping the Aluminum (Al) to the SrMnO₃ ceramic [6,7,8]. In the presence of the hexagonal SrAl₂O₄ grains, an interfacial strain [lattice mismatch between 4H SrMnO₃ and SrAl₂O₄] will be generated at the grain boundary, where the SrMnO₃ will be compressively stressed, resulting in the realization of the 6H SrMnO₃ polymorph. In step 1 of the schematic Figure 2.5(a), the grounded powders of the SrCO₃ and MnO₂ were mixed, and then Al₂O₃ powders were added at different mole concentrations ($x = 0.01, 0.02, 0.05, 0.10, \text{ and } 0.20$).

The pure and Al-doped SrMnO₃ powder were calcined (i.e., 800 °C for 24 h) in the quartz crucibles to form the mixed grains of the 4H SrMnO₃ (purple grain in a blue circle) and hexagonal SrAl₂O₄ (cyan grain in a blue square) as illustrated in Figure 2.5(b). The calcined powders (which contains the mixed grains of both 4H SrMnO₃ and SrAl₂O₄) were next pressurized at 133 Pa to the pellets (diameter is 7 mm) as presented in Figure 2.5(c). In the next step, we present the sintering process of the Al-doped SrMnO₃ pellets as schematized in Figure 2.5(d). During the densification process at a higher temperature (1350 °C), an interfacial strain would have occurred at the grain boundaries of the 4H SrMnO₃ and a SrAl₂O₄ [Figure 2.5(d)]. The interfacial region where the misfit strain has occurred is shown by the blue rectangle, the 4H SrMnO₃ grain (purple color) receives stress (red arrows) from the SrAl₂O₄ grains (cyan color) in the proximity of the 4H SrMnO₃ grain. This interfacial region (blue rectangle region) is enlarged to clearly understand the stress effect at the grain boundary (white dotted lines) of the 4H SrMnO₃ and SrAl₂O₄ grains. The SrAl₂O₄ grains surrounding the 4H SrMnO₃ grain apply high compressive stress (required to achieve a 6H from the 4H polymorph of SrMnO₃) due to their lattice mismatch. The misfit strain

(from the lattice-mismatch amongst a 4H SrMnO₃ and the SrAl₂O₄) arises at the grain boundaries of 4H SrMnO₃ (5.454 Å) and SrAl₂O₄ (5.17 Å) generates ultra-high stress of ~6.1 GPa, which allows us to achieve a 6H polymorph free from the application of external hydrostatic force. In the final step, 4 [Figure 2.5(e)] illustrates the SEM image of the Al-doped SrMnO₃ ceramic pellet sintered at 1350 °C for 24 h. In the SEM image of the Al-doped SrMnO₃ ceramic, there exist two grain-regions that exhibit a different color contrast, the 6H SrMnO₃ grains (marked by a red circle) and the SrAl₂O₄ grains (marked by cyan square). The 6H SrMnO₃ polymorph is realized (without external hydrostatic pressure) via Al-doping to 4H SrMnO₃. Using the misfit strain mechanism, our plan to break the centrosymmetric 6H-hexagonal SrMnO₃ by tilting the MnO₆ octahedra, realizing the ferroelectric effect in 6H-hexagonal SrMnO₃ with controlled spatial inversion symmetry [9]. However, so we are unsuccessful to produce the ferroelectric polarization via tilting the Mn-octahedra (MnO₆) in the 6H SrMnO₃ polymorph.

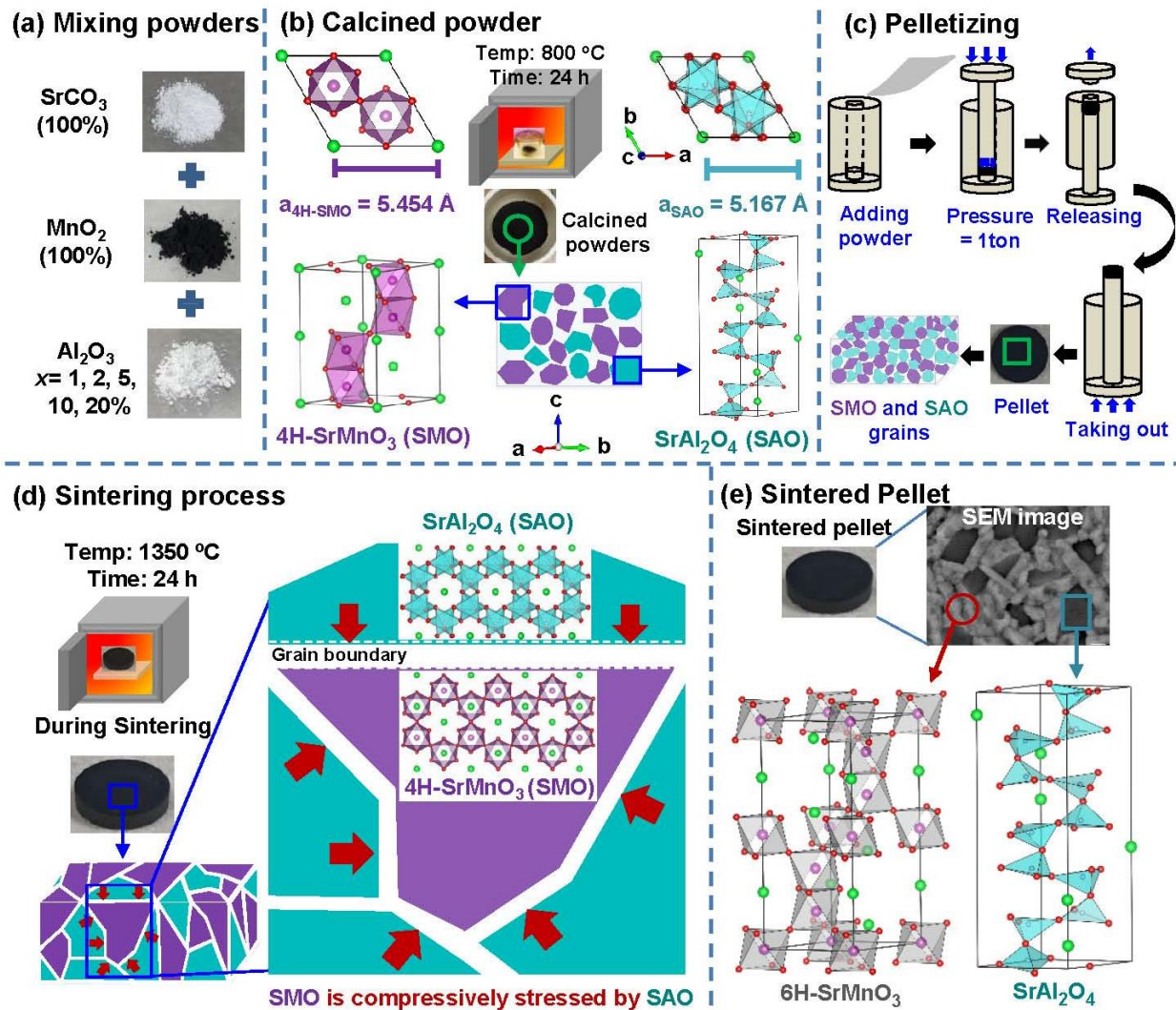


Figure 2.5 The schematic illustration of the achieved 6H SrMnO₃ polymorph via solid-state reaction method.

2.5 Fabrication of free-standing membranes by chemical etching of sacrificial layers

We fabricated the free-standing membranes via chemical etching of two different sacrificial layers.

- (1) Chemical etching of a perovskite $\text{La}_{0.7}\text{Sr}_{0.3}\text{MnO}_3$ (LSMO)
- (2) Chemical etching of a perovskite SrCuO_2 (SCO)

(1) Chemical etching of a perovskite $\text{La}_{0.7}\text{Sr}_{0.3}\text{MnO}_3$ (LSMO)

In this chemical etching process, the SrRuO_3 films were liberated from the SrTiO_3 (001) substrate via selective-etching of a sacrificial $\text{La}_{0.7}\text{Sr}_{0.3}\text{MnO}_3$ (LSMO) film-layer [10,11]. Before beginning the etching process, $\text{SrRuO}_3/\text{La}_{0.7}\text{Sr}_{0.3}\text{MnO}_3/\text{SrTiO}_3$ heterostructure was covered with the polydimethylsiloxane (PDMS) as mechanical polymer support. To perform the etching process of an LSMO layer, the $\text{SrRuO}_3/\text{La}_{0.7}\text{Sr}_{0.3}\text{MnO}_3/\text{SrTiO}_3$ heterostructure is placed in the aqueous (diluted potassium iodide) solution of HCl (10 ml) + KI (8 mg) + H_2O (100 ml) [10,11] [Figure 2.6]; this solution dissolves the LSMO with a high etch rate while having a negligible effect on the SrRuO_3 films [10,11]. In the LSMO, the manganese exist in two oxidation states (Mn^{4+} and Mn^{3+}), the Mn^{3+} makes the LSMO unstable to the acidic solution and thus finally dissolved according to the following reaction [10,11].



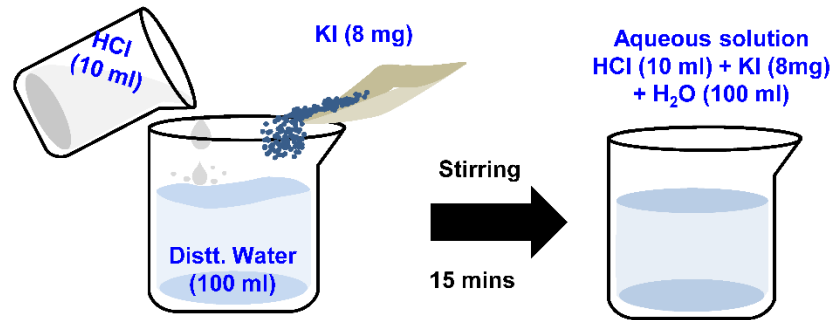
After the complete etching of the LSMO film layer, the released PDMS/ SrRuO_3 thin film was then transferred to secondary substrates (i.e., Pt/silicon or quartz) using a tweezer. After the transfer process is completed, the PDMS is simply released from the SrRuO_3 via a tweezer. The detailed transfer process is schematized in Figure 2.6.

(2) Chemical etching of a perovskite SrCuO_2 (SCO)

To increase the chemical etching rate, we used the SrCuO_2 as a sacrificial layer for the film transfer rather than using the LSMO to increased the etching rate. We select SCO compared to the LSMO because it is oxygen-deficient perovskite, with no oxygen O^{2-} ions in the Sr^{2+} plane, and Cu^{2+} is coordinated with the four oxygen atoms [12]. This oxygen deficiency of the SrCuO_2 perovskite makes it more chemically reactive to other anions (i.e., OH^{1-} or I^{1-}).

The SrRuO₃ films were freed/released from the STO (001) substrate via chemically selective etching of the sacrificial SrCuO₂ layer. The SrRuO₃/SrCuO₂/SrTiO₃ is coated with the PDMS. In this etching process, we put the SrRuO₃/SrCuO₂/SrTiO₃ heterostructures in an aqueous (diluted potassium iodide) solution of HCl (10 ml) + KI (8 mg) + H₂O (100 ml) [10,11] [Figure 2.6]. After the complete etching of the SCO film layer, the released SrRuO₃ epitaxial film was transferred to another secondary substrate (i.e., Pt(111)/TiO₂/SiO₂/Si(100) or quartz) via polydimethylsiloxane (PDMS) polymer support. The detailed transfer process is schematized in Figure 2.6. The transfer films were then used for the structural, surface, and electrical measurements.

(a) Solution preparation



(b) Film transfer

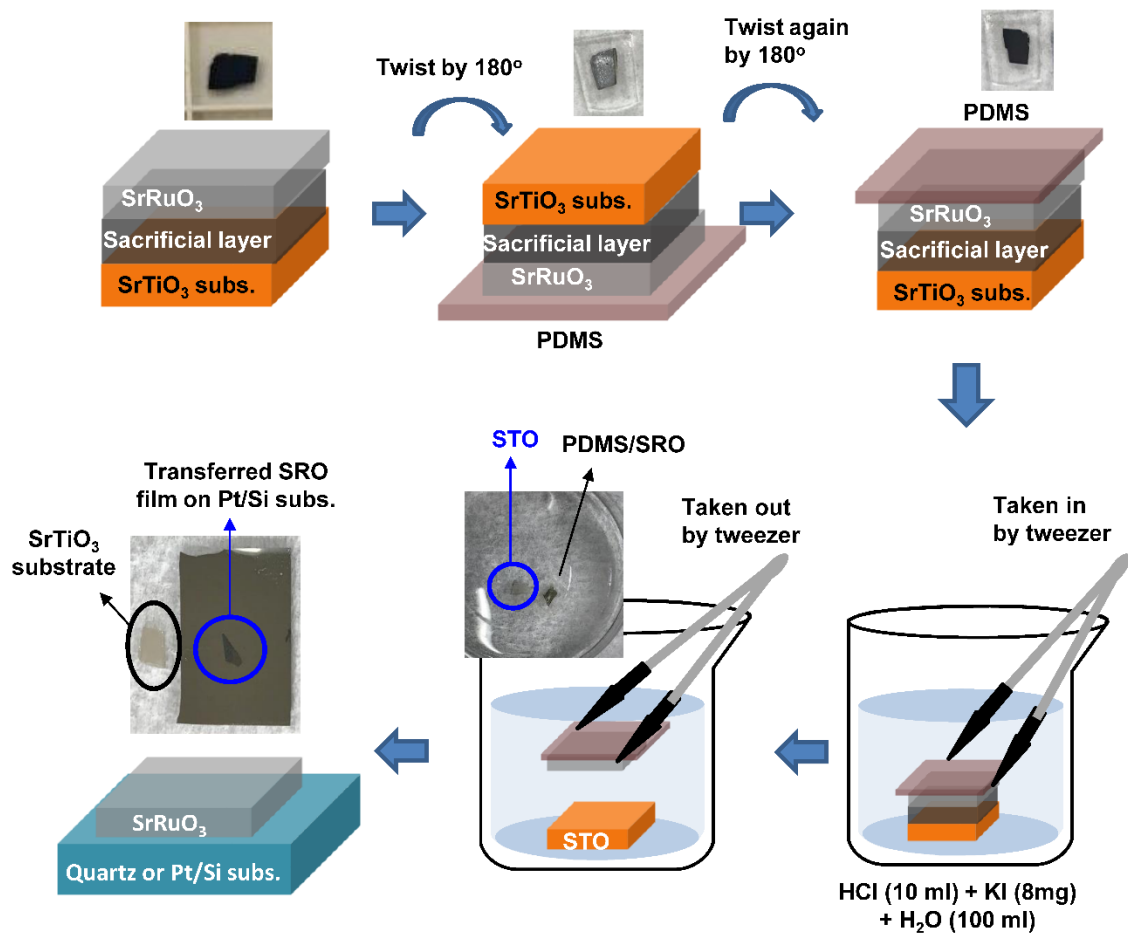


Figure 2.6 (a) Preparation of the aqueous solution of KI (8 mg) + HCl (10 ml) + H₂O (100 ml). (b) Etching of the sacrificial layer (LSMO or SCO) via the aqueous solution of KI (8 mg) + HCl (10 ml) + H₂O (100 ml) and then the SrRuO₃ membrane is transferred to the other substrate for other measurements.

References

- [1] Y. Hiruma, Y. Imai, Y. Watanabe, H. Nagata, and T. Takenaka, *Appl. Phys. Lett.* **92**, 262904 (2008).
- [2] K. Yoshii, Y. Hiruma, H. Nagata, and T. Takenaka, *Jpn. J. Appl. Phys.* **45**, 4493 (2006).
- [3] A. Hussain, C. W. Ahn, J. S. Lee, A. Ullah, and I. W. Kim, *Sens. Actuators A Phys.* **158**, 84 (2010).
- [4] A. Khaliq, M. Sheeraz, A. Ullah, H. J. Seog, C. W. Ahn, T. H. Kim, S. Cho, I. W. Kim, *Ceram. Int.* **44**, 13278 (2018).
- [5] A. Khaliq, M. Sheeraz, A. Ullah, J. S. Lee, C. W. Ahn, I. W. Kim, *Sens. Actuators A Phys.* **258**, 174 (2017).
- [6] R. Sondena, S. Stolen, P. Ravindran, and T. Grande, *Phys. Rev. B* **75**, 214307 (2007).
- [7] H. Shibahara, *J. Mater. Res.* **6**, 565 (1991).
- [8] M. B. Nielsen, D. Ceresoli, P. Parisiades, V. B. Prakapenka, T. Yu, Y. Wang, and M. Bremholm, *Phys. Rev. B* **90**, 214101 (2014).
- [9] B. B. Van Aken, T. T. M. Palstra, A. Filippetti, and N. A. Spaldin, *Nat. Mater.* **3**, 164 (2004).
- [10] S. R. Bakaul, C. R. Serrao, O. Lee, Z. Lu, A. Yadav, C. Carraro, R. Maboudian, R. Ramesh, and S. Salahuddin, *Adv. Mater.* **29**, 1605699 (2017).
- [11] H. Elangovan, M. Barzilay, S. Seremi, N. Cohen, and Y. Jiang, L. W. Martin, and Y. Ivry, *ACS Nano* **14**, 5053 (2020).
- [12] D. Samal, T. Haiyan, H. Molegraaf, B. Kuiper, W. Siemons, S. Bals, J. Verbeeck, G. V. Tendeloo, Y. Takamura, E. Arenholz, C. A. Jenkins, G. Rijnders, and G. Koster, *Phys. Rev. Lett.* **111**, 096102 (2013).

Chapter 3

Enhanced ferroelectricity in perovskite oxysulfides

3.1 Perovskite oxysulfides $ABO_{3-x}S_x$

Perovskite oxysulfides $ABO_{3-x}S_x$, where the apical or equatorial oxygen sites in perovskite transition-metal oxides ABO_3 are partially substituted by sulfur S atoms [Figure 3.1], are of great interest. Its fascinating physical phenomena (i.e. the enhanced ferroelectricity [1,2], the band-gap tuning [3,4], the improved photocatalytic activity [5,6], the structural phase transition [1,2], and so forth) can enable the realization of novel multi-functional devices [1-6].

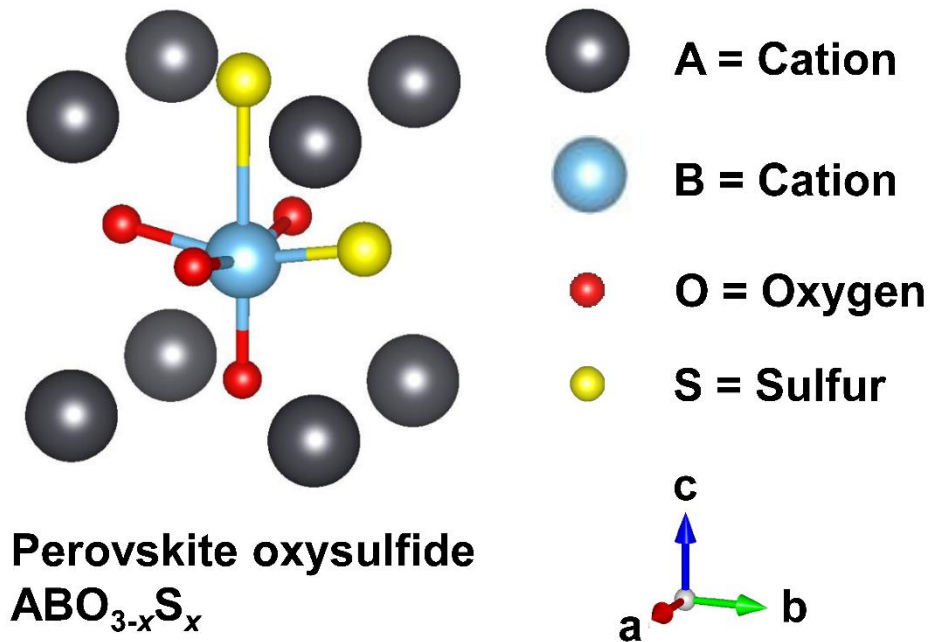


Figure 3.1 Perovskite oxysulfides, the sulfur substitution at the apical or equatorial oxygen position.

3.2 Inversion symmetry control by sulfur doping

The inversion symmetry of complex oxides is reflected in its functional properties. Whenever the inversion symmetry of oxide material is broken, new functionalities arise, can be

utilized for the performance of functional materials for technological applications. Recently, theoretical groups predicted that anion substitution to perovskites is considered an alternative way of manipulating the inversion symmetry in perovskites [1,2].

Due to the isovalent nature of a sulfur S atom ($3s^23p^4$) with an oxygen O atom ($2s^22p^4$), an oxygen atom is easily substituted with a sulfur atom [2]. Note that a sulfur atom possesses a larger ionic radius ($\sim 1.84 \text{ \AA}$) than an oxygen atom ($\sim 1.4 \text{ \AA}$) [7,8]. With the substitution of the oxygen atom with the sulfur atom, the initial perovskite structure is distorted with the modification of the crystallographic symmetry, and an optical gap in the electronic band structure becomes reduced with the broadening of the band-width [1,2]. For perovskite oxysulfide $\text{PbTiO}_{3-x}\text{S}_x$, it was theoretically reported that the polar Ti displacement with respect to the equatorial oxygen atom is further enhanced, when the apical oxygen atom in the parent compound is replaced by a sulfur atom [1]. It was also found that the tetragonality in the sulfurized $\text{PbTiO}_{3-x}\text{S}_x$ distinctly increases resulting in higher spontaneous polarization compared with the pure PbTiO_3 . With the enhancement in ferroelectricity and tetragonality, an indirect bandgap in the electronic structure becomes narrowed from 3.44 (PbTiO_3) to 2.25 eV (PbTiO_2S) [1]. Similar behaviors by sulfurization were predicted in a tetragonal perovskite oxysulfide KNbO_2S , too [2].

3.3 Challenges and realization of perovskite oxysulfides

The effect of sulfurization on physical properties in perovskite oxides has been limitedly studied due to the challenging synthesis of perovskite oxysulfides with high crystallinity [3-6,9-11]. Despite a few earlier reports of the structural, electronic, optical, photovoltaic, and photocatalytic properties in bulk perovskite oxysulfides [3,5,6,12], a systematic experimental study of the sulfurization effects has been rare. Note that most of the previous theoretical results

were derived from the first-principles calculations with primitive unit cells without considering possible disorder in actual experiments at finite temperatures [1,2]. Accordingly, perovskite-oxysulfide single crystals with high crystallinity are essential for a fair comparison of theoretical predictions with experimental results. Based on the previous literature, however, most of the bulk perovskite-oxysulfide compounds are ceramics with poly-crystallinity (i.e. the coexistence of many grains with different crystallographic orientations) [3-6]. Experimentally, it is very difficult to synthesize bulk single crystals with a sufficient amount of sulfur due to the volatility of the sulfur element [3,6,9,12,13]. In case of the conventional solid-state-reaction method [3,6,9,12,13] a sintering process at a high temperature above 1,000 °C is usually required for the crystallization [3,6,9,12,13]. Under such a high sintering temperature, sulfur atoms are readily vaporized and thereby, the overall sulfur content in the bulk compound becomes deficient significantly [3,6,9,10,12,13]. Therefore, to overcome this limitation, a new approach should be developed and then, be implemented for studying the sulfurization effects on perovskite oxides systematically.

A key to realize perovskite oxysulfides with high crystallinity is to separate the sulfur-doping process from the sample fabrication. With this design strategy, various synthetic methods have been utilized for the sulfurization of complex oxides such as chemical vapor deposition (CVD) in a two-zone furnace [14,15], thermal annealing under either CS₂ [3,10] or H₂S gas flow [4,16], and so on [3,4,10,14-16]. Here, a source oxide material is first prepared and then, the base material is chemically reacted with a precursor (e.g. CS₂ and H₂S) incorporating a sulfur element at a particular temperature, which produces an oxysulfide. Nevertheless, for the both cases of the CVD and thermal annealing techniques, precise control of the sulfur-doping concentration turned out to be quite difficult [3,4,10,14-16], *albeit* the base oxide material was sulfurized successfully. Thus,

an alternative route needs to be explored for the artificial design to perovskite oxysulfides with the stoichiometric control of the sulfur content.

In this work, we have established a new and facile method to realize perovskite oxysulfides with high crystallinity. In our technique, a thiourea ($\text{CH}_4\text{N}_2\text{S}$) solution, where S^{2-} can act as a substitute for O^{2-} , is used as a precursor for sulfurization. First, a thiourea solution is spin-coated on a specimen surface and then, is thermally annealed for the diffusion of sulfur atoms inside the sample. While manipulating the mole concentration of the thiourea solution, it is feasible to control the sulfur-doping level in the resulting oxysulfides quantitatively. Hence, we can systematically examine the sulfurization effects on their physical properties, which enable us to compare experimental results with theoretical calculations directly. When sulfur is doped to high-crystalline $\text{Pb}(\text{Zr,Ti})\text{O}_3$ (PZT) films, it is experimentally identified that the ferroelectric polarization is enhanced with an increase in the tetragonality, which is in agreement with theoretical predictions. The pronounced tetragonal distortion and thereby, the increase of ferroelectric transition temperature are demonstrated by synchrotron x-ray diffraction analyses. It is highly likely that an apical oxygen atom is replaced by a sulfur atom leading to further softening of ferroelectric phonon modes in the PZT oxysulfides. In addition to the enhanced ferroelectricity, the reduction of a bandgap is observed, which can be attributed to the band-width broadening by sulfur substitution. Based on the experimental observations, the potential of our sulfur-doping technique will be discussed in the aspect of multi-functional material design.

3.4 Theoretical predictions of a sulfurization effect on $\text{Pb}(\text{Zr}_{0.5}\text{Ti}_{0.5})\text{O}_3$

The effect of sulfur doping on the structural and electrical properties in ferroelectric PZT was theoretically examined through first-principles calculations. In these calculations, we

construct the tetragonal $\text{Pb}(\text{Zr}_{0.5}\text{Ti}_{0.5})\text{O}_3$ structure with a uniform distribution of Ti and Zr [space group $I4mm$ (No. 107)] as shown in Figure 1(a) (for more details of the computational method, see the Appendix A). A sulfur atom is substituted for an oxygen atom in the tetragonal $\text{Pb}(\text{Zr}_{0.5}\text{Ti}_{0.5})\text{O}_3$, which has three distinguishable O-sites: the Ti-top, Ti-side, and Ti-bottom sites, as marked in Figure 3.2(a). Through the calculation of the formation energies for three different S substituted PZT structures ($E_f = E(\text{PZT-S}) - E(\text{PZT}) + \mu(\text{O}) - \mu(\text{S})$, where $\mu(\text{O})$ and $\mu(\text{S})$ are the chemical potentials of the O and S atoms), we confirm that the structure is very unstable for the replacement of the Ti-side oxygen atom with a sulfur atom ($E_f = 4.053$ eV/atom), by comparison with the other sulfur substitution cases [Ti-top (3.198 eV/atom) and Ti-bottom (3.795 eV/atom)]; Therefore, we only consider the effect of sulfur substitution for the Ti-top and Ti-bottom oxygen sites [i.e. Ti-top (3.198 eV/atom) and Ti-bottom (3.795 eV/atom)]. Interestingly, as the sulfur substitution ratio increases, the c/a ratio (i.e. tetragonality) increases [the black solid line in Figure 3.2(b)]. Due to the larger ionic radius of the sulfur atom than that of the oxygen atom, the PZT unit cells become more elongated along the c -axis and the Zr and Ti ions are off-centered further. With the promoted polar displacements of Zr and Ti atoms, it is evident that ferroelectric polarization in the sulfurized PZT increases, as the sulfur concentration increases.

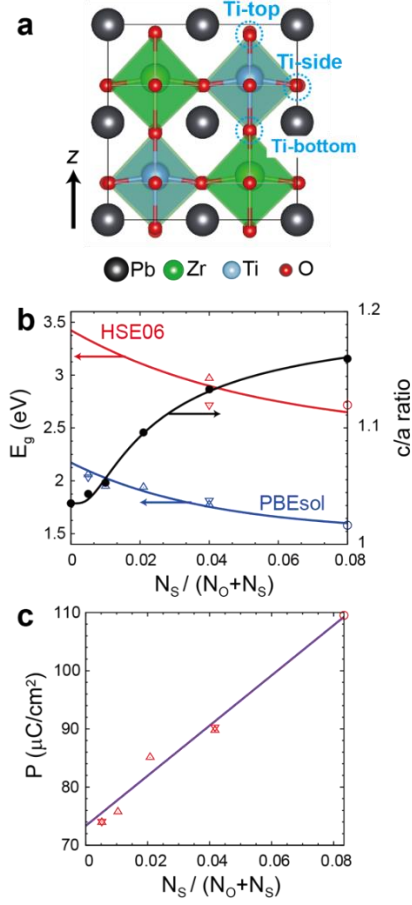


Figure 3.2 Theoretical calculations of the sulfurization effect on $\text{Pb}(\text{Zr}_{0.5}\text{Ti}_{0.5})\text{O}_3$. (a) Atomic structure of tetragonal $\text{Pb}(\text{Zr}_{0.5}\text{Ti}_{0.5})\text{O}_3$ with a uniform distribution of Ti and Zr. Three distinguishable oxygen sites relative to Ti are denoted. (b) The variations of the c/a ratio and the bandgap (E_g) with PBEsol and HSE06 exchange-correlation functionals. (c) The spontaneous polarization P along the z -direction at the sulfur substitution ratio $N_S/(N_O + N_S)$ of tetragonal $\text{Pb}(\text{Zr}_{0.5}\text{Ti}_{0.5})\text{O}_{3-x}\text{S}_x$.

In contrast to the enhanced tetragonality and ferroelectricity, it was found that the electronic band gap decreases with the increasing sulfur concentration [Figure 3.2(b)]. Note that the bandgap in tetragonal PZT is determined by the O 2p and Ti 3d orbital states, which mainly contribute to the valence band maximum (VBM) and conduction band minimum (CBM), respectively. In substitution of a sulfur atom for an oxygen atom, the S 3p orbital states are formed at the VBM.

The broadening of S 3*p* band of the VBM is larger than the increment of the energy difference between CBM and the band edge formed by O 2*p*, which leads to the band-gap reduction in the electronic structure [Figure 3.3].

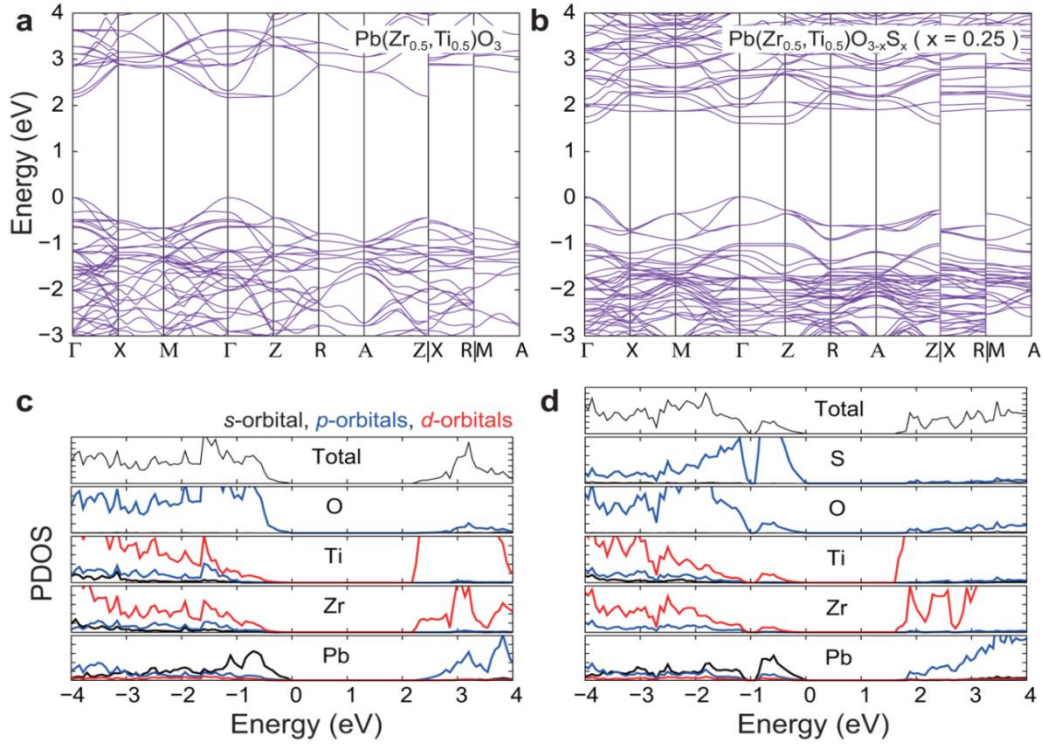


Figure 3.3 Band structure and density of states calculation. (a) and (b) The band structures of the tetragonal $\text{Pb}(\text{Zr}_{0.5}\text{Ti}_{0.5})\text{O}_3$ and oxysulfide $\text{Pb}(\text{Zr}_{0.5}\text{Ti}_{0.5})\text{O}_{3-x}\text{S}_x$ ($x = 0.25$). (c) and (d) The total density of states and atomic-orbital projected density of states for tetragonal $\text{Pb}(\text{Zr}_{0.5}\text{Ti}_{0.5})\text{O}_3$ and oxysulfide $\text{Pb}(\text{Zr}_{0.5}\text{Ti}_{0.5})\text{O}_{3-x}\text{S}_x$ ($x = 0.25$). The Fermi energy is taken to be zero.

3.5 Experimental methods

To validate our theoretical predictions of sulfur-substituted PZT experimentally, we prepared PZT films and then, sulfurized them by spin-coating a thiourea ($\text{CH}_4\text{N}_2\text{S}$) solution on the PZT film surface and via the successive thermal annealing for its diffusion. A high-crystalline

$\text{Pb}(\text{Zr}_{0.52}\text{Ti}_{0.48})\text{O}_3$ film, which is compositionally at the morphotropic phase boundary (MPB) in the bulk compound [18-20], was first synthesized on a SrRuO_3 (10 nm, bottom electrode)/ SrTiO_3 (001) heterostructure using the sol-gel method [Fabrication process in Chapter 2]. In the vicinity of MPB, the PZT film is structurally monoclinic and this monoclinic symmetry is very sensitive to external stimuli such as chemical doping [21], temperature [22], electric field [22-25], mechanical stress [22,26,27], and so on [21-27]. The structural sensitivity of such monoclinic PZT films to a chemical modification allows us to monitor a structural change by sulfur doping easily. Then, we sulfurized the monoclinic $\text{Pb}(\text{Zr}_{0.52}\text{Ti}_{0.48})\text{O}_3$ film by spin-coating a thiourea ($\text{CH}_4\text{N}_2\text{S}$) solution containing the isovalent S^{2-} ion with the O^{2-} ion. And, the thiourea layer coated on the PZT surface was diffused into the PZT film via a thermal annealing process (Fabrication process in Chapter 2).

In our sulfurization method, precise control of the sulfur-doping level in the sulfurized PZT films is also attainable. To do this, a diluted PZT sol-gel solution was prepared by dissolving a conventional PZT solution in the equal volume of the acetic acid/2-methoxyethanol mixture solvent [28]. Then, the diluted PZT solution and thiourea powders were mixed with various mole ratios, which produced a PZT oxysulfide [$\text{Pb}(\text{Zr}_{0.52}\text{Ti}_{0.48})\text{O}_{3-x}\text{S}_x$] sol-gel solution with the controlled sulfur mole concentration ($x = 0.01, 0.02, 0.03, 0.04, \text{ and } 0.05$). Finally, the as-prepared $\text{Pb}(\text{Zr}_{0.52}\text{Ti}_{0.48})\text{O}_{3-x}\text{S}_x$ solution was spin-coated on a SrRuO_3 (10 nm)/ SrTiO_3 (001) substrate and then, it was annealed in air at $650\text{ }^\circ\text{C}$ for 30 minutes for crystallization [Fabrication process in Chapter 2].

3.6 Characterization of the sulfurized perovskites

To identify the crystallinity of our sulfurized PZT films, the high-resolution (HR) image was recorded in the zone axis of [100] as shown in Figure 3.4. In the HR image, the sulfurized PZT thin film consists of a sulfur-doped PZT (~170 nm)/SrRuO₃ (10 nm)/SrTiO₃ (001) film heterostructure. Additionally, a clear lattice image indicates that the sulfurized thin film was well fabricated with good crystalline quality [Figure 3.4(a)]. Selected area electron diffraction (SAED) pattern recorded in the proximity of the sulfurized PZT film/SrRuO₃ bottom interface reveals that the as-synthesized sulfur-doped PZT film is textured along [001] crystallographic orientation with respect to the underlying SrTiO₃ substrate [Figure 3.4(b)]. The chemical composition of the as-fabricated PZT film was also confirmed by a chemical mapping with an energy dispersive spectroscopy (EDS) detector [Figures 3.4(c) and (g)]. The results show that both the film/electrode and the electrode/substrate interfaces are chemically sharp without any interfacial intermixing. While O is observed throughout the entire heterostructure, Pb and Ru only exist in the sulfur-doped PZT film and the SrRuO₃ electrode, respectively. In contrast, the evidence for S is not obvious only with the EDS results due to a little sulfur-doping level.

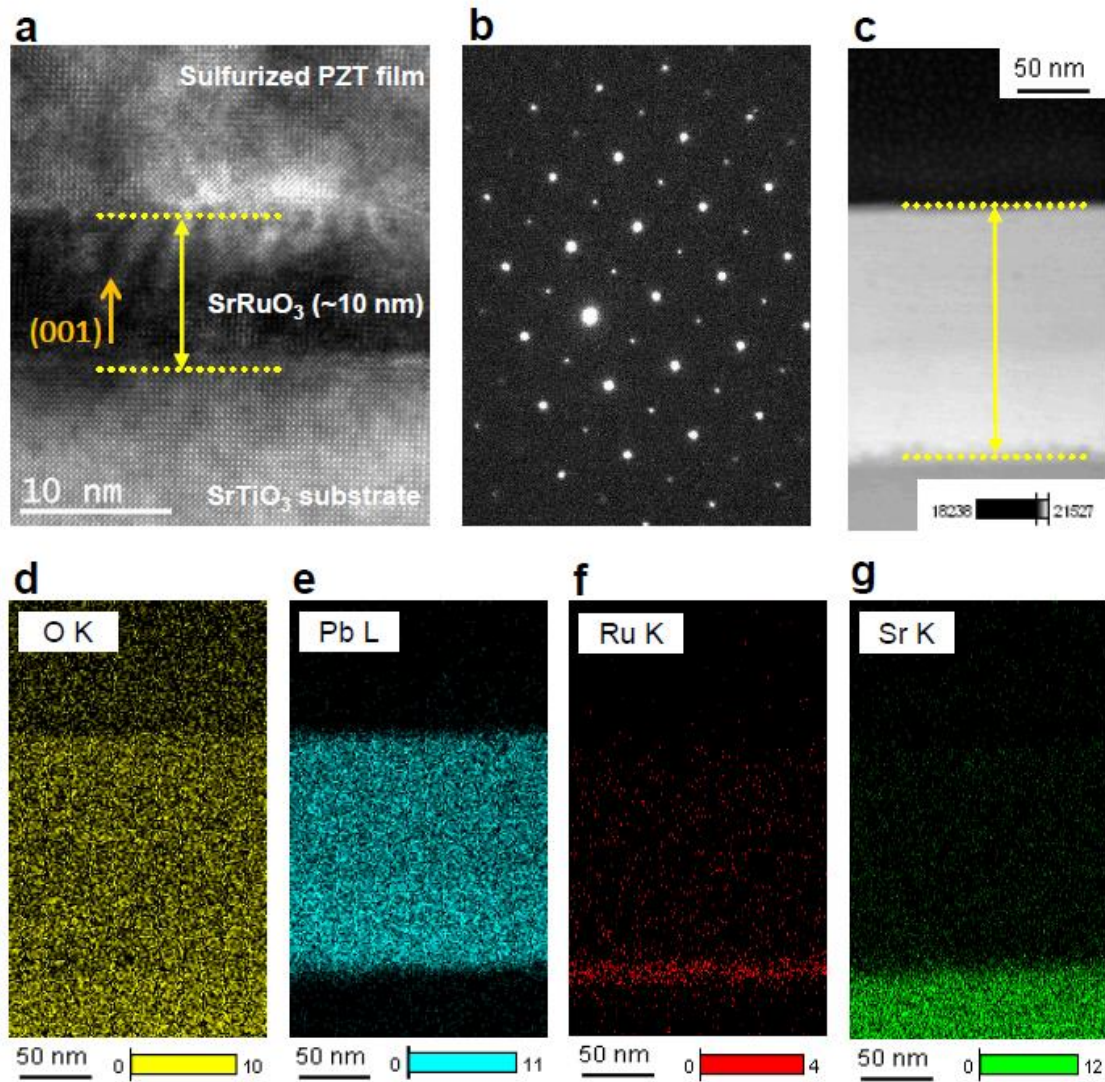


Figure 3.4 Crystallinity and elemental analysis of a sulfurized $\text{Pb}(\text{Zr}_{0.52}\text{Ti}_{0.48})\text{O}_3$ film on SrRuO_3 (10 nm)/ SrTiO_3 (001) substrate. (a) High-resolution transmission electron microscopy image (HRTEM) of a sulfurized PZT film grown on a $\text{SrRuO}_3/\text{SrTiO}_3$ (001) substrate (scale bar: 10 nm), (b) SAED pattern of the PZT at the interface, (c) the dotted yellow color line represents the film thickness through which the composition analysis is carried out. (d-g) Elemental map analysis of the O, Pb, Ru, and Sr, respectively.

The crystallinity of our sulfur-doped PZT films was also confirmed by synchrotron x-ray diffraction (XRD) measurements [Figure 3.5]. The out-of-plane (θ - 2θ) scans of pure PZT (black) and sulfurized PZT films (red) are illustrated in Figure 3.5(a). The pure and sulfurized PZT films grown on the SrRuO₃ (10 nm)/ SrTiO₃ (001) substrates are textured along the [001] crystallographic orientation. A diffraction peak of different crystallographic orientation [i.e. PZT (101)] is also observed. The enlarged view of both peaks in Figures 3.5(b) and (c), clearly differentiates the sulfurized PZT from the pure PZT film. The dotted red colored line represents the (001) peak position of the sulfurized PZT, shifted towards the lower angle compared to the dotted black line for a peak position of the pure PZT. Similarly, in the broad (002) peak, the two diffraction peaks appearance in the pure PZT suggesting that the pure PZT possesses the monoclinic symmetry at the morphotropic phase boundary (MPB). On the other hand, the sulfurization effect can be seen with the emergence of two splitted peaks into a single (002) diffraction peak represented by a solid red curve.

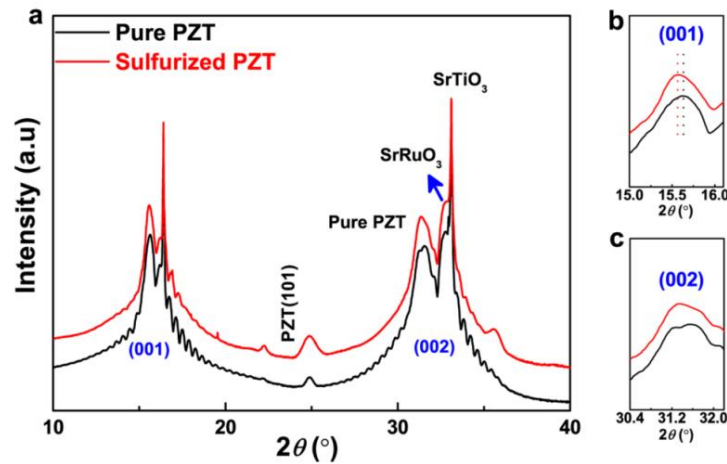


Figure 3.5 The structure characterization of the pure and sulfurized PZT films on SrRuO₃ (10 nm)/SrTiO₃ (001) substrate. (a) Out-of-plane θ - 2θ XRD pattern of pure PZT and sulfurized PZT on SRO/STO substrate. (b) and (c) The enlarged (001) and (002) peaks of pure and sulfurized PZT films.

To verify the existence of sulfur atoms in our sulfurized PZT films, the sulfur and oxygen K-edge spectra were taken in x-ray photoelectron spectroscopy (XPS) measurements [Figure 3.6]. For a pure PZT film, the O K-edge XPS responses were also monitored for a comparison with the sulfur-doped PZT film. As shown in Figure 3.6(a), XPS peaks of S^{2-} (161.8 eV) and S^{4+} (165.4 eV in the binding energy) valence states are evident for the sulfur-doped PZT film, whereas no S signal is measured for the pure PZT film. The presence of sulfur atoms diffused by our method is also identified from the XPS depth profile of a sulfurized PZT film grown on a Pt(111)/TiO₂/SiO₂/Si(100) substrate [Figure 3.6(b)]. By fitting the observed S K-edge curve via the Lorentzian functions, the volume fraction of S^{2-} (a red solid curve in Figure 3.6(a)) and S^{4+} [a blue solid curve in Figure 3.6(a)] states were extracted from the raw XPS data (a black solid curve in Figure 3.6(a)) [29-31]. Note the S^{4+} charge valence state may arise from sulfur dioxide (SO₂) molecules on the film surface [31,32]. Since the portion (30.50 %) of the S^{4+} state is much smaller than that (69.49 %) of the S^{2-} state, the majority of sulfur atoms act as an anion dopant rather than a cation dopant.

We also found that the concentration of oxygen vacancies in a PZT oxysulfide is reduced by sulfurization. As shown in the O K-edge XPS spectra of the pure (black solid line) and sulfurized (red solid line) PZT films [Figure 3.6(c)], the XPS peak (~531.5 eV) corresponding to oxygen vacancies is shifted towards the XPS peak (~528.9 eV) of an oxygen atom in a perovskite oxide lattice. It has been recently reported that oxygen vacancies with a positive ionic charge are accumulated on the surface of ferroelectric films to screen negative polarization bound charges effectively [33,34]. When a ferroelectric PZT film is sulfurized, the accumulated oxygen vacancies on the film surface can be easily replaced by the provided sulfur atoms. The occupation of oxygen vacancies by sulfurization decreases the total amount of oxygen vacancies leading to the lateral

shift of the oxygen vacancy XPS peak. Therefore, it is highly likely that S^{2-} anions were introduced into ferroelectric PZT films through our sulfurization technique, which contributes to the reduction of oxygen vacancies as well as the substitution for the isovalent oxygen ions.

By quantifying the sulfur contents in various PZT oxysulfide films with different sulfur doping concentrations (x) using an electron probe micro-analyzer (EPMA) technique [Figure 3.6 (d)], we demonstrated that the sulfur doping level is controllable in our sulfurization method. Evidently, the measured sulfur contents continuously increase, as the x value increases. On the contrary, oxygen content abruptly decreases for earlier x (< 0.02), probably due to the replacement of oxygen atoms by the sulfur dopants in our PZT oxysulfides. For higher x (> 0.02), the estimated oxygen content does not keep decreasing, and rather, it becomes somewhat saturated close to the finite value.

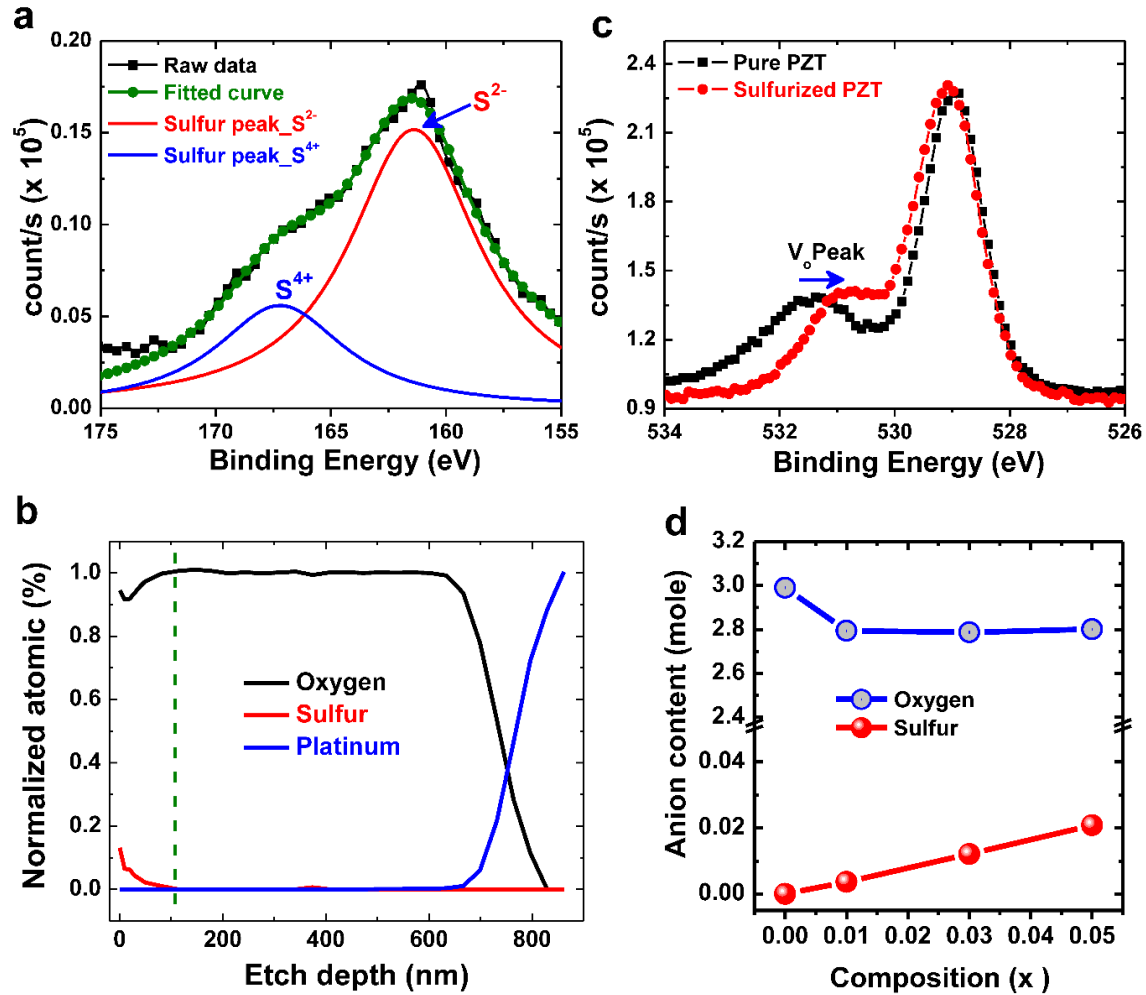


Figure 3.6 X-ray photoelectron spectroscopy (XPS) measurements of a sulfurized $\text{Pb}(\text{Zr}_{0.52}\text{Ti}_{0.48})\text{O}_3$ film. (a) The S K-edge XPS spectrum of a sulfurized PZT film. The red and blue solid curves correspond to the fitting curves of the oxidation states of S^{2-} and S^{4+} , respectively. The solid red curve represents the sulfur (S^{2-}) substitution to an oxygen site, while the blue solid curve shows the presence of SO_2 molecule on the surface of the film. (b) The elemental composition as a function of the depth for the sulfurized PZT film grown on the Pt(111)/ TiO_2 / SiO_2 /Si(100) substrate. (c) The O K-edge XPS spectra of pure and sulfurized PZT films. (d) Electron probe micro-analyzer (EPMA) measurement of the pure and sulfurized PZT film grown on the Pt(111)/ TiO_2 / SiO_2 /Si(100) substrate.

When the monoclinic PZT film is sulfurized, the peak splitting becomes weakened, and thereby, the two separated peaks become merged into a single peak indicative of a monoclinic-to-tetragonal structural transition. With the increasing sulfur-doping level from $x = 0.01$ to 0.05 , the monoclinic-to-tetragonal phase transition is evident, as shown in Figures. 3.7(a)-(e). The L -scan profile of the $\text{Pb}(\text{Zr}_{0.52}\text{Ti}_{0.48})\text{O}_{3-x}\text{S}_x$ film peaks in Figure 3.7(f) clearly shows that the two Bragg peaks induced by a monoclinic distortion become merged with a tetragonal transition, as the sulfur mole concentration increases. By plotting the in-plane (a_{PZT}) and out-of-plane (c_{PZT}) lattice constants of the sulfurized PZT films as the sulfur-doping level (x) [Figure 3.7(g)], we found that c_{PZT} keeps increasing for x less than 0.03 but decreases above $x = 0.03$, whereas a_{PZT} gradually decreases with the increasing sulfur-doping concentration (x). The increase of tetragonality below the critical sulfur-doping content ($x = 0.03$) is consistent with our theoretical prediction of sulfurized PZT and nonetheless, a further study of the decreasing tetragonality above $x = 0.03$ would be highly desirable.

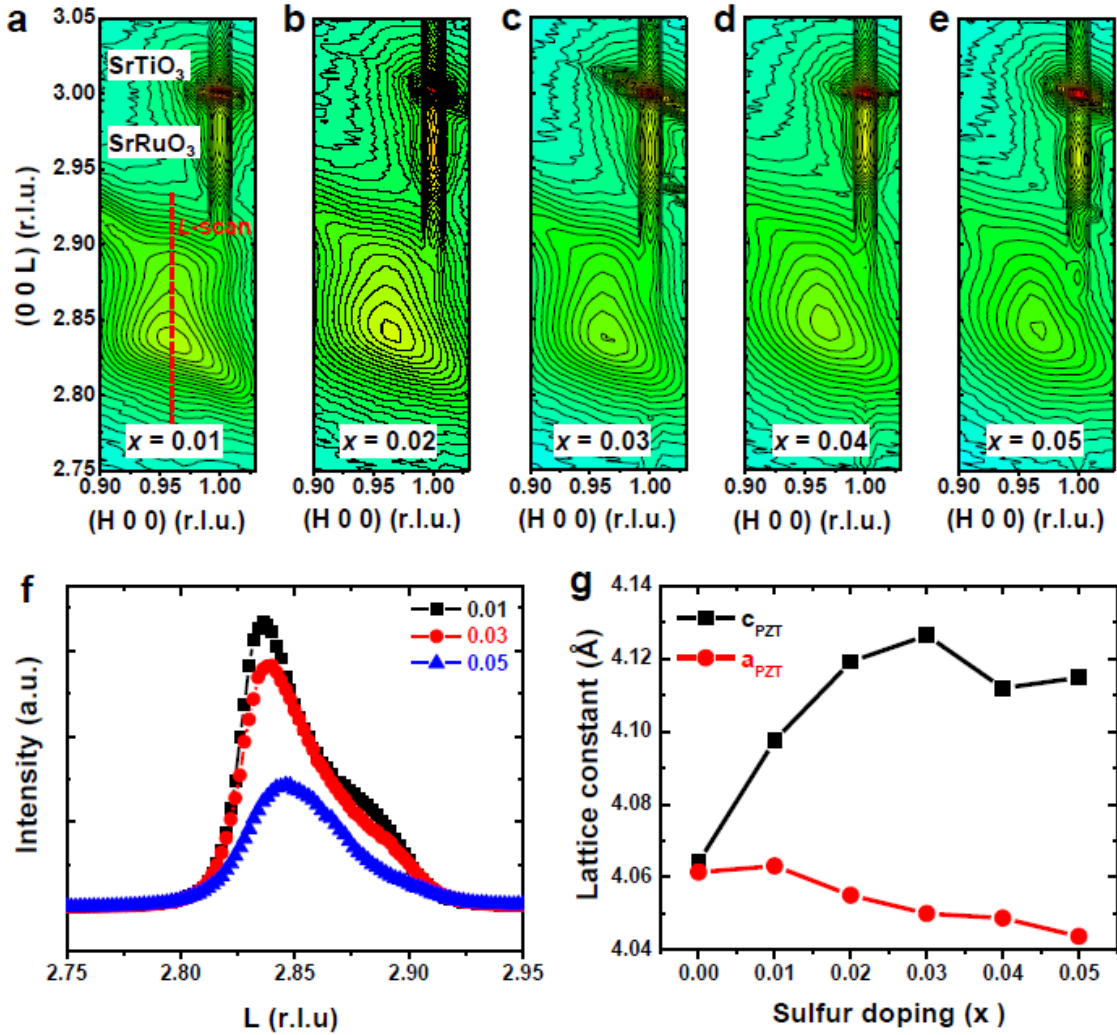


Figure 3.7 The structural analyses of PZT oxysulfide ($\text{Pb}(\text{Zr}_{0.52}\text{Ti}_{0.48})\text{O}_{3-x}\text{S}_x$) films on $\text{SrRuO}_3/\text{SrTiO}_3$ substrates. (a-e) High-resolution RSMs of sulfur-doped PZT ($\text{Pb}(\text{Zr}_{0.52}\text{Ti}_{0.48})\text{O}_{3-x}\text{S}_x$, where $x = 0.01, 0.02, 0.03, 0.04$, and 0.05) films around the (103) Bragg peaks of SrTiO_3 (001) substrate. (f) The L -scan profiles (along the red dotted line in Figure 3.7(a) at $H = 0.96$ in the RSMs of Figures 3.7(a)-(e)). (g) The sulfur-doping level dependence of the in-plane (a_{PZT}) and out-of-plane (c_{PZT}) lattice parameters extracted from the RSM plots.

3.7 Results: Enhancement of ferroelectricity and Bandgap reduction

The tetragonal distortion by sulfurization enhances ferroelectricity in sulfur-doped PZT films. Figure 3.8(a) shows the polarization (P)-electric field (E) hysteresis loops of pure and sulfurized PZT (001) films. It was found that the sulfurized PZT film with larger tetragonality exhibit higher remnant polarization [$P_{\text{avg}} = (|P_{+}|+|P_{-}|)/2 = 34.3 \mu\text{C cm}^{-2}$] than the pure PZT film [$22.2 \mu\text{C cm}^{-2}$].

Using piezoresponse force microscopy (PFM) [Fig. 3.8(b)], we confirmed that the ferroelectricity of these two (i.e., pure and sulfurized) PZT films robustly exhibits strong amplitude signals [Figures 3.8(b), and (c)] and an explicit phase contrast [Fig. 3.8(d), and (e)]. Then, the increase of ferroelectric polarization was also corroborated by comparing the magnitude of their piezo-responses relatively.

By controlling the sulfur-doping content (x) in ferroelectric PZT films and obtaining the corresponding P - E hysteresis loops, we also found that the measured remnant polarization shows a similar tendency with the tetragonality with respect to x [Figure 3.8(f)]. The polarization of the pure PZT and PZT oxysulfide [$\text{Pb}(\text{Zr}_{0.52}\text{Ti}_{0.48})\text{O}_{3-x}\text{S}_x$] with different mole concentration ($x = 0.01, 0.02, 0.03, 0.04, 0.05$) grown on the SrRuO_3 (10 nm)/ SrTiO_3 (001) substrate are shown in the Figure 3.8(f). The remnant polarization with the error bar of the pure and oxysulfide PZT as increasing sulfur substitution is depicted in Figure 3.8(g). The increasing and decreasing trend in the remnant polarization is well-matched with the tetragonal distortion (c/a) extracted from the reciprocal space mapping (RSM) data.

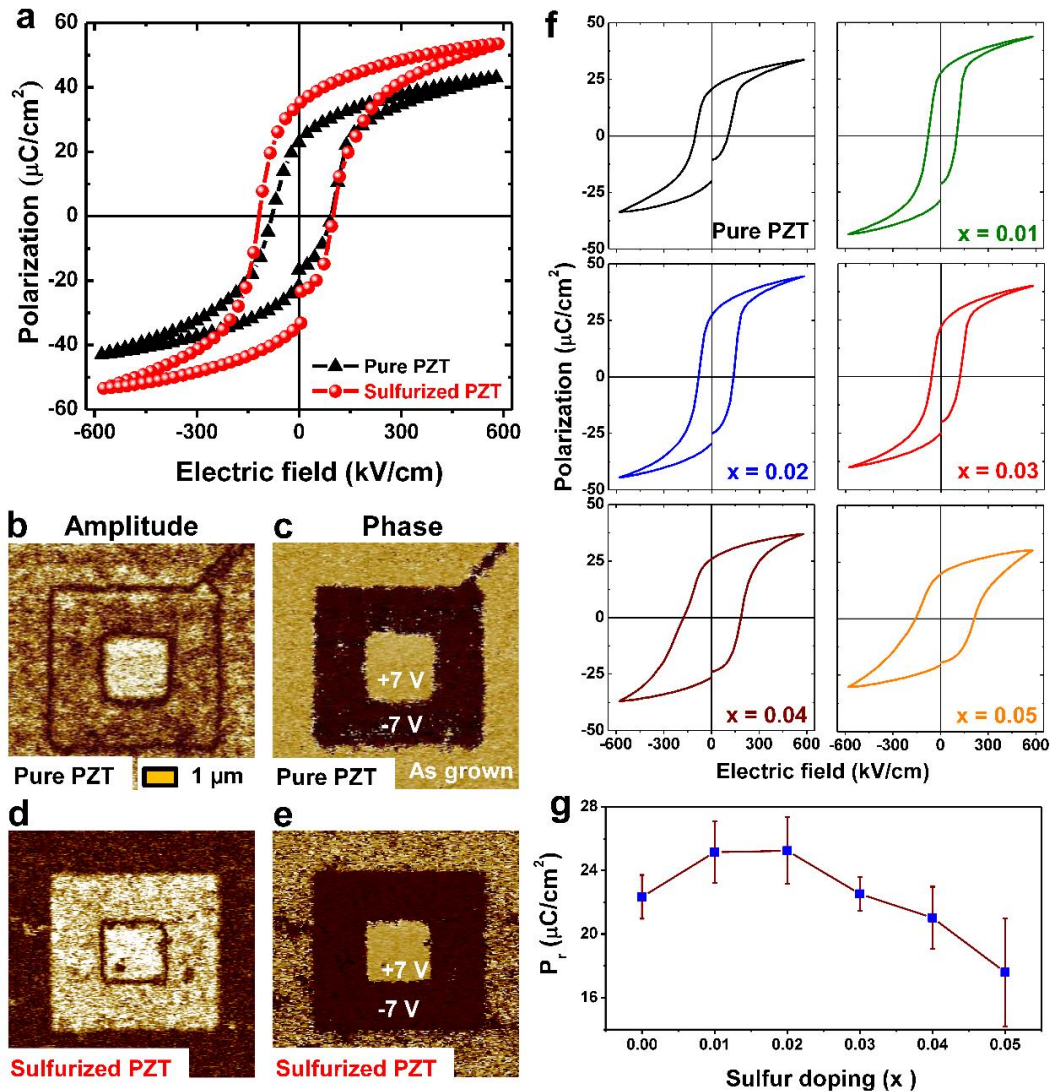


Figure 3.8 Enhancement of ferroelectric polarization in sulfurized $\text{Pb}(\text{Zr}_{0.52}\text{Ti}_{0.48})\text{O}_3$ films. (a) Polarization (P)-electric field (E) hysteresis loops of pure and sulfurized PZT films on $\text{SrRuO}_3/\text{SrTiO}_3$ (001) substrate. (b)-(e) Piezoresponse force microscopy (PFM) images, (b) and (c) out of plane amplitude (R) and (d) and (e) phase (θ) mapping images of the pure and sulfurized PZT films, respectively at the DC bias of ± 7 V. (f) The comparison of the polarization hysteresis loops against the electric field of the pure PZT and PZT oxysulfide ($x = 0.01, 0.02, 0.03, 0.04, 0.05$) on the SrRuO_3 (10 nm)/ SrTiO_3 substrate. (g) Remnant polarization of PZT oxysulfide as increasing sulfur doping level measured at 600 kV/cm.

For a better comparison with our theoretical predictions of enhanced ferroelectricity in PZT oxysulfides, we tested the sulfurization effect on a pure PbTiO_3 film with simple tetragonal symmetry [Figure 3.9]. The measuring setup of the polarization (P)-electric field (E) hysteresis loops of pure and sulfurized PTO films on $\text{Pt}(111)/\text{TiO}_2/\text{SiO}_2/\text{Si}(100)$ substrate is shown in Figure 3.9(a). The hysteresis loops of both the pure PTO and sulfurized PTO were conducting loop. Notably, we found that the sulfur-doped PbTiO_3 film shows a much higher remnant polarization ($26.6 \mu\text{C cm}^{-2}$) than the pure PbTiO_3 film ($17.9 \mu\text{C cm}^{-2}$), which is quite consistent with our results in pure and sulfur-doped PZT films. The increment in remnant polarization between PZT (54.2 %) and PbTiO_3 (48.2 %) oxysulfides are very comparable to each other.

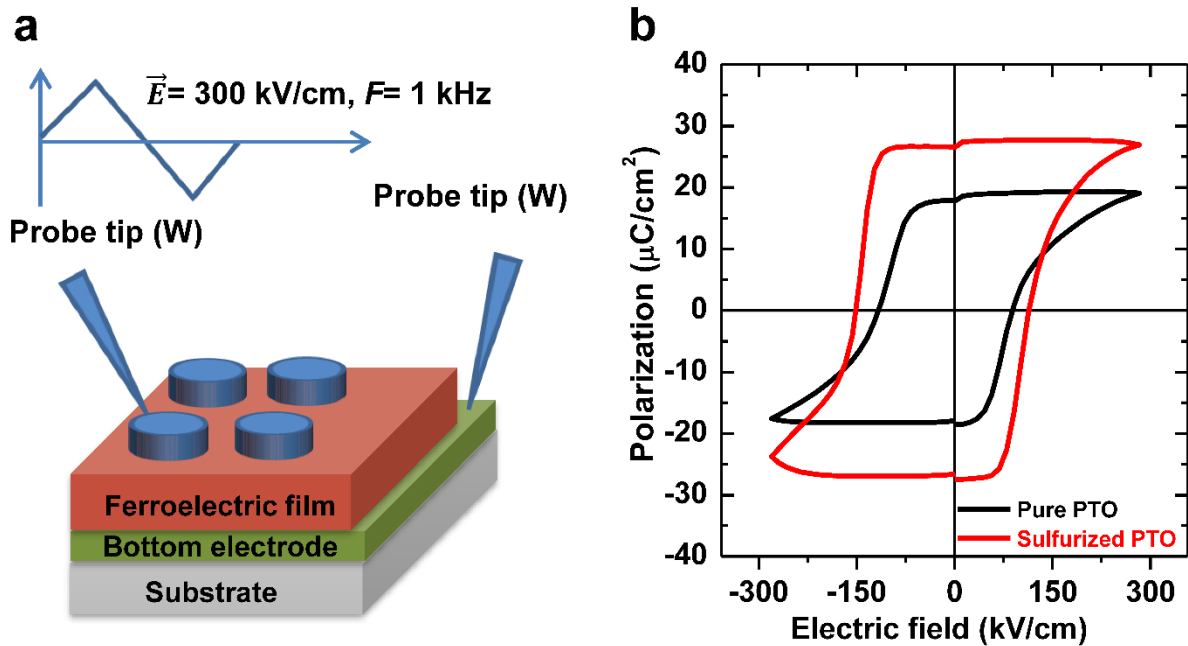


Figure 3.9 (a) Measuring setup for the polarization in sulfurized PbTiO_3 films. (b) Polarization (P)-electric field (E) hysteresis loops of pure and sulfurized PTO films on $\text{Pt}(111)/\text{TiO}_2/\text{SiO}_2/\text{Si}(100)$ substrate.

In contrast with the enhancement in the tetragonality, ferroelectricity, and T_C , an electronic bandgap in a sulfurized PZT film is reduced, which arises from a band-width expansion by the Ti $3d$ -S $3p$ covalent bonding. A decrease in the bandgap was shown in the ellipsometry [Figure 3.10(a)] and ultra-violet spectrometry [Figure 3.10(b)] measurements of our pure and sulfurized PZT films. In these optical measurements, the band gaps were quantified to 3.41 and 3.32 eV for the pure and sulfurized PZT films, respectively [4,35]. And, the decrement of 0.09 eV by sulfur doping is comparable to that predicted in our theoretical calculations. It follows that the decrease of a bandgap by sulfurization is intrinsic, that is, not attributed to an extrinsic effect (e.g. the formation of an intermediate defect level between VBM and CBM [4]).

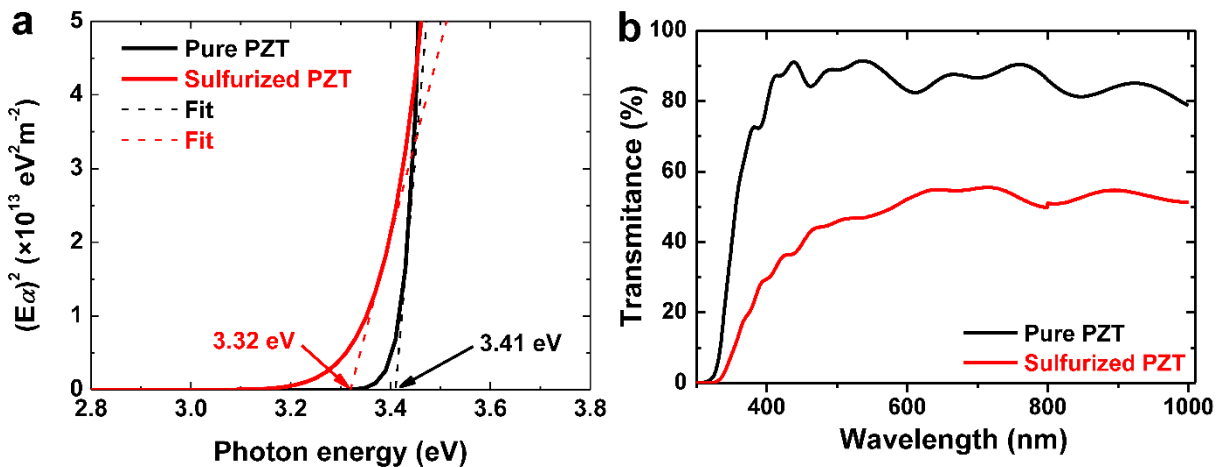


Figure 3.10 The electronic band-gap measurements of pure and sulfurized $\text{Pb}(\text{Zr}_{0.52}\text{Ti}_{0.48})\text{O}_3$ films. (a) The bandgap measurement of pure and sulfurized PZT films on $\text{SrRuO}_3/\text{SrTiO}_3$ (001) substrates using ellipsometry. Here, $(E\alpha)^2$, where E and α is the photon energy and the absorption coefficient, respectively, was plotted as a function of the photon energy (eV). (b) ultraviolet-visible spectrometry of pure and sulfurized PZT films on fluorine-doped tin oxide (FTO) coated glass substrates.

3.8 Discussion: Origin of enhanced ferroelectricity in perovskite oxysulfides

To elucidate the origin of the enhanced ferroelectricity in our PZT oxysulfide films, we examined the responses of ferroelectric soft-phonon modes to sulfur doping using Raman spectroscopy (Figure 3.11). Note that there are 7 possible transverse optical (TO) phonon modes in perovskite PZT. Among these 7 TO phonon modes, only two phonon modes [i.e. horizontal E(1TO) and vertical A₁(1TO)] modes are ferroelectric soft modes in PZT, where the ferroelectric polarization mostly arises from A-site Pb displacements with respect to apical oxygen atoms [36]. It is evident that the two modes are down-shifted towards lower wavenumbers after sulfurization [black left arrows in Figure 3.11(a)]. In contrast, non-ferroelectric soft modes [i.e. E(2TO) and E(3TO)] remain unchanged with the initial wavenumber [red downward arrows in Figure 3.11(a) and (b)], when a ferroelectric PZT film is sulfurized. Considering the fact that the soft phonon mode shifts are mainly activated with changes in ferroelectric properties [37], the observed peak shift in the ferroelectric Raman modes should be attributed to the increase of structural tetragonality (i.e. the elongation and shrinkage along the out-of-plane and in-plane directions, respectively) and thereby, the enhancement of ferroelectric polarization by sulfurization.

More interestingly, another two phonon modes [i.e. A₁(2TO) and A₁(3TO)] are upper-shifted towards higher wavenumbers after sulfurization [blue right arrows in Figure 3.11(a) and (b)]. We note that these two phonon modes are very susceptible to the chemical bonding nature between the B-site transition-metal *d* and the apical oxygen *p* orbitals in ABO₃ perovskite oxides [38,39]. Explicitly, the frequency of A₁(2TO) and A₁(3TO) modes is described as

$$f = \frac{1}{2\pi} \sqrt{\frac{k}{m}}, \quad (1)$$

where *k* is the force constant depending on the bonding strength of the B-O hybridization [the Ti or Zr-O (S) bonding in PZT (PZT oxysulfide)] and *m* is the atomic mass of the B-site cation

[Ti⁴⁺ or Zr⁴⁺ ion] [40]. Here, we stress that the Ti 3*d*-S 3*p* bonding is more covalent compared with the Ti 3*d*-O 2*p* bonding due to the lower electronegativity of the sulfur element than the oxygen atom [1]. As shown in Figure 3.10(c), such strong covalency of the Ti-S (apical) bonding gives rise to a larger force constant (k_2) than the Ti-O (apical) bonding (k_1), inducing an increase in the phonon frequency, that is, an upper shift in the corresponding wavenumber. The force constant observed from the Raman spectrum is the statistical average of the two (fluctuating Ti-S and Ti-O) bond strengths. Accordingly, it is highly plausible that an apical oxygen atom is replaced by a sulfur atom and the linked ferroelectric phonon modes are further softened in the PZT oxysulfides.

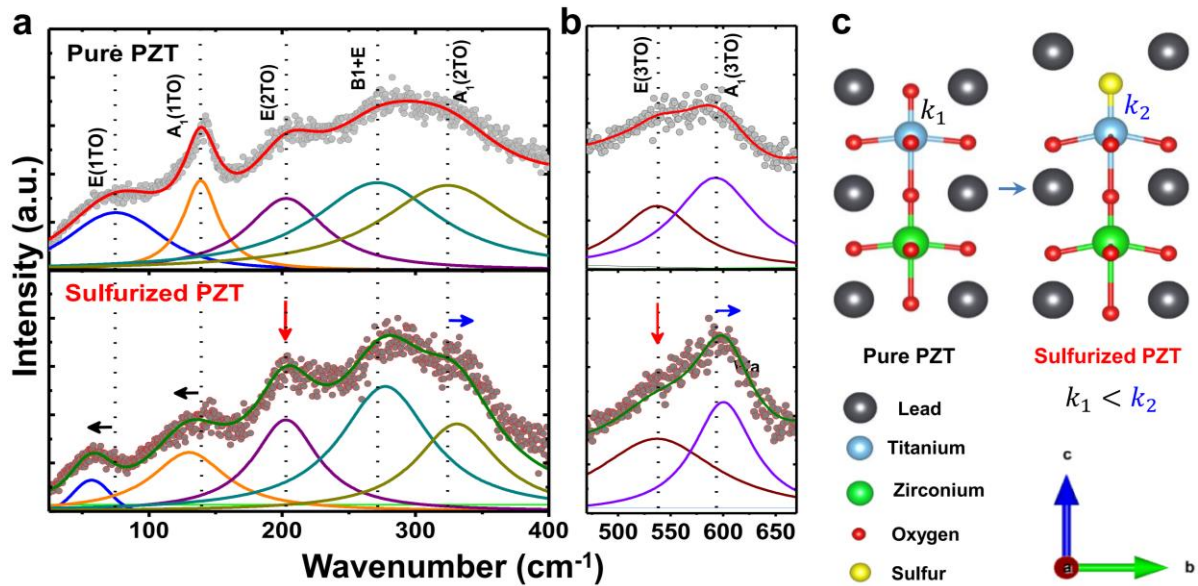


Figure 3.11 The Raman spectroscopy of pure and sulfurized $\text{Pb}(\text{Zr}_{0.52}\text{Ti}_{0.48})\text{O}_3$ films. Room temperature Raman spectra of pure and sulfurized PZT films in the wavenumber ranges (a) 25 to 400 cm^{-1} and (b) 470 to 670 cm^{-1} . (c) Schematic demonstration of the structural transition via sulfur doping in PZT films.

3.9 Implications

The data in the ferroelectric random access memory (FeRAM) can be store using the spontaneous polarization of perovskite ferroelectrics. An external electric field can switch the polarization direction ‘0’ and ‘1’. Despite its great promise, FeRAM has a low attraction in today’s memory market, mainly due to process integration and cost issues. On the other side, the observation of the photovoltaic effect in the ferroelectric materials has proposed the use of the photovoltaic effect for information transfer and storing applications.

In this work, the enhancements in the structural tetragonality and the ferroelectric polarization are attained, whereas the bandgap in the electronic band structure is reduced. Conceptually, our work can be utilized for the artificial design of new ferroelectric photovoltaic devices with high efficiency and multi-functionality.

References

- [1] J. A. Brehm, H. Takenaka, C. W. Lee, I. Grinberg, J. W. Bennett, M. R. Schoenberg, and A. M. Rappe, *Phys. Rev. B* **89**, 195202 (2014).
- [2] G. Amarsanaa, D. Odkhuu, C. W. Ahn, and I. W. Kim, *J. Appl. Phys.* **116**, 194105 (2014).
- [3] S. Pereraa, H. Hui, C. Zhao, H. Xue, F. Sun, C. Deng, N. Gross, C. Milleville, X. Xu, D. F. Watson, B. Weinstein, Y.-Y. Sun, S. Zhang, and H. Zeng, *Nano Energy* **22**, 129 (2016).
- [4] S. M. Lee, and Y. S. Cho, *Dalton Trans.* **45**, 5598 (2016).
- [5] F.-F. Li, D.-R. Liu, G.-M. Gao, B. Xue, and Y.-S. Jiang, *Appl. Catal. B-Environ.* **166**, 104 (2015).
- [6] A. Ishikawa, Y. Yamada, T. Takata, J. N. Kondo, M. Hara, H. Kobayashi, K. Domen, *Chem. Mater.* **15**, 4442 (2003).
- [7] R. D. Shannon, and C. T. Prewitt, *Acta Crystallogr. B* **25**, 925 (1969).
- [8] R. D. Shannon, *Acta Crystallogr. A.* **32**, 751 (1976).
- [9] S. Niu, H. Huyan, Y. Liu, M. Yeung, K. Ye, L. Blankemeier, T. Orvis, D. Sarkar, D. J. Singh, R. Kapadia, and J. Ravichandran, *Adv. Mater.* **29**, 1604733 (2017).
- [10] A. Clearfield, *Acta Crystallogr.* **16**, 135 (1963).
- [11] Y. Wang, N. Sato, and T. Fujino, *J. alloys compd.* **327**, 104 (2001).
- [12] M. Itoh, and Y. Inabe, *Phys. Rev. B* **68**, 035107 (2003).
- [13] B. Okai, K. Takahashi, M. Saeki, and J. Yoshimoto, *Mater. Res. Bull.* **23**, 1575 (1988).
- [14] I. Bilgin, F. Liu, A. Vargas, A. Winchester, M. K. L. Man, M. Upmanyu, K. M. Dani, G. Gupta, S. Talapatra, A. D. Mohite, and S. Kar, *ACS nano* **9**, 8822 (2015).
- [15] J. Ma, K. Tang, H. Mao, J. Ye, S. Zhu, Z. Xu, Z. Yao, S. Gu, and Y. Zheng, *Appl. Surf. Sci.* **435**, 297 (2018).

- [16] R. Lelieveld, and D. Ijdo, *Acta Crystallogr. Sec. B: Struct. Crystallogr. Cryst. Chem.* **36**, 2223 (1980).
- [17] S. B. Zhang, and J. E. Northrup, *Phys. Rev. Lett.* **67**, 2339 (1991).
- [18] B. Noheda, J. A. Gonzalo, L. E. Cross, R. Guo, S. E. Park, D. E. Cox, and G. Shirane, *Phys. Rev. B* **61**, 8687 (2000).
- [19] B. Noheda, D. E. Cox, G. Shirane, J. Gao, and Z.-G. Ye, *Phys. Rev. B* **66**, 054104 (2002).
- [20] B. Noheda, D. E. Cox, G. Shirane, J. A. Gonzalo, L. E. Cross, and S.-E. Park, *Appl. Phys. Lett.* **74**, 2059 (1999).
- [21] C. S. Tu, V. H. Schmidt, I. C. Shih, and R. Chien, *Phys. Rev. B* **67**, 020102(R) (2003).
- [22] M. Davis, D. Damjanovic, and N. Setter, *Phys. Rev. B* **73**, 014115 (2006).
- [23] F. Bai, N. Wang, J. Li, and D. Viehland, *J. Appl. Phys.* **96**, 1620 (2004).
- [24] B. Noheda, Z. Zhong, D. E. Cox, G. Shirane, S.-E. Park, and P. Rehrig, *Phys. Rev. B* **65**, 224101 (2002).
- [25] R. Chien, V. H. Schmidt, C.-S. Tu, L.-W. Hung, and H. Luo, *Phys. Rev. B* **69**, 172101 (2004).
- [26] Z. Chen, Z. Luo, C. Huang, Y. Qi, P. Yang, L. You, C. Hu, T. Wu, J. Wang, C. Gao, T. Sritharan, and L. Chen, *Adv. Funct. Mater.* **21**, 133 (2011).
- [27] H. M. Christen, J. H. Nam, H. S. Kim, A. J. Hatt, and N. A. Spaldin, *Phys. Rev. B* **83**, 144107 (2011).
- [28] Y. J. Ko, D. Y. Kim, S. S. Won, C. W. Ahn, I. W. Kim, A. I. Kingon, S.-H. Kim, J.-H. Ko, and J. H. Jung, *ACS Appl. Mater. Interfaces* **8**, 6504 (2016).
- [29] X. Tang, and D. Li, *J. Phys. Chem. C* **112**, 5405 (2008).
- [30] D. Gonbeau, C. Guimon, G. P.-Guillouzo, A. Levasseur, G. Meunier, and R. Dormoy, *Surf. Sci.* **254**, 81 (1991).

- [31] D. I. Sayago, P. Serrano, O. Böhme, A. Goldoni, G. Paolucci, E. Román, and J. A. Martín-Gago, *Phys. Rev. B* **64**, 205402 (2001).
- [32] T. Umebayashi, T. Yamaki, H. Itoh, and K. Asai, *Appl. Phys. Lett.* **81**, 454 (2002).
- [33] M. F. Chisholm, W. Luo, M. P. Oxley, S. T. Pantelides, and H. N. Lee, *Phys. Rev. Lett.* **105**, 197602 (2010).
- [34] D. Lee, S. H. Baek, T. H. Kim, J.-G. Yoon, C. M. Folkman, C. B. Eom, and T. W. Noh, *Phys. Rev. B* **84**, 125305 (2011).
- [35] M. W. Chu, I. Szafraniak, R. Scholz, C. Harnagea, D. Hesse, M. Alexe, and U. Gosele, *Nat. Mater.* **3**, 87 (2004).
- [36] D. A. Tenne, P. Turner, J. D. Schmidt, M. Biegalski, Y. L. Li, L. Q. Chen, A. Soukiassian, S. Trolier-McKinstry, D. G. Schlom, X. X. Xi, D. D. Fong, P. H. Fuoss, J. A. Eastman, G. B. Stephenson, C. Thompson, and S. K. Streiffer, *Phys. Rev. Lett.* **103**, 177601 (2009).
- [37] J. D. Freire, and R. S. Katiyar, *Phys. Rev. B* **37**, 2074 (1988).
- [38] M. K. Zhu, P.-X. Lu, Y.-D. Hou, X. M. Song, H. Wang, and H. Yan, *J. Am. Ceram. Soc.* **89**, 3739 (2006).
- [39] D. Fu, T. Ohno, T. Ogawa, H. Suzuki, K. Ishikawa, and T. Hayashi, *Jpn. J. Appl. Phys.* **39**, 5687 (2000).
- [40] X. Yang, X. Su, M. Shen, F. Zheng, Y. Xin, L. Zhang, M. Hua, Y. Chen, and V. G. Harris, *Adv. Mater.* **24**, 1202 (2012).

Chapter 4

Stress-driven high electro-strain in BNT-based ceramics at a low applied field

4.1 Bismuth based perovskites oxides

Perovskite oxides ABO_3 , the crystal structure consists of the corner-linked octahedra of oxygen “O” atoms (anions) with “B” cations at their centers and “A” cations in the interstices formed by the oxygen octahedra. The name “perovskite” is given to a large number of crystal structures based on the first discovered mineral $CaTiO_3$, named after the Russian mineralogist Count Lev Aleksevich von Perovski.

There are many perovskite structures, such as lead (Pb) based perovskites, which are promising for piezoelectric ceramics. However, Considering the toxicity and atmospheric impact of lead-based materials, the bismuth-based piezoceramics, such as $Bi_{1/2}Na_{1/2}TiO_3$ (BNT) is a relaxor-ferroelectric with rhombohedral symmetry at room temperature and pressure. The BNT has been considered as a building block towards lead-free actuator devices owing to their robust strain response [1–4]. However, the large strain hysteresis and large electromechanical strain at a high driving electric field restrict their utilization for the practical actuating application. Large strain response in $BaTiO_3$ modified BNT (BNT–BT), and $Bi_{1/2}K_{1/2}TiO_3$ modified BNT (BNT–BKT) ceramics have been reported so far either by making solid solutions or by doping a single element [5,6-9].

4.2 Inversion symmetry breaking by ferroelectric particles

In this study, by adding the ferroelectric $\text{Bi}_{1/2}(\text{Na}_{0.78}\text{K}_{0.22})_{1/2}\text{TiO}_3$ (BNKT) particles (volume percent fraction) to the relaxor the $0.72\text{Bi}_{1/2}\text{Na}_{1/2}\text{TiO}_3\text{-}0.28\text{SrTiO}_3$ (BNT-28ST), the spatial inversion symmetry in perovskite BNT-28ST is uniformly lifted resulting in a high piezoelectric response at a low applied field in the BNT-28ST/BNKT ceramic composite. A relaxor $0.72\text{Bi}_{1/2}\text{Na}_{1/2}\text{TiO}_3\text{-}0.28\text{SrTiO}_3$ (BNT-28ST) was chosen as a base material due to its high normalized strain response [10]. In order to generate a stress-induced high electrostrain at a reasonably low driving field, the ferroelectric plate-type $\text{Bi}_{1/2}(\text{Na}_{0.78}\text{K}_{0.22})_{1/2}\text{TiO}_3$ (BNKT) particles were applied to the BNT-28ST powders. We introduced the ferroelectric plate-type BNKT particles because of its high linear strain response (~ 293 pm/V) among the BNT-BKT system [11,12]. At a given applied electric field in BNT-28ST/BNKT composite, the BNKT ferroelectric particles are capable to compressively stressed the BNT-28ST relaxor ceramic and lifted the spatial inversion symmetry, resulting in high electrostrain.

4.3 Sample characterization

The microstructural images of layer-structured NBiT15 particles and plate-type BNKT particles are shown in Figure 4.1(a) and (b), respectively. A molten salt synthesis technique was used to prepare the NBiT15 particles. As seen in Figure 4.1(a), NBiT15 particles have a typical plate-type shape, which is believed to have stronger growth along the a - and b -axis than the c -axis [13,14]. After the successful fabrication of NBiT15 particles, a topochemical microstructural conversion technique was used to obtain plate-type BNKT ferroelectric particles (Figure 4.1(b)) [15]. In comparison to NBiT15 particles, an obvious increase in thickness was noticed in plate-type BNKT particles [13,14].

To confirm the crystalline structure, X-ray diffraction (XRD) measurement of NBiT15 particles and plate-type BNKT particles was performed in the 2θ range of $20\text{--}60^\circ$ (Figure 4.1(c) and (d)). The layered structure of NBiT15 particles was confirmed from the XRD profile [13,14], while plate-type BNKT particles have shown a single perovskite phase without any detectable secondary phase, which is in good agreement with the microstructural study [13,14]. The above microstructural and structural analyses confirm the successful growth (two steps molten salt method) of NBiT15 particles and plate-type BNKT particles [13–15].

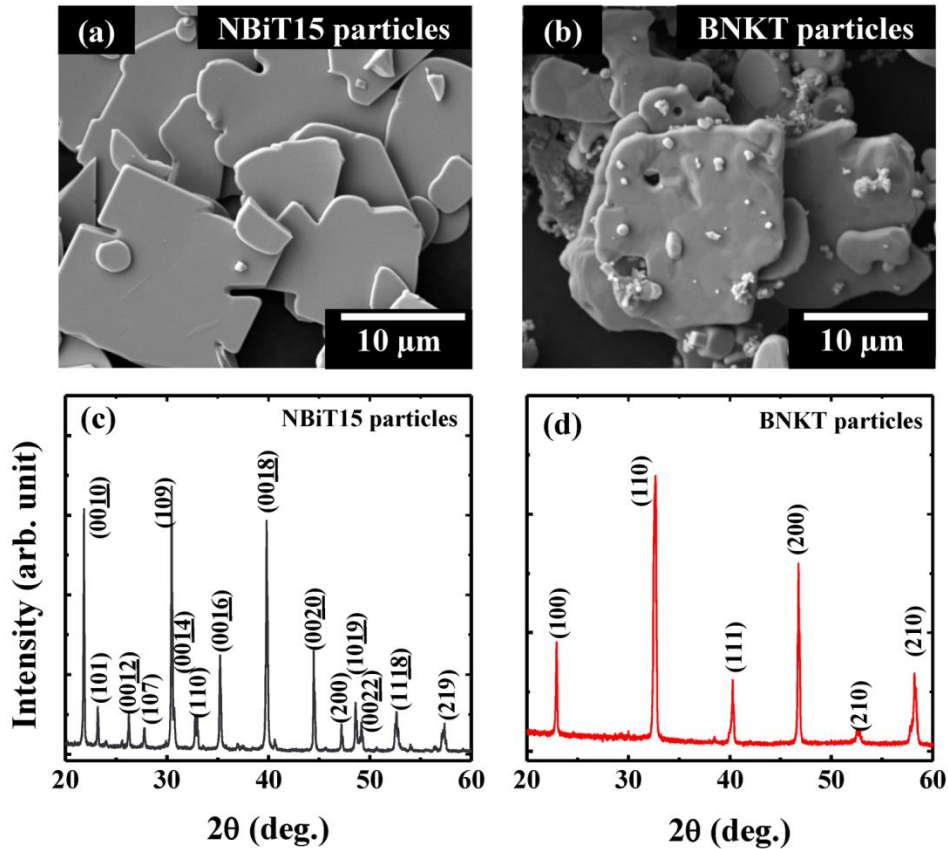


Figure 4.1 The FE-SEM images of (a) $\text{Na}_{0.5}\text{Bi}_{4.5}\text{Ti}_4\text{O}_{15}$ (NBiT15) particles (b) plate-type $\text{Bi}_{1/2}(\text{Na}_{0.78}\text{K}_{0.22})_{1/2}\text{TiO}_3$ (BNKT) perovskite particles, XRD patterns of (c) NBiT15 particles and (d) plate-type BNKT particles.

To get the insight into the ferroelectric induced-effect of the plate-type BNKT particles on the phase structure of relaxor BNT-28ST, XRD analyses of poled samples at an applied field of 4 kV/mm was carried out in the 2θ range of $10-70^\circ$, illustrated in Figure 4.2(a). In agreement with the reported study [10], pure BNT-28ST showed a single-phase perovskite structure with pseudocubic symmetry while the pure BNKT ceramic has the tetragonal symmetry. The addition of plate-type BNKT particles in different volume ratios have an obvious effect on the crystal structure of the BNT-28ST which can be seen in the enlarged T(002) and T(200) peaks, as seen in Figure 4.2(b). With the addition of the plate-type BNKT particles, it appears that tetragonal symmetry is structurally predominant. The XRD results suggest a mixed phase of relaxor and ferroelectric composite upon the addition of plate-type BNKT ferroelectric particles which are well reflected from microstructural images.

Figure 4.2 (c) presents the surface morphologies of pure BNT-28ST and 0-3 type composites with various volume ratios of 5, 10, and 15 vol.% plate-type BNKT particles. The BNT-28ST morphology consists of dense, well-defined grains with uniform distribution, throughout the material with circular grain shape and average grain size of $1.5 \mu\text{m}$. As usual, all the 0-3 type composites have mixed morphology, comprised of both small grains and large particles ($5.5 \mu\text{m}$). The large grains are the plate-type BNKT particles, surrounded by the smaller grains of BNT-28ST in Figure 4.2 (c).

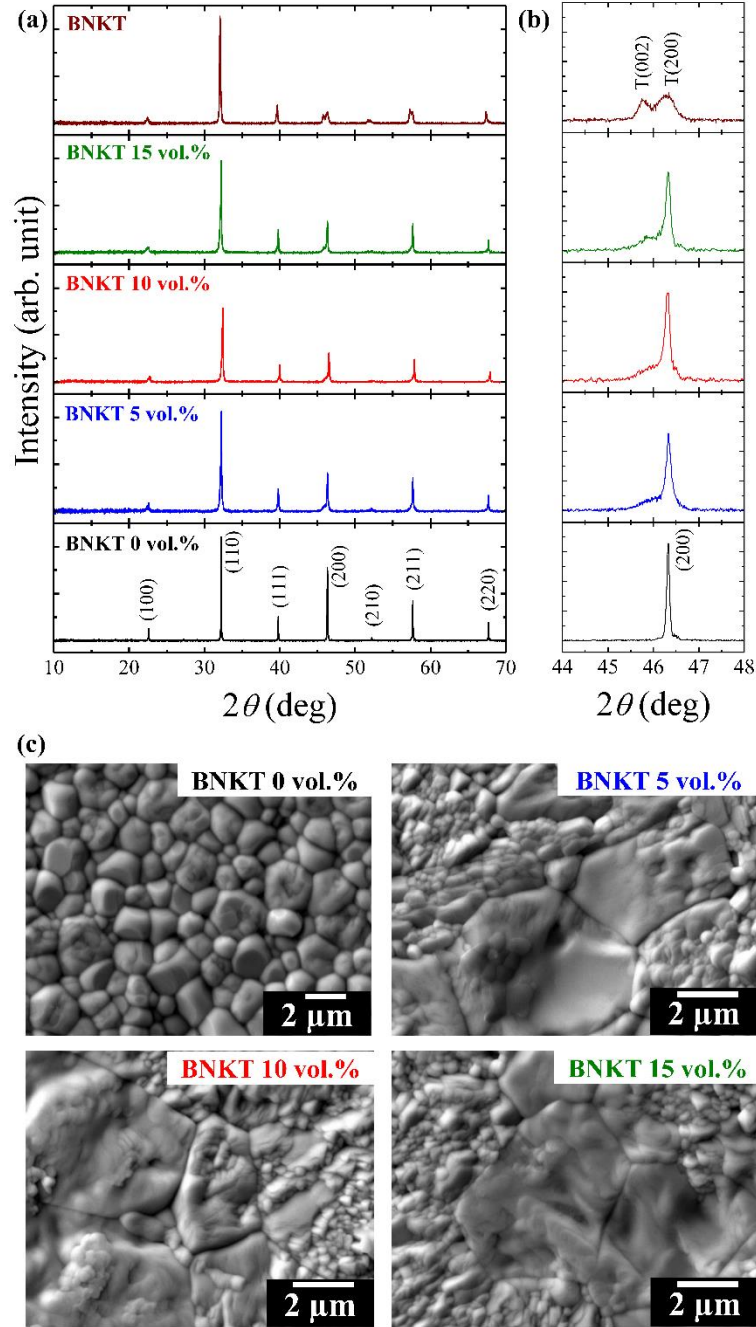


Figure 4.2 (a) XRD patterns of the of BNT–28ST/BNKT (0, 5, 10, and 15 vol.%) composites and pure BNKT ceramic in the 2θ range of $10\text{--}70^\circ$, (b) the enlarge (200) peak of the corresponding composites and pure BNKT. Figure 4.2 FE–SEM images of BNT–28ST/BNKT (0, 5, 10, and 15 vol.%) composites. The small size BNT–28ST relaxor particles are surrounding the large size ferroelectric particles.

4.4 Results: Explanation of high electro-strain at a low driving field

To analyze the effect of the ferroelectric plate-type BNKT particles on the relaxor BNT-28ST, the room temperature polarization and bipolar strain behavior were examined under the applied field of 5 kV/mm in Figure 4.3(a) and (b). The pure BNT-28ST sample showed a slim polarization hysteresis loop characterized by a small remnant polarization ($P_r = 4 \mu\text{C}/\text{cm}^2$) and coercive field ($E_c = 0.6 \text{ kV}/\text{mm}$), showing the features of an ergodic relaxor phase [3,8,16]. As expected, an obvious increase in remnant polarization and coercive field were noticed with the increasing vol.% content of plate-type BNKT particles, while slight variations in maximum polarization were witnessed as shown in Figure 4.3(d) and (e). At the highest ratio of the plate-type BNKT particles (15 vol.%), the remnant polarization and coercive field remarkably increased to $20 \mu\text{C}/\text{cm}^2$ and $2 \text{ kV}/\text{mm}$, respectively which is the hallmark of transition towards the ferroelectric phase [3,8,16]. The observed fashion in polarization parameters, along with the visible changes in hysteresis loops, demonstrates that the BNT-28ST ceramic transformed from an ergodic relaxor to a non-ergodic ferroelectric phase upon the addition of the ferroelectric plate-type BNKT particles at different BNKT content [3,8,16]. The depolarization fields (E_{dep}) which appear at the first inflection point of the electrical unloading in P - E hysteresis loops, is narrowly connected to the development in the field-induced strain [15,17]. Interestingly, it can be realized from Figure 4.3(a), that the depolarization field (E_{dep}) shifted towards a lower applied field in the plate-type BNKT added samples compared to that of the ergodic relaxor (BNT-28ST), which supported the high electrostrain under a low driving field [15,17]. The plate-type BNKT particles induced ergodic relaxor to a ferroelectric phase can be seen noticeably from bipolar strain hysteresis loops (Figure 4.3(b)). Consistent with the polarization hysteresis loop, BNT-28ST delivers large strain ($S = 0.29\%$) with nearly zero negative strain own to the ergodic relaxor nature

[16,17]. At a low fraction of plate-type BNKT added particles (5 vol.%), the maximum strain slightly decreased without any visible change in the negative strain. A noticeable increase in negative strain has appeared with the increasing volume fraction of plate-type BNKT particles. On the contrary, the maximum strain level dropped at a higher volume ratio of plate-type BNKT particles. The observed variations in polarization and strain parameters suggest that the nucleation sites (ferroelectric plate-type BNKT particles) turn as an activating source to enlarge the values of P_r and S_{neg} , the ergodic state is transformed into a ferroelectric phase [18].

The unipolar strain of BNT-28ST and its 0-3 type composites were examined under the applied electric field of 4 kV/mm (Figure 4.3(c)). The poling field (E_{pol}) of each composite has been marked with dashed lines. The unipolar strain behavior of all samples is well consistent with the polarization and bipolar strain loops (Figure 4.3(a) and (b)). It can be seen from Figure 4.3(c), that the pure BNT-28ST and the 5 vol.% composited sample display a relaxor like unipolar hysteresis loop with a comparable magnitude of strain level. With further increase in the volume ratio of the plate-type BNKT particles, the maximum strain (S_{max}) level decreased as well as a considerable reduction in the hysteresis was perceived. The decrease in the S_{max} value of the 15 vol.% composited sample comes from the dominant normal ferroelectric behavior over the relaxor response in the composite ceramic [15,19,20].

In general, the poling field (E_{pol}) is the minimum applied field to boost up the electrostrain in incipient piezoelectric materials and has earned a special interest in designing piezoelectric materials for actuator application [15,17,20,21]. The E_{pol} extracted from the unipolar strain curves as a function of volume ratio of plate-type BNKT particles is provided in Figure 4.3(f) also schematically shown in the inset of Figure 4.3(f). Pure BNT-28ST ceramic had a high poling field ($E_{pol} = 2.95$ kV/mm) [22], an apparent decrease in the poling field was noticed with the increasing

ferroelectric plate-type BNKT particles content. At the 15 vol.% BNKT ferroelectric particles, the reduction in the poling field was near ~40 % of the pure BNT–28ST. Moreover, the maximum strain level showed a similar trend and decreased with increasing BNKT ferroelectric particles.

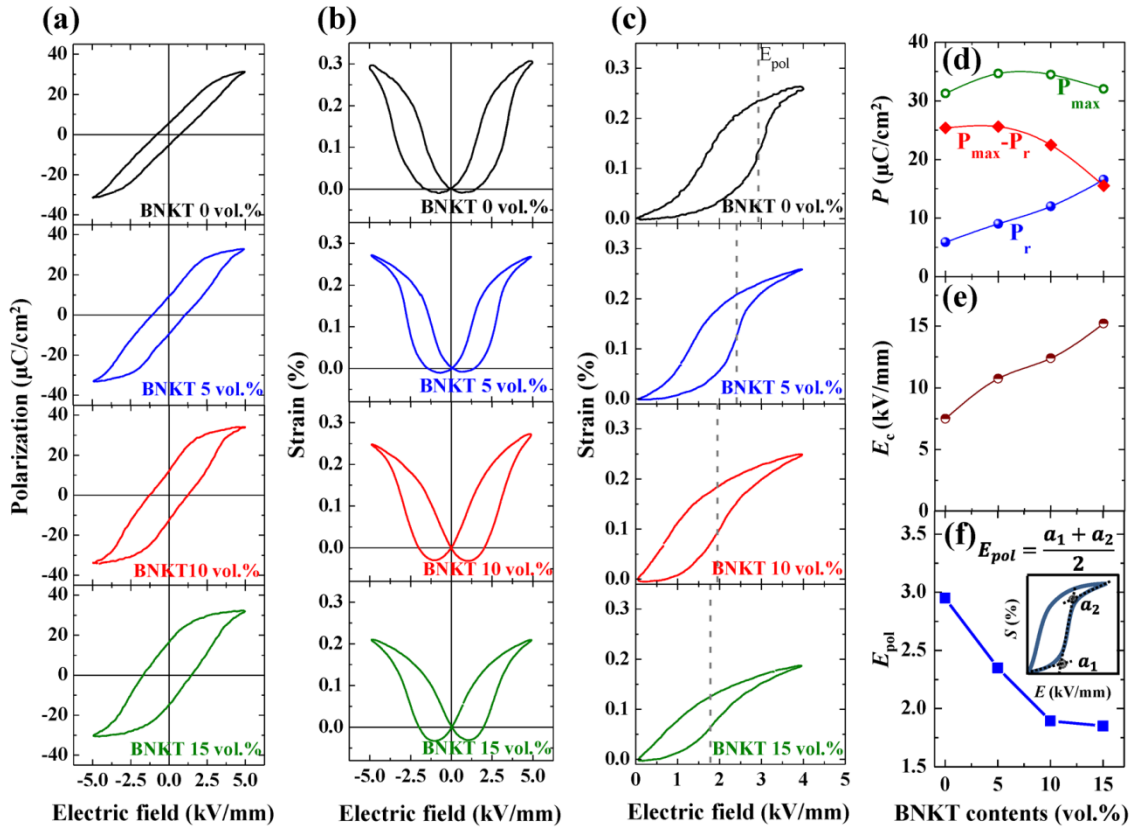


Figure 4.3 (a) Polarization, (b) bipolar, and (c) unipolar strain hysteresis loops of BNT–28ST/BNKT composites (0 vol.% to 15 vol.%). Extracted values of (d) polarization (P_{max} , P_r , and $P_{max} - P_r$), (e) coercive field (E_c), and (f) poling field (E_{pol}) with respect to plate-type BNKT content in vol.%. The bipolar and unipolar strain hysteresis loops were measured at the frequency of 0.2 Hz at room temperature. Schematic for the poling field (E_{pol}) is in the inset of Fig. 4(f). The poling field (E_{pol}) is marked with a black dashed line in all composited BNT–28ST/BNKT samples according to the schematic figure.

4.5 Discussion: Strain coupling mechanism in BNT-based composite ceramics

The polarization coupling mechanism and the series capacitor model in 0–3 type composite ceramics were reported responsible for reducing the poling field for high strain generation [15,18–20]. Apart from the polarization coupling mechanism and series capacitor model, the influence of other factors, such as interdiffusion at the boundary of the two end members, the presence of grain boundaries that impose a mechanical clamping among the neighboring grains, and the generation of internal residual stresses due to thermal and piezoelectric strains can also be encountered [20].

Recently, Zhang et al., suggested that the mismatch in the coefficient of thermal expansion of each component in the relaxor/ferroelectric composite yielded the variations in the electric response and residual stresses leading to changes in the macroscopic electrical constitutive behavior. Based on the stated proposition, the strain coupling model (SCM) in addition to the polarization coupling mechanism (PCM) and series capacitor model was considered to play an important role in the reduction of E_{pol} [20]. As the 10 vol.% composite sample shows a large normalized strain at a low driving field among all samples. Thus, field-dependent stress of the 10 vol.% BNT–28ST/BNKT composite sample was estimated from the unipolar strain loops (during the first and second field cycles). Figure 4.4(b) and (c) show the field-dependent unipolar strain of a ferroelectric BNKT (S_{FE}) and a relaxor BNT–28ST (S_{RE}), taken over the first (black line) cycle and second (yellow line) cycle Figure 4.4(a). Note that, the data presented here in the waveform, to clearly visualize the behavior of both ferroelectric and relaxor part. As can be seen from Figure 4.4(b), the strain value of the BNKT (blue line) increased with increasing the applied electric field, reached to a maximum value of 0.37% at 5 kV/mm. Upon the completion of the first triangular cycle, the ferroelectric BNKT material does not come back to its initial un–poled state and holds a new position called remnant strain equivalent to $S_{r,FE} = 0.225\%$, where the strain curve for the

ferroelectric BNKT (marked as a blue color curve) can be seen in Figure 4.4(f). The subsequent cycle (second loop) initiated from the new position (remnant strain) to the maximum strain value and return to the remnant strain state. The strain waveform of the relaxor part (marked as a red color curve in Figure 4.4(f)) revealed quite different behavior; returned to its initial un-poled state (zero remnant strain) when the applied field is removed, followed by the succeeding cycle.

Therefore, when we applied the electric field in the relaxor ferroelectric composite ceramics it would create stress at the grain boundaries between the relaxor and ferroelectric grains because of the appearance of the difference in strain response ($S_{FE} - S_{RE}$). Figure 4.4(b) and (c) show the $S_{FE} - S_{RE}$, and stress (σ_{RE}), respectively, extracted from the unipolar strain loop during the first and second poling cycle as a function of the applied field. The observed behavior suggested that with the addition of plate-type BNKT (ferroelectric) particles to BNT-28ST (relaxor matrix), the development of tensile stress on the relaxor matrix is highly expected due to the different strain responses ($S_{FE} - S_{RE} > 0$) under the applied field (Figure 4.4(d)) [20]. This effect of the tensile stress can be easily understood in the strain loops response in Figure 4.4(f) for the two applied field cycles. In the case of the 10 vol.% composite sample, the small remnant strain value was noticed upon the completion of the first poling cycle due to the residual stress (strain loop is marked in black in Figure 4.4(g)). When the second subsequent cycle begins the strain loops initiated from the new remnant strain position [strain loop is marked in yellow in Figure 4.4(g)]. This remnant strain arises from the presence of the ferroelectric large size particles (plate-type BNKT) in the composite ceramics body. The non-zero remnant strain suggests that the ferroelectric long-range order exists in some volume fraction of the samples. Despite the transition from a relaxor to the ferroelectric state, the poling fields (E_{pol}) of the pure BNKT and BNT-28ST are relatively different as shown in Figure 4.4(f). Interestingly the reduction in the poling field

(E_{pol}) of the BNKT 10 vol.% composite sample (Figure 4.4(g)) is observed with nearly the same inflection points of the uphill in the strain loops to the pure BNKT as shown in Figure 4.4(f).

The residual stress in the two-phase system (ferroelectric and relaxor) can be computed when both phases have different elastic moduli [20]. The stress in the entire system for various volume ratios was calculated using the following equation:

$$\sigma_{RE} = S_{r,FE} \left[\frac{1}{Y_{RE}} + \frac{V_{RE}}{Y_{FE}V_{FE}} (1 + S_{r,FE}) \right]^{-1} \quad (1)$$

Where σ_{RE} is the internal stress in the relaxor part, Y is the isotropic elastic modulus, V is the volume ratio for the relaxor and ferroelectric materials, and $S_{r,FE}$ is the remnant strain of the ferroelectric part. The subscripts RE and FE indicate the relaxor and ferroelectric end members of the composite, respectively. The elastic moduli for the relaxor BNT–28ST (146 GPa) and ferroelectric BNKT (114 GPa) were obtained from the available literature [23–26]. The residual longitudinal stress as a function of BNKT content is illustrated in Figure 4.4(h). The calculated residual longitudinal stress values were 11.1, 22.5, and 33.8 MPa, for the BNKT content 5, 10, and 15 vol.%, respectively. Recently Martin et al., has reported that the stress-induced ferroelectric long-range order in the BNT based ceramic can be arises at the bias stress of about -200 MPa [27]. Lynch et al., has reported that the increasing external stress (compressive) can change the ferroelectric domain order in the soft PLZT ceramics [28]. The stress-strain curves at the applied stress of -6 MPa have shown the beginning of the depolarization which has changed the polarization–electric field (P – E) hysteresis loop to the pinched type hysteresis and has reduced the remnant polarization to 80% by increasing the stress up to -60 MPa [28]. Conversely to the external stress, in our case, the ferroelectric plat–type BNKT particles were used to stress internally the relaxor (BNT–28ST) domains. The calculated residual longitudinal stress values are comparable to the reported literature suggesting that such stress values can trigger the formation of the long–

order ferroelectric domains in the composites body [28]. The plate-type BNKT particles with 10 vol.% has shown the applied stress value of 22.5 MPa to the relaxor at 2 kV/mm in the composite. Such stress from the ferroelectric to relaxor can be considered responsible for the electric field induced large strain at low electric field upon the reduction in the poling field as shown in Figure 4.4(g).

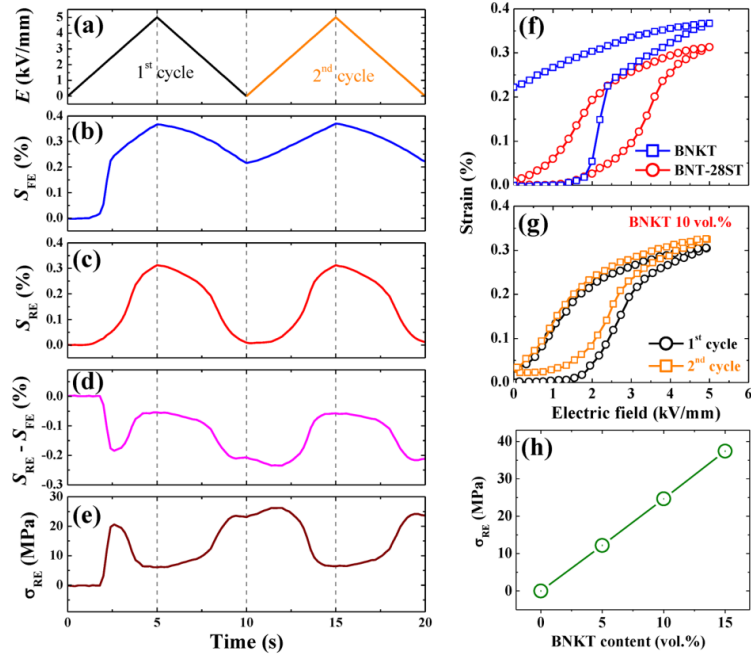


Figure 4.4 (a) The applied electric field for two cycles as a function of time for the measured parameters. The electric-field-induced electromechanical strain of (b) ferroelectric BNKT particles and (c) relaxor BNT-28ST. (d) The difference in strain responses ($S_{FE} - S_{RE}(\%)$) extracted from the unipolar strain as a function of field, (e) the field-dependent residual (longitudinal) stress (MPa). (f) The virgin strain response of the ferroelectric BNKT plate type particles and the relaxor BNT-28ST during the first cycle of the applied electric field, (g) the collective strain response of the 10 vol.% composite sample during the first and second cycle of the applied field, and (h) calculated residual (longitudinal) stress (MPa) after poling state as a function of BNKT content (vol.%).

To clearly understand the SCM, Figure 4.5(a)–(c) illustrates the schematic diagram of the strain coupling effect (a) before poling (b) under the applied field, and (c) after the applied (poling) field, during the first and second field cycle. Figure 4.5(a) presents the composite body, comprised as ferroelectric (FE) domain (green square block containing the black dashed domain boundaries) surrounded by the incipient relaxor domain (black square block containing the black dotted circular small domains) in the initial condition of zero applied electric field. Note that the unit cell of the relaxor BNT-28ST and ferroelectric BNKT is centrosymmetric and non-centrosymmetric as show in the 4.5(a). All the ferroelectric and relaxor domains are randomly oriented before the application of the electric field. However, under the operational field (at poling E_{pol} field of a ferroelectric part in the composite) the relaxor (centrosymmetric) part receives the stress from the ferroelectric (non-centrosymmetric) part in the composite body. The stress begins to establish due to the quick domain orientation response of the ferroelectric domain when the applied field reached the inflection point of the ferroelectric materials. Such a switching response of the ferroelectric domain stresses the relaxor part in the composite body by experiencing the elongation (shown by red color) in the direction of the field while compresses (shown by blue color) in the direction perpendicular to the external field as depicted in Figure 4.5(b). Under such stress state, the inversion symmetry of the centrosymmetric relaxor (BNT-28ST) break to non-centrosymmetric Figure 4.5(b). The ferroelectric part stresses the relaxor part in the composite body due to its low poling field resulting in the large electric field-induced strain at a low driving field. When the external field is reduced to zero, the composite body does not restore its initial position (before poling), illustrating that the composite body remains under the stress condition. In such a stress state, some of the relaxor region regain the initial state (centrosymmetric) forming the black dotted circular relaxor domains while some part remains under stress state (due to the presence of the remnant strain) as shown by

the extended ferroelectric domain boundaries (black dashed lines) in Figure 4.5(c). This happens due to the strain difference ($S_{FE} - S_{RE} > 0$) in the ferroelectric part (blue curve in Figure 4.4(f)) and the relaxor part (red curve in Figure 4.4(f)) of the composite. The stress-induced strain effect will continue upon the further applied cycle between, under the applied field state (Figure 4.5(b)), and after the poling field (Figure 4.5(c)), as illustrated by the yellow arrow directing to both sides. Thus, the large electromechanical strain at a low driving field is delivered due to the stress from the ferroelectric to the relaxor in the composite ceramic, as explained in the mechanism.

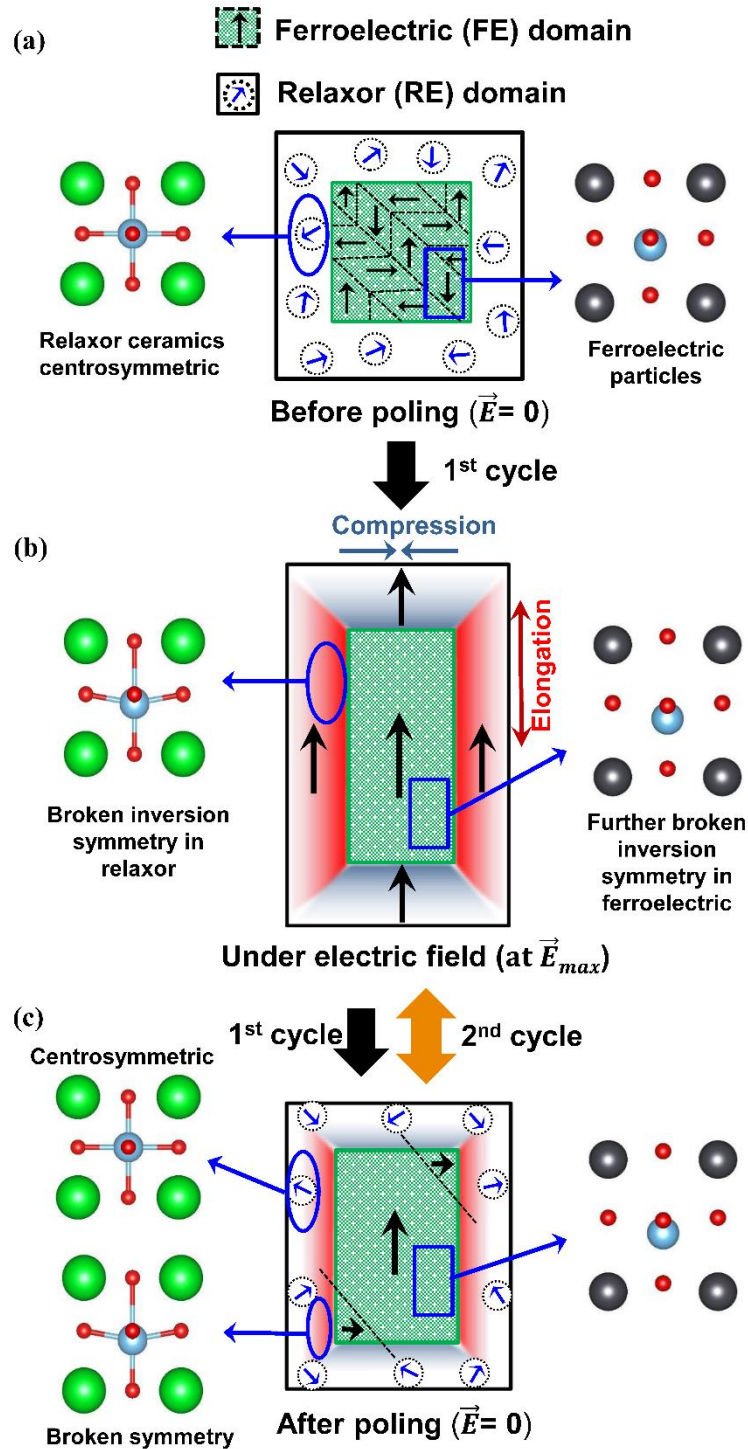


Figure 4.5 Schematic of strain coupling mechanism (a) before poling, (b) under the applied field, and (c) after poling. The tensile strain motif in the figure (b) and (c) is presented by the red color for elongated strain and blue as a compressive strain.

4.6 Device applications

The inverse piezoelectric effect is used to generate the displacement (x) and force (F) in a piezoelectric actuator. A direct multilayer piezoelectric actuator can be designed from the series connection of the ceramic pellets as shown in Figure 4.6. To produce accumulative displacement, these ceramic pellets are mechanically connected in series and electrically connected in parallel. Herein, in this work, the observed high normalized strain at low-field suggests that the relaxor-ferroelectric (BNT–28ST/BNKT) composite can be a desirable material for practical piezoelectric actuator devices.

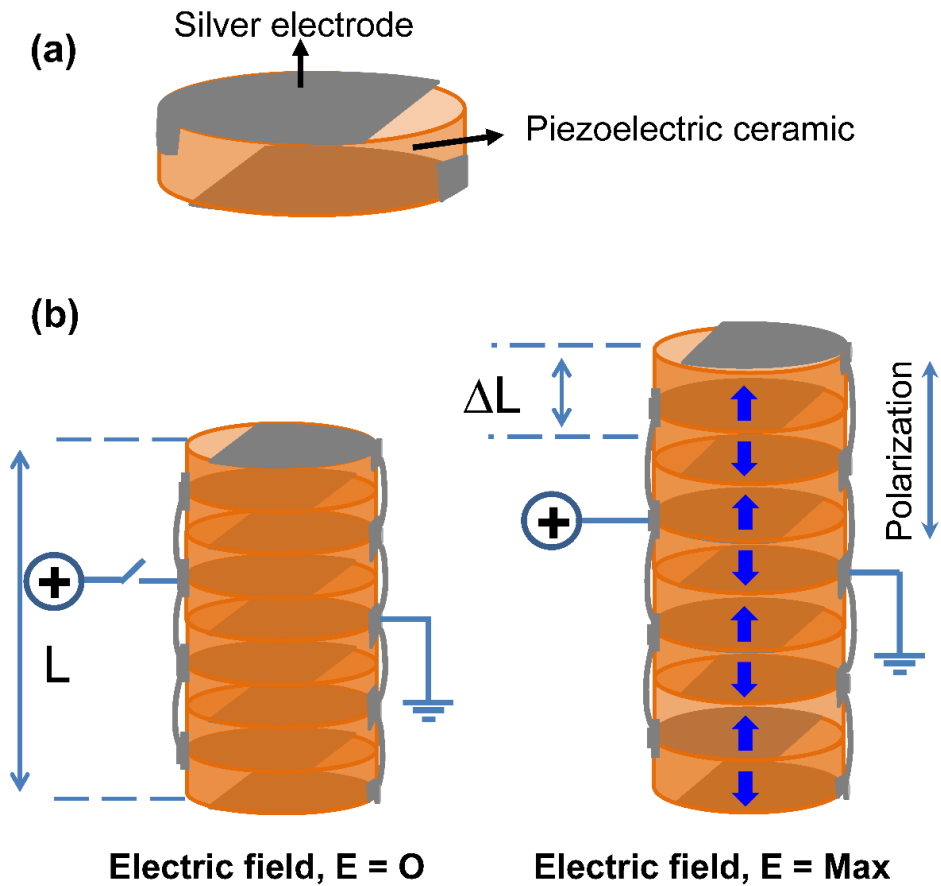


Figure 4.6 A schematic of a multilayer piezoelectric actuator under the electric field at zero and maximum electric field.

References

- [1] J. Rödel, and J. –F. Li, MRS Bull. **43**, 570 (2018).
- [2] A. J. Bell, O. Deubzer, MRS Bull. **43**, 581 (2018).
- [3] J. Rödel, K. G. Webber, R. Dittmer, W. Jo, M. Kimura, and D. Damjanovic, J. Eur. Ceram. Soc. **35**, 1659 (2015).
- [4] K. Shibata, R. Wang, T. Tou, and J. Koruza, MRS Bull. **43**, 612 (2018).
- [5] W. Jo, R. Dittmer, M. Acosta, J. Zang, C. Groh, E. Sapper, K. Wang, and J. Rödel, J. Electroceram. **29**, 71 (2012).
- [6] S. T. Zhang, A. B. Kounga, E. Aulbach, T. Granzow, W. Jo, H. J. Kleebe, and J. Rödel, J. Appl. Phys. **103**, 034107 (2008).
- [7] T. Takenaka, K. I. Maruyama, and K. Sakata, Jpn. J. Appl. Phys. **30**, 2236 (1991).
- [8] A. Ullah, C. W. Ahn, A. Ullah, I. W. Kim, Appl. Phys. Lett. **103**, 022906 (2013).
- [9] T. H. Dinh , V. D. N. Tran, T. T. Nguyen, Q. T. N. Hoang, H. S. Han, and J. S. Lee, Ceram. Int. **43**, 17160 (2017).
- [10] Y. Hiruma, Y. Imai, Y. Watanabe, H. Nagata, and T. Takenaka, Appl. Phys. Lett. **92**, 262904 (2008).
- [11] K. Yoshii, Y. Hiruma, H. Nagata, T. Takenaka, Jpn. J. Appl. Phys. **45**, 4493 (2006).
- [12] A. Hussain, C. W. Ahn, J. S. Lee, A. Ullah, and I. W. Kim, Sens. Actuators A Phys. **158**, 84 (2010).
- [13] A. Hussain, J. U. Rahman, F. Ahmed, J. S. Kim, M. H. Kim, T. K. Song, and W. J. Kim, J. of Eur. Ceram. Soc. **35**, 919 (2015).

- [14] J. T. Zeng, K. W. Kwok, W. K. Tam, H. Y. Tian, X. P. Jiang, and H. L. W. Chan, *J. Am. Ceram. Soc.* **89**, 3850 (2006).
- [15] A. Khaliq, M. Sheeraz, A. Ullah, H. J. Seog, C. W. Ahn, T. H. Kim, S. Cho, and I. W. Kim, *Ceram. Int.* **44**, 13278 (2018).
- [16] A. Ullah, M. Alam, A. Ullah, C. W. Ahn, J. S. Lee, S. Cho, and I. W. Kim, *RSC Adv.* **6**, 63915 (2016).
- [17] C. Groh, D. J. Franzbach, W. Jo, K. G. Webber, J. Kling, L. A. Schmitt, H. J. Kleebe, S. J. Jeong, J. S. Lee, and J. Rödel, *Adv. Funct. Mater.* **24**, 356 (2014).
- [18] A. Khaliq, M. Sheeraz, A. Ullah, J. S. Lee, C. W. Ahn, I. W. Kim, *Sens. Actuators A Phys.* **258**, 174 (2017).
- [19] D. S. Lee, D. H. Lim, M. S. Kim, K. H. Kim, and S. J. Jeong, *Appl. Phys. Lett.* **99**, 062906 (2011).
- [20] H. Zhang, C. Groh, Q. Zhang, W. Jo, K. G. Webber, and J. Rödel, *Adv. Electron. Mater.* **1**, 1500018 (2015).
- [21] D. S. Lee, S. J. Jeong, M. S. Kim, and J. H. Koh, *J. Appl. Phys.* **112**, 124109 (2012).
- [22] T. A. Duong, H. -S. Han, Y. -H. Hong, Y. -S. Park, H. T. K. Nguyen, T. H. Dinh, and J. S. Lee, *J. Electroceramics* **41**, 73 (2018).
- [23] S. Jo, C. H. Hong, D. S. Kim, H. W. Kang, C. W. Ahn, H. G. Lee, S. Nahm, W. Jo, S. H. Han, *Sensors and Actuators A: Physical* **258**, 201 (2017).
- [24] J. Suchanicz, G. Klimkowski, M. Karpierz, U. Lewczuk, I. Faszczowy, A. Pękala, K. Konieczny, M. Antonova, and A. Sternberg, *IOP Conf. Ser.: Mater. Sci. Eng.* **49**, 012038 (2013).
- [25] R. Dittmer, W. Jo, K. G. Webber, J. L. Jones, and J. Rödel, *J. Appl. Phys.* **115**, 084108 (2014).
- [26] A. Sasaki, T. Chiba, Y. Mamiya, and E. Otsuki, *Jpn. J. Appl. Phys.* **308**, 5564 (1999).

[27] A. Martin, H. Uršič, T. Rojac, and K. G. Webber, *Appl. Phys. Lett.* **114**, 052901 (2019).

[28] C. S. Lynch, *Acta Mater.* **44**, 4137 (1996).

Chapter 5

Realization of 6H-hexagonal polymorphic phase in Al-doped SrMnO₃ oxide

5.1 Crystallographic structure of SrMnO₃ oxide and structural phase transition in SrMnO₃

The crystallographic structure of the SrMnO₃ exists in three polymorphs [i.e., cubic perovskite (*Pm-3m*), 4H-hexagonal (*P6₃/mmc*), and 6H-hexagonal structure (*P6₃/mmc*) [Figure 5.1 (a)-(c)]. These polymorphs are distinguished by their structure symmetry and the stacking sequence [1-10]. Based on these polymorphic phases, the complex oxide SrMnO₃ is a promising candidate due to its interesting physical properties such as ferroelectricity, ferromagnetic, magnetoelectric, electrocaloric, and so on [1-3,11-13]. These fascinating physical properties are closely connected to the crystallographic-structure of the SrMnO₃ [1-3,11-14]. Up to now, most of the theoretical and experimental studies have been focused on the cubic and 4H polymorphs of the SrMnO₃ due to their easy synthesis process [3,9,10,15]. However, a 6H polymorph has been rarely reported due to the challenging synthetic conditions (i.e., high temperature and pressure are required) [Figure 5.1(d)] [9,15-17]. Previously, a 6H SrMnO₃ polymorph was achieved in the SrMnO₃ by applying hydrostatic pressure (~6 GPa) using the diamond-anvil-cell (DAC) technique [9,15-17]. However, no alternative route is developed to achieve a 6H polymorph in SrMnO₃.

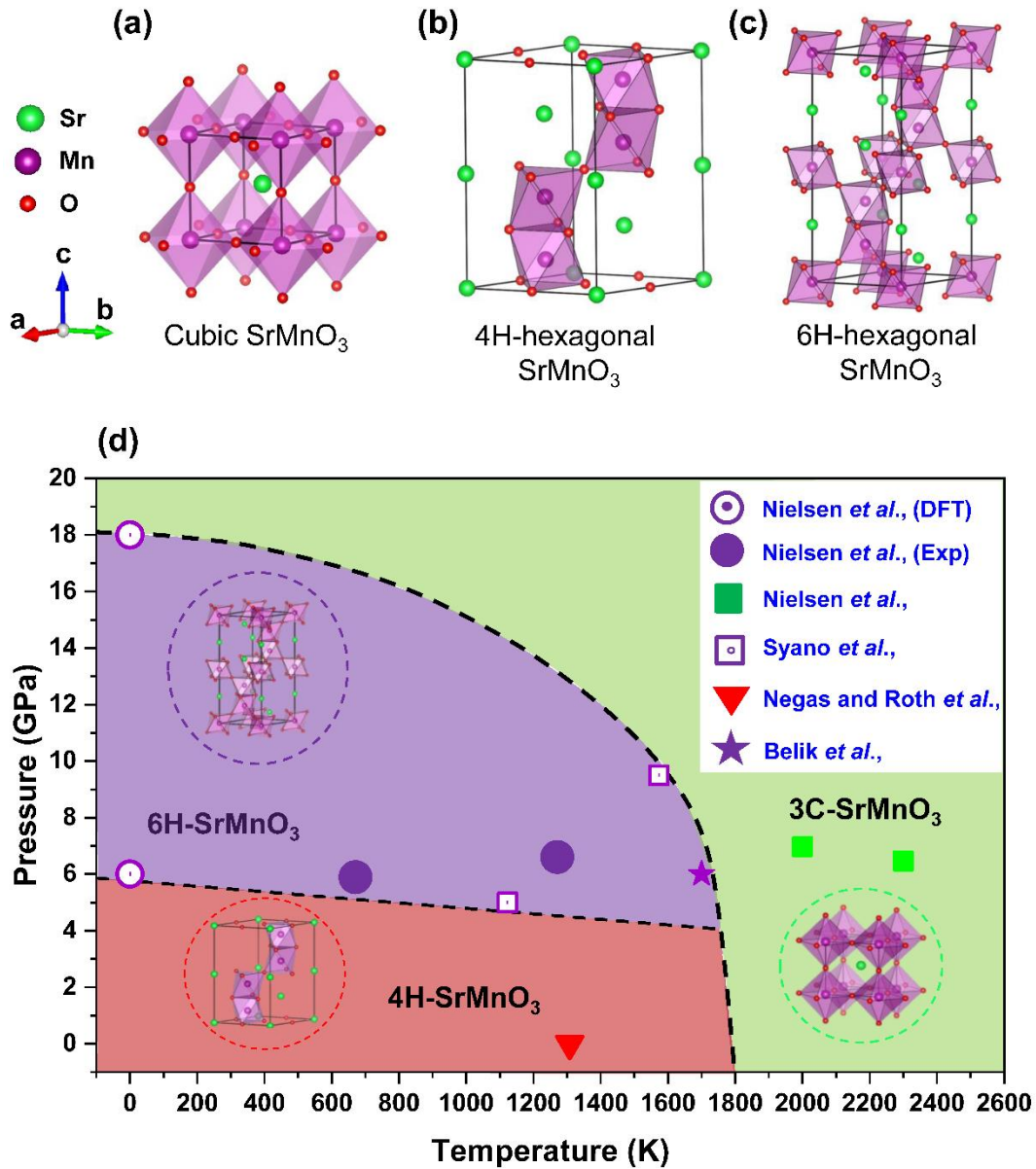


Figure 5.1 (a) In cubic perovskite SrMnO_3 structure, only corner-sharing can be observed. (b) An alternating face- and corner-sharing can be realized in 4H-hexagonal SrMnO_3 polymorph along a c -axis. (c) In a 6H SrMnO_3 polymorph, the degree of the corner-shared octahedra is raised from 4H SrMnO_3 [1-3]. The schematic illustration of the polymorphic SrMnO_3 phases at high pressure and temperature [7-9].

5.2 Hypothetical realization of 6H-hexagonal polymorph

To realize a 6H polymorph in SrMnO₃, we designed an alternative method without applying the external pressure. An interfacial strain mechanism (i.e., misfit strain at the grain boundaries of two unlike materials) is used rather than applying the hydrostatic pressure of ~6 GPa. Hypothetically, the interfacial strain arising from the lattice mismatch between two isosymmetric materials [i.e., 4H SrMnO₃ with another hexagonal material] can produce a stress value which leads us to successfully realize the 6H polymorph. Initially, we estimated the lattice parameter (5.17 Å) from the hydrostatic pressure value (i.e., ~6 GPa) required for achieving the 6H polymorph. As a 6H polymorph from a 4H polymorph of the SrMnO₃ can be achieved by hydrostatic pressure (~6 GPa) produced by the conventional diamond-anvil-cell (DAC).

Stress = Young's modulus × Strain

$$\sigma = E\epsilon \quad (1)$$

Here, σ is used for stress, E represents Young's modulus (115.6 GPa) and ϵ illustrates the strain produced due to the applied stress. The strain can be written as

$$\epsilon = \frac{\Delta L}{L} = \frac{a_{\text{SMO}} - a_{\text{U}}}{a_{\text{SMO}}} \quad (2)$$

Where a_{U} is used for the representation of the lattice parameter of the required (unknown) material.

Using equation (1) and (2) we can get

$$a_{\text{U}} = a_{\text{SMO}} \left(1 - \frac{\sigma}{E}\right) = 5.17 \text{ \AA} \quad (3)$$

Substituting the $a_{\text{SMO}} = 5.45 \text{ \AA}$, $\sigma = 6 \text{ GPa}$, and $E = 115.6 \text{ GPa}$, we found

$$a_{\text{U}} = 5.17 \text{ \AA}$$

Therefore, we need to develop another compound (lattice constant ~5.17 Å) locally in the proximity of the 4H SrMnO₃ to achieve a 6H polymorph from the 4H polymorph of the SrMnO₃.

Subsequently, we found that the hexagonal SrAl₂O₄ (*P*6₃22) with the lattice constant (5.167 Å) is comparable to the calculated (5.17 Å) value [18,19]. With this design strategy, we constructed the SrAl₂O₄ grains locally in the proximity to the 4H SrMnO₃ grains by doping the Aluminum (Al) to the SrMnO₃ [Fabrication process in chapter 2]. In the presence of the SrAl₂O₄ grains, it is feasible to generate the ultrahigh stress of ~6 GPa in proximity to SrMnO₃ grains [18,19]. The stress value required for realizing the 6H of polymorph from a 4H polymorph can be obtained using the following (ϵ) relation.

$$\sigma = E\epsilon = E \times \frac{a_{\text{SMO}} - a_{\text{SAO}}}{a_{\text{SMO}}} \quad (4)$$

Where σ is used for stress, E represents Young's modulus (115.6 GPa), a_{SMO} and a_{SAO} represent the lattice parameters of the SrMnO₃ and SrAl₂O₄, respectively.

$$\sigma = E\epsilon = 6.1 \text{ GPa}$$

The obtained stress value ($\sigma = 6.1$ GPa) is nearly identical as required for the realization of the 6H polymorph free from the application of external hydrostatic force.

To confirm our hypothesis, the Al-doped ($x = 0.00, 0.01, 0.02, 0.05, 0.10, \text{ and } 0.20$) SrMnO₃ ceramics were fabricated using the solid-state reaction technique. The Al₂O₃ powders at different mole ratios (x) were added to the mixer of SrCO₃ and MnO₂, respectively [Appendix A]. By examining the structural and chemical stoichiometry, we noticed that the 6H polymorph is achieved in the Al-doped SrMnO₃. Moreover, the phonon modes indicative of the presence of the 6H polymorph were additionally observed at the wavenumber 380, 596, and 778 cm⁻¹ using the Raman spectroscopy.

Furthermore, we evident via the first-principles calculations that the vacancies defects in the SrMnO₃ have no role to realize the 6H polymorph. Therefore, we clarified experimentally that the 6H polymorph can be realized by Al-doping to the SrMnO₃.

5.3 Inversion symmetry manipulation by interfacial strain

The origin of the off-center displacement of a transition metal (cation) in a perovskite structured ferroelectrics is the ligand-field hybridization (Ti $3d$ -O $2p$) of the transition metal (B-site) cation with its surrounding (oxygen) anions, like BaTiO₃ and Pb(Zr,Ti)O₃. However, in the hexagonal materials, such as YMnO₃ (space group), the inversion symmetry is broken by a tilting of the trigonal bipyramid resulting in the ferroelectric phase [20-21].

In this work, Al is doped to SrMnO₃ to produce the ferroelectric polarization in 6H-hexagonal SrMnO₃ ceramics with controlled spatial inversion symmetry. Herein, we constructed the hexagonal SrAl₂O₄ grains locally in the proximity to the 4H-hexagonal SrMnO₃ grains by doping the Aluminum (Al) to the SrMnO₃ ceramic. Using the interfacial strain mechanism, a 6H-hexagonal polymorph is realized in the SrMnO₃ polymorph identified in the x-ray diffraction analysis and Raman spectral measurements. We plan to generate the ferroelectric ordering by octahedral tilting in a 6H-hexagonal SrMnO₃ oxide. Then, the inversion symmetry in 6H-hexagonal SrMnO₃ is expected to be broken, which leads to a net electric polarization.

5.4 Results: Structural and chemical analyses

The x-ray diffraction (XRD) theta-2theta (θ - 2θ) examinations of the pure and Al-doped SrMnO₃ ceramics are shown in Figure 5.2. For pure SrMnO₃, the measured Bragg peaks positions are identical to the peak positions in the reference XRD of a 4H SrMnO₃ [Figure 5.2(a)] [6,15]. On the other side, as the Al-doping content (x) increases (i.e., $x = 0.01$), the diffraction peak of the 6H polymorph emerges and then pre-dominant at a higher-doping concentration ($x \geq 0.10$). We observed how the diffraction peaks evolve in the 2θ angles range 27-30°, 32-34°, 39-42°, and 46-50° as an increasing doping content x , as given in Figures 5.2(b)-(e) [6,15]. The crystallographic

structure of the SrAl_2O_4 is identified in the narrow XRD [27-30°] scan [Figure 5.2(b)] [18]. A 6H SrMnO_3 polymorph is verified in the enlarged XRD scans shown in Figures 5.2(c)-(e) [the reference XRD patterns 4H, 6H, and cubic SrMnO_3 are given in Figure 5.2(a)]. Note that the 6H peaks (at 32.74°, 39.88°, and 46.82°) co-existed with the 4H peaks (at 32.80°, 39.61°, and 48.84°) in the 2θ scan at lower Al concentration ($x = 0.01$) [6,17]. As the Al-doping content increases, 46.82° 6H peak becomes pre-dominant, which indicates that the 6H polymorph peaks are energetically favorable in heavily ($x \geq 0.10$) doped SrMnO_3 .

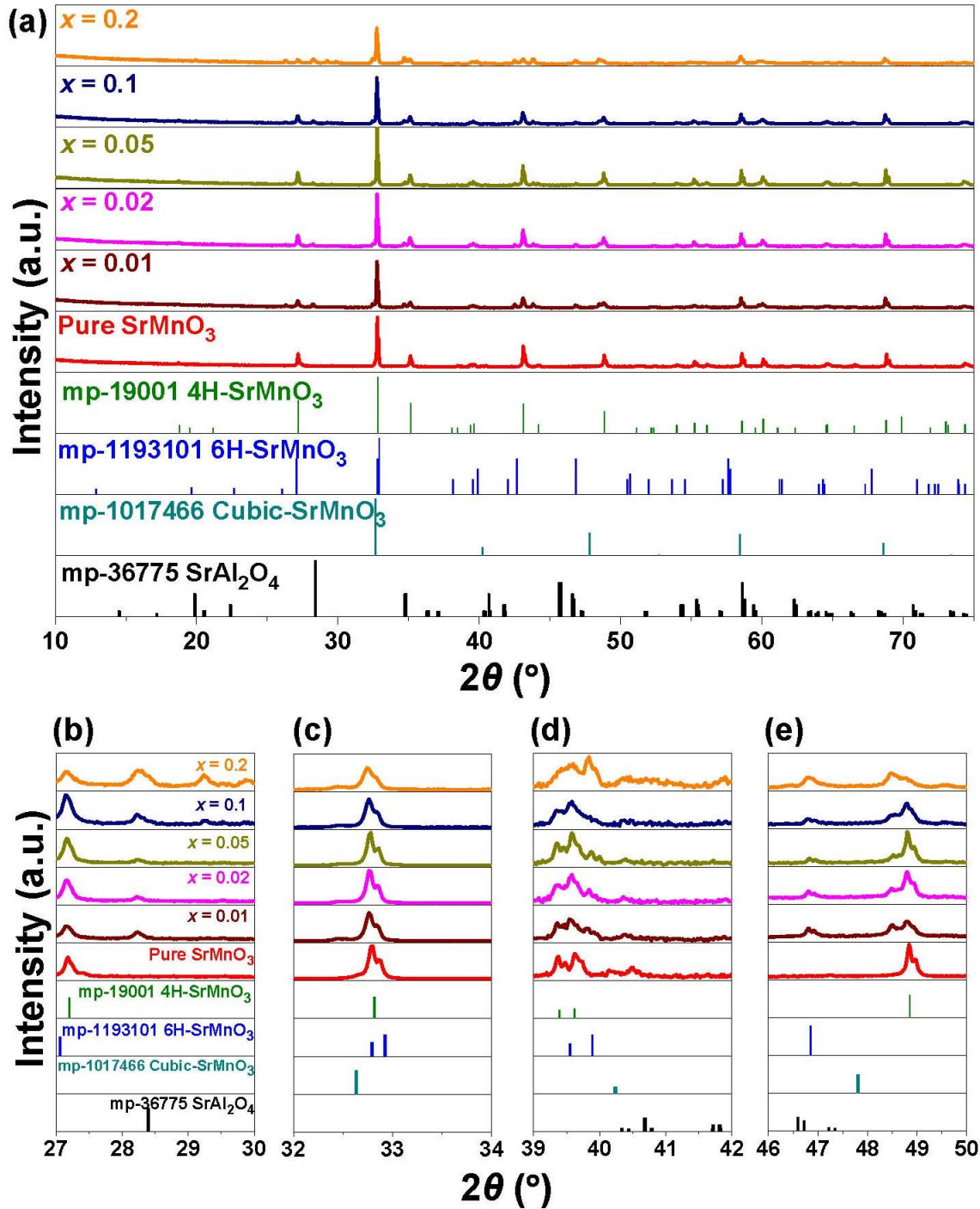


Figure 5.2 (a) XRD patterns of pure and Al-doped SrMnO₃ ceramics with various doping concentrations (x). The powder XRD scans of the 4H SrMnO₃ (green lines), 6H SrMnO₃ (blue lines), cubic-SrMnO₃ (cyan lines), SrAl₂O₄ (black lines), and MnO₂ (purple lines) are provided for comparison [17-19]. The enlarge XRD patterns in the 2θ range from (b) 27 to 30°, (c) 32 to 34°, (d) 46 to 50°.

To calculate the lattice parameters of 6H polymorph, we performed the XRD Rietveld refinement of the pure and Al-doped (0.10, and 0.20) SrMnO₃ samples via FullProf Suite [Figure 5.3] [22,23]. The Structural parameters of 4H SrMnO₃ (*P6₃/mmc*), 6H SrMnO₃ (*P6₃/mmc*), and SrAl₂O₄ (*P6₃22*) were used for the refinement of the pure and Al-doped SrMnO₃ ceramics [1,6]. The refined structural parameters of both (4H and 6H) SrMnO₃ polymorphs and SrAl₂O₄ are listed in Table 5.1, good agreement with the reported work [6,15,18,19]. Furthermore, the goodness of fit (χ^2) value of the pure and Al-doped ($x = 0.10$ and 0.20) SrMnO₃ is 5, 13, and 13.8, respectively. The high χ^2 comes from the presence of unknown secondary peaks which were not refined, as provided in Figure 5.3 (b,c).

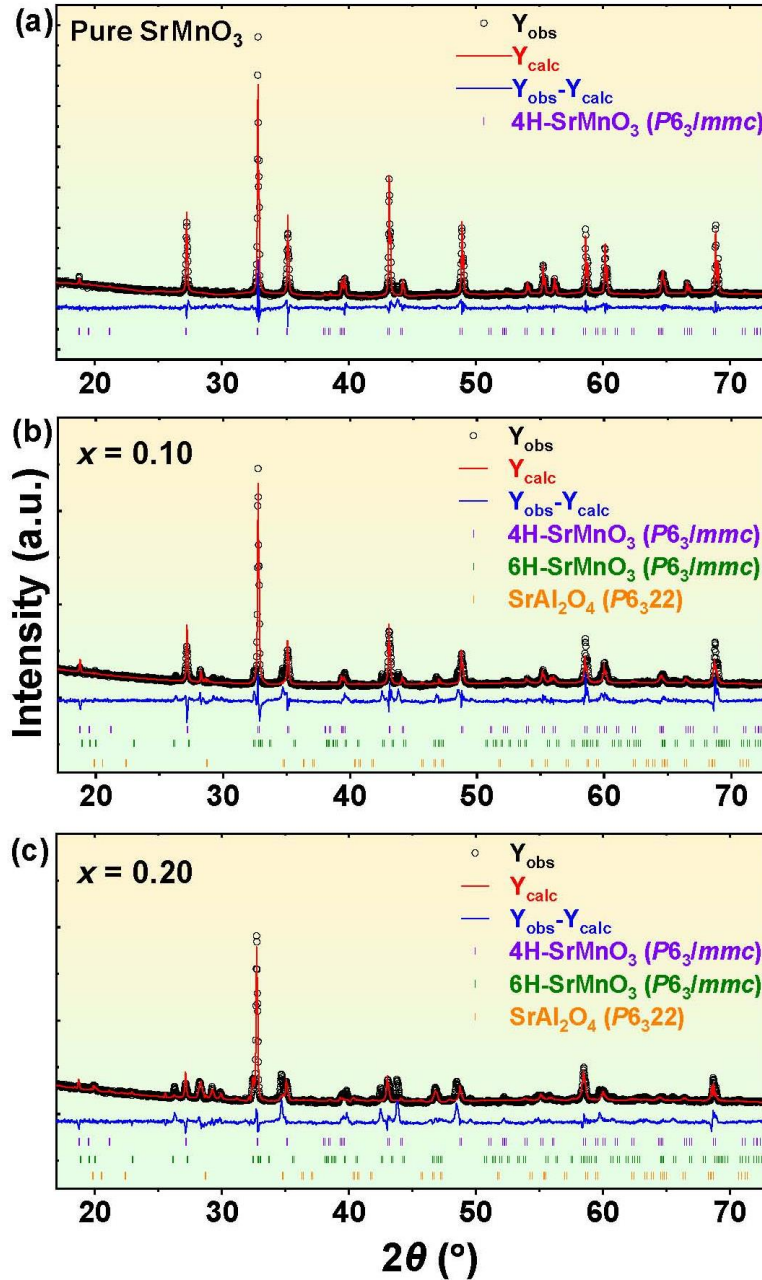


Figure 5.3 Rietveld refinement of XRD results of (a) pure SrMnO₃ and (b,c) Al-doped ($x = 0.10$, and 0.20) SrMnO₃ ceramics. The XRD fitted lines of the observed experimental (Y_{obs}), calculated (Y_{cal}), and the difference between observed and experimental ($Y_{\text{obs}} - Y_{\text{cal}}$) XRD profiles are denoted by black, red, and blue lines, respectively. The Braggs position of the 4H SrMnO₃, 6H SrMnO₃, and SrAl₂O₄ are represented via purple, olive, and orange color tick lines, respectively.

Table 5.1: The calculated lattice parameters of the 4H SrMnO₃, 6H SrMnO₃, and SrAl₂O₄ phase via Rietveld refinement of XRD patterns in the pure (0.00) SrMnO₃ and Al-doped (0.10, and 0.20) SrMnO₃ ceramic samples.

Pure and Al-doped SrMnO ₃		Space group	Lattice parameters (Å)		References
			<i>a</i> = <i>b</i>	<i>c</i>	
0.00	4H SrMnO ₃	<i>P6₃/mmc</i>	5.45	9.08	Present work
0.10	4H SrMnO ₃	<i>P6₃/mmc</i>	5.46	9.11	Present work
	6H SrMnO ₃	<i>P6₃/mmc</i>	5.42	13.63	
	SrAl ₂ O ₄	<i>P6₃22</i>	5.16	8.65	
0.20	4H SrMnO ₃	<i>P6₃/mmc</i>	5.46	9.11	Present work
	6H SrMnO ₃	<i>P6₃/mmc</i>	5.43	13.64	
	SrAl ₂ O ₄	<i>P6₃22</i>	5.16	8.67	
Previous works					
SrMnO ₃	4H SrMnO ₃	<i>P6₃/mmc</i>	5.45	9.09	[16]
SrMnO ₃	4H SrMnO ₃	<i>P6₃/mmc</i>	5.45	9.08	[3]
	6H SrMnO ₃	<i>P6₃/mmc</i>	5.43	13.40	
SrMnO ₃	4H SrMnO ₃	<i>P6₃/mmc</i>	5.45	9.08	[9]
	6H SrMnO ₃	<i>P6₃/mmc</i>	5.43	13.40	
SrAl ₂ O ₄	SrAl ₂ O ₄	<i>P6₃22</i>	5.17	8.46	[10,15]

To detect the Al presence in Al-doped SrMnO₃ ceramics, we performed the x-ray photoelectron spectroscopy (XPS) measurements at the Al 2*p* edges [Figure 5.4]. It should be noted that the increasing peak intensity in XPS data represents the increasing quantity of the specific atom represents [24,25]. We observed that the number of Al atoms increases upon the increasing Al-doping content (*x*) as shown in the plotted XPS [Figure 5.4] maximum peak intensity of the Al 2*p*-edge spectra [25].

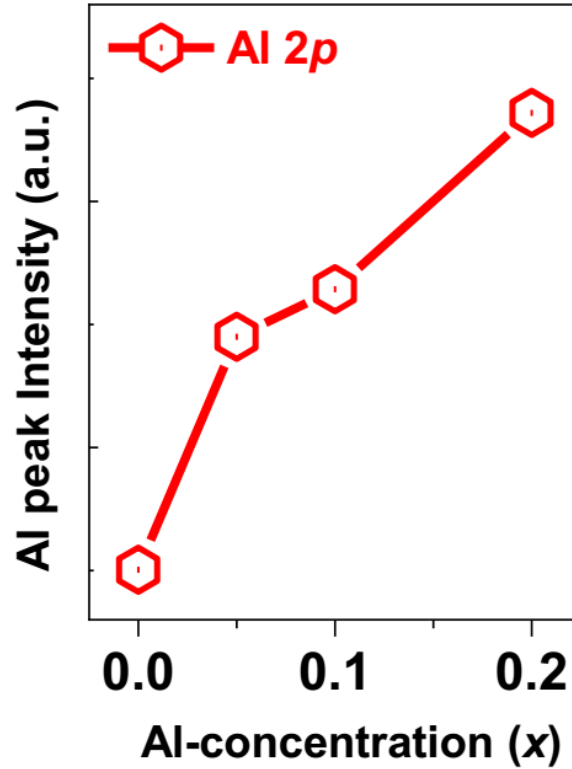


Figure 5.4 The maximum XPS intensity of the Al 2p edges as a function of Al doping content (x).

To verify the chemical composition of the SrMnO₃ ceramics, we performed the field emission scanning electron microscope (FE-SEM) and energy-dispersive spectroscopy (EDS) analyses of pure and Al-doped ($x = 0.01, 0.10, 0.20$) SrMnO₃ ceramics. Noticeably, there is an obvious difference in back-scattered FE-SEM images [Figure 5.5(a)] of the surface morphology of the Al-doped SrMnO₃ ceramics. The surface morphological results of the Al-doped SrMnO₃ ceramics contain two different grain regions with color contrast (gray and black regions). We mapped out the spatial elemental distribution of the corresponding back-scattered SEM data by monitoring the Mn-K and Al-K edge signals. These two unlike regions with different chemical/elemental compositions exhibit a different color contrast [see Figures 5.5(b)-(c)]. The EDS mapping data at the Mn-K and Al-K edges illustrate that the black spot-regions are Mn-deficient [Figure 5.5(b)] and exceedingly Al-abundant [Figure 5.5(c)] in chemical content.

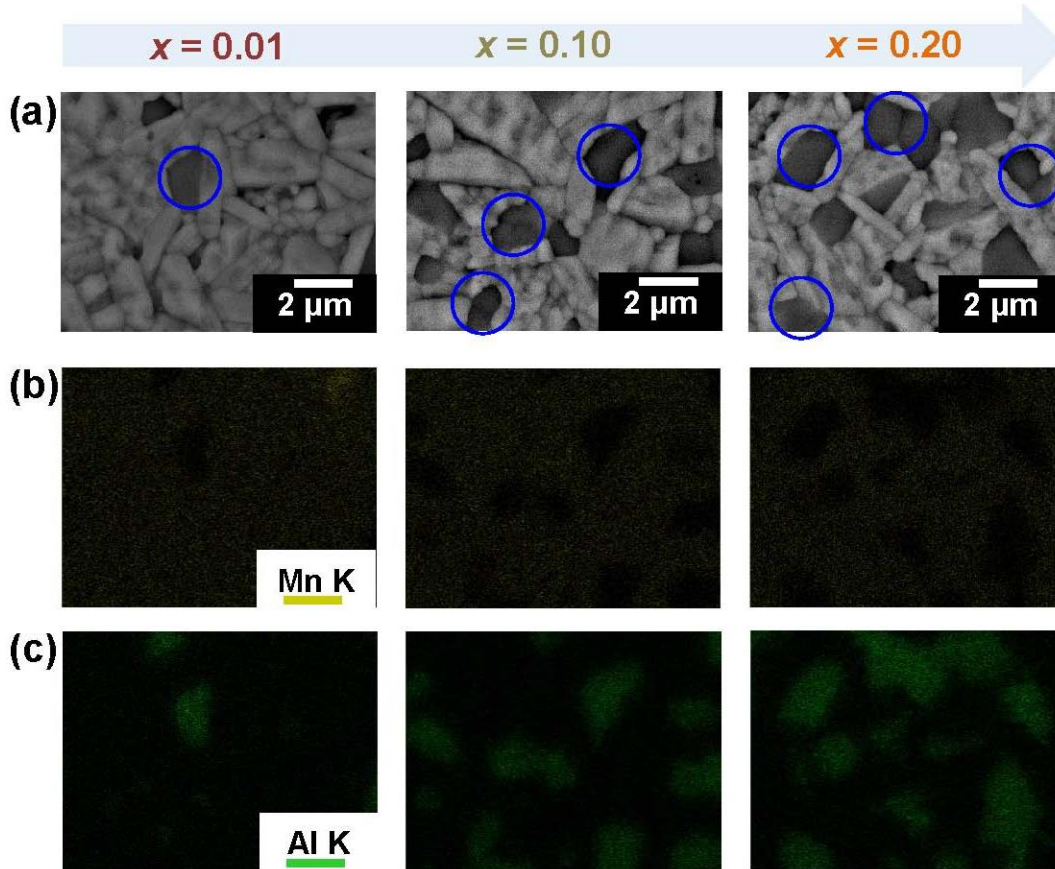


Figure 5.5 (a) Backscattered FE-SEM surface pictures of the Al-doped ($x = 0.01$, 0.10 , and 0.20) SrMnO_3 ceramic pellets. The black spots (SrAl_2O_4 grains) were encircled with blue colors in the back-scattered SEM images. (b) and (d) Elemental mapping results of the Al_2O_3 (1, 10, and 20%) doped SrMnO_3 target surfaces in (a) respectively, using EDS.

5.5 Discussion: Origin of the realized 6H-hexagonal polymorph in our Al-doped SrMnO_3 ceramics

To explain the origin of the realization of 6H polymorph in our Al-doped SrMnO_3 ceramics, we measured the room-temperature Raman spectroscopy of the pure and Al-doped SrMnO_3 samples as shown in Figure 5.6. The four obtained Raman modes of the pure SrMnO_3 are well-matched with the reference Raman pattern (green lines) of 4H SrMnO_3 in Figure 5.6 [26,27].

However, in the Al-doped 4H SrMnO₃ ceramics, additional vibrational modes were noticed at an increasing Al-doping level. Among these modes, the SrAl₂O₄ (marked by black arrow) vibrational mode is identified at 460 cm⁻¹ (an overlapped peak with 4H SrMnO₃ peak at 440) [28]. To identify the additional three modes, we used the Raman spectra of the 6H BaTiO₃ (space group: *P6₃/mmc*) ceramics for comparison due to the unavailable Raman study of the 6H SrMnO₃ [29-31]. Considering the fact that if a Ti atom in the BaTiO₃ is replaced by the Mn atom, the active modes at the wavenumber 380, 596, and 778 cm⁻¹ (in our data) are comparable to 411 [E_{1g}: Mn displacement), 636 [A_{1g}: octahedral stretching), and 806 (A_{1g}: octahedral breathing) modes of the 6H BaTiO₃, respectively [29,30].

To understand explicitly, the frequency of E_{1g} and A_{1g} modes is defined as

$$f = \frac{1}{2\pi} \sqrt{\frac{k}{m}} \quad (5)$$

Where, m represents the atomic weight of a B-site cation [(Mn) in SrMnO₃ or (Ti) in BaTiO₃] atom and k signify a force constant. The relationship between wavenumber and frequency of an oscillator is

$$k = \frac{2\pi}{\lambda} = \frac{2\pi f}{v} \quad (6)$$

Here, λ and v represents the wavelength and wave velocity, respectively.

As E_{1g} (Mn displacement), A_{1g} (octahedral stretching), and A_{1g} (octahedral breathing) modes are associated with the B-site vibration. Therefore, we consider the ratio between the frequency (f) of vibration of Ti ion (for 6H BaTiO₃) and that of Mn ion (for 6H SrMnO₃) via the following equation

$$\frac{f_{Ti}}{f_{Mn}} = \sqrt{\frac{m_{Mn}}{m_{Ti}}} \quad (7)$$

The ratio of the wavenumber of two vibrations can be estimated by substituting the atomic masses of Mn [54.94 (u)] and Ti [47.87 (u)] using the above equation

$$\frac{k_{Ti}}{k_{Mn}} = \frac{f_{Ti}}{f_{Mn}} = \sqrt{\frac{m_{Mn}}{m_{Ti}}} = 1.07$$

The value estimated from the ratio 380 [our Raman data] to the 411 (E_{1g}) [reference 6H BaTiO₃] is

$$\frac{k_{Ti}}{k_{Mn}} = \frac{411}{380} = 1.08$$

Also, the ratio of the vibrational modes at the wavenumber 596 cm⁻¹ [our Raman data] to the vibration mode at 636 cm⁻¹ (A_{1g}) [reference 6H BaTiO₃] is

$$\frac{k_{Ti}}{k_{Mn}} = \frac{636}{596} = 1.06$$

Similarly, taking the ratio of the modes at the wavenumber 778 cm⁻¹ [our Raman data] and 805 cm⁻¹ (A_{1g}) [reference 6H BaTiO₃] is

$$\frac{k_{Ti}}{k_{Mn}} = \frac{805}{778} = 1.03$$

The value calculated from the ratio of atomic mass is quite close to the values estimated from the wavenumber of modes in our experimental data. It is highly likely that the vibration peaks around 380, 596, and 778 cm⁻¹ are the E_{1g} (Mn displacement), A_{1g} (octahedral stretching), and A_{1g} (octahedral breathing) modes of the 6H SrMnO₃ polymorph.

It is highly likely that additional vibrational (380, 596, and 778 cm⁻¹) modes are the activated Raman modes of the 6H-SrMnO₃. However, the intensity of these modes is comparatively low, further studies are required to understand these modes. Additionally, we could not obtain a vibrational peak to replace the mode (E_{1g} : 221 cm⁻¹) in the 6H-BaTiO₃ due to the limitation of our measurement setup (Raman data cannot be obtained below the 200 cm⁻¹).

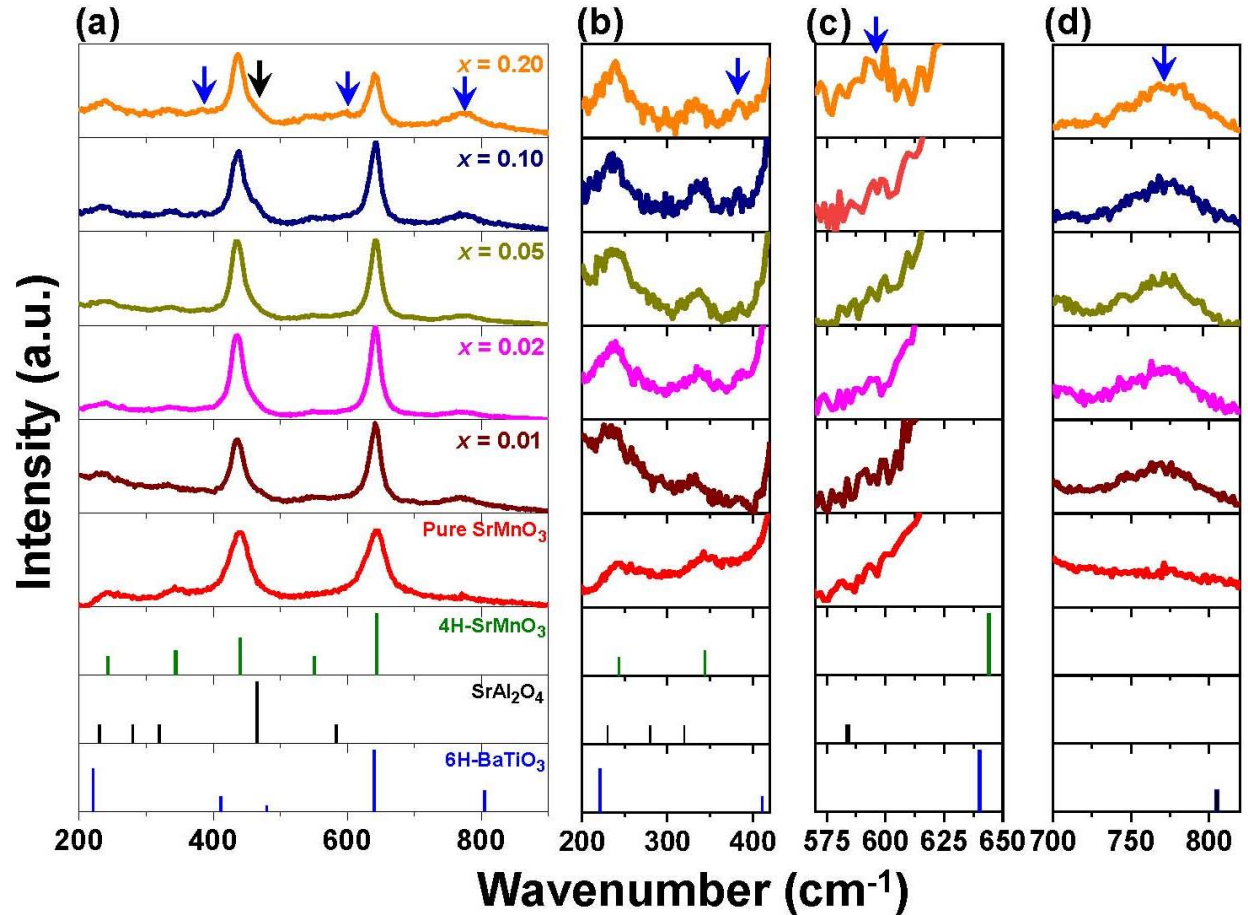


Figure 5.6 (a) Room-temperature Raman spectroscopy of a pure and Al-doped SrMnO_3 ceramics with various doping concentrations (x) in the wavenumber range from 200 to 900 cm^{-1} . The reference Raman spectral peaks of the 4H SrMnO_3 (green lines), SrAl_2O_4 (blue lines), and 6H BaTiO_3 (black lines) are also plotted. The enlarged Raman peaks are provided in the wavenumber range from (b) 300 to 420 cm^{-1} , 570 to 650 cm^{-1} , and (c) 700 to 820 cm^{-1} [28,29].

To verify our experimental results for the vacancy defects in SrMnO_3 ceramics, first-principles density functional theory (DFT) calculations were applied to compare the energies of both (4H and 6H) SrMnO_3 polymorphs and the vacancy defect (Sr-deficiency and oxygen vacancies) in each corresponding polymorph, as tabulated in Table 5.2 [32-35]. In order to have

an equal number of atoms and homogeneous deficiencies, $3 \times 2 \times 1$ and $2 \times 2 \times 1$ supercells were considered for the 4H and 6H SrMnO_3 polymorphs, respectively [Appendex A]. It was revealed that the 4H polymorph of the SrMnO_3 is energetically more favorable by 2.5 meV/atom than that of the 6H SrMnO_3 . Furthermore, independent of the concentration, the Sr-deficiency, and the oxygen vacancy did not affect this energy difference. The energy difference between the two (4H and 6H) SrMnO_3 polymorphs is negligible, therefore, we concluded that the vacancy defect (Sr-deficiency and oxygen vacancy) has no role to realize the 6H polymorph in the 4H SrMnO_3 .

Table 5.2 Total energy calculation of the 4H SrMnO_3 , 6H SrMnO_3 , and vacancy defects (strontium (Sr) and oxygen (O) vacancy) in each corresponding SrMnO_3 polymorph.

Strontium (Sr) Deficiency (%)	4H-hexagonal SrMnO_3 Energy (eV)/atom	6H-hexagonal SrMnO_3 Energy (eV)/ atom
0	-7.2251	-7.2003
4.16	-7.2206	-7.1983
8.33	-7.2233	-7.1963
12.48	-7.2221	-7.1918
16.66	-7.2127	-7.1983
<hr/>		
Oxygen (O) Vacancies (%)	4H-hexagonal SrMnO_3 Energy (eV)/atom	6H-hexagonal SrMnO_3 Energy (eV)/ atom
0	-7.2257	-7.2012
1.39	-7.2203	-7.1994
2.78	-7.2164	-7.1973
4.16	-7.2131	-7.1917
5.55	-7.2068	-7.1862
11.11	-7.1770	-7.1557

Herein, based on the experimental and theoretical calculations, it is important to discuss how a 6H SrMnO_3 polymorph is realized in the SrMnO_3 via Al-doping. The realization of the 6H

SrMnO₃ polymorph is dependent on the interfacial strain mechanism revealed in the refined XRD results. From the XRD data of the Al-doped SrMnO₃ ceramics (Fig. 4), a 6H polymorph is predominant at higher Al-doping content ($x \geq 0.10$). Likewise, the number of SrAl₂O₄ grains increased at a higher doping level x ($x \geq 0.10$). It is highly likely that the Al doping would enable the 4H polymorph in pure SrMnO₃ to be pressurized by the stress (~6 GPa) arising from the mismatch of the lattice parameters amongst the 4H SrMnO₃ polymorph and the SrAl₂O₄ at the grain boundary.

On the other side, we confirmed via first-principle calculations that the total energy in the existence of vacancy defects for both the SrMnO₃ (4H and 6H) polymorphs are identical and have no effect in the realization of the 6H SrMnO₃ polymorph. Therefore, we finally realized a 6H polymorph in the Al-doped SrMnO₃ ceramics by the interfacial strain between 4H SrMnO₃ and SrAl₂O₄.

5.6 Further interest

In the strongly correlated complex oxides, the realization of room temperature multi-ferroelectricity (e.g two ferroic orders ferromagnetic and ferroelectric) has been an important point in recent decades due to the practical applications as well as ionic physics involved. To achieve the multiferroic SrMnO₃, we use the interfacial strain to attain a polar phase in the centrosymmetric 6H-hexagonal SrMnO₃ by tilting the MnO₆ octahedra. However, we succeeded only to realize the 6H SrMnO₃ ceramics without ferroelectric ordering. Further experiments need to be performed for the identification of the polar phase, especially growing the 6H SrMnO₃ thin film epitaxially.

References

- [1] R. Søndena, P. Ravindran, S. Stølen, T. Grande, and M. Hanfland, *Phys. Rev. B* **74**, 144102 (2006).
- [2] R. Søndena, S. Stølen, P. Ravindran, and T. Grande, *Phys. Rev. B* **75**, 214307 (2007).
- [3] A. A. Belik, Y. Matsushita, Y. Katsuya, M. Tanaka, T. Kolodiazhnyi, M. Isobe, and E. T. Muromachi, *Phys. Rev. B* **84**, 094438 (2011).
- [4] K. Kikuchi, H. Chiba, M. Kikuchi, and Y. Syono, *J. Solid State Chem.* **146**, 1 (1999).
- [5] O. Chmaissem, B. Dabrowski, S. Kolesnik, J. Mais, D. E. Brown, R. Kruk, P. Prior, B. Pyles, and J. D. Jorgensen, *Phys. Rev. B* **64**, 134412 (2001).
- [6] B. L. Chamberland, A. W. Sleight, and J. F. Weiher, *J. Solid State Chem.* **1**, 506 (1970).
- [7] P. D. Battle, T. C. Gibb, and C. W. Jones, *J. Solid State Chem.* **74**, 60 (1988).
- [8] H. Shibahara, *J. Mater. Res.* **6**, 565 (1991).
- [9] Y. Syono, S. I. Akimoto, and K. Kohn, *J. Phys. Soc. Jpn.* **26**, 993 (1969).
- [10] T. Negas and R. S. Roth, *J. Solid State Chem.* **1**, 409 (1970).
- [11] J. W. Guo, P. S. Wang, Y. Yuan, Q. He, J. L. Lu, T. Z. Chen, S. Z. Yang, Y. J. Wang, R. Erni, M. D. Rossell, V. Gopalan, H. J. Xiang, Y. Tokura, and P. Yu, *Phys. Rev. B* **97**, 235135 (2018).
- [12] S. Kamba, V. Goian, V. Skoromets, J. Hejtmánek, V. Bovtun, M. Kempa, F. Borodavka, P. Vaněk, A. A. Belik, J. H. Lee, O. Pacherová, and K. M. Rabe, *Phys. Rev. B* **89**, 064308 (2014).
- [13] C. Becher, L. Maurel, U. Aschauer, M. Lilienblum, C. Mag'e, D. Meier, E. Langenberg, M. Trassin, J. Blasco, I. P. Krug, P. A. Algarabel, N. A. Spaldin, J. A. Pardo, and M. Fiebig, *Nat. Nanotechnol.* **10**, 661 (2015).
- [14] L. Vistoli, W. Wang, A. Sander, Q. Zhu, B. Casals, R. Cichelero, A. Barthelemy, S. Fusil, G. Herranz, R. Abrudan, E. Weschke, K. Nakazawa, H. Kohno, J. Santamaria, W. Wu, V. Garcia,

and M. Bibes, *Nat. Phys.* **15**, 67 (2019).

[15] M. B. Nielsen, D. Ceresoli, P. Parisiades, V. B. Prakapenka, T. Yu, Y. Wang, and M. Bremholm, *Phys. Rev. B* **90**, 214101 (2014).

[16] G. Y. Shen, V. B. Prakapenka, P. J. Eng, M. L. Rivers, and S. R. Sutton, *J. Synchrotron Rad.* **12**, 642 (2005).

[17] Y. B. Wang, M. Rivers, S. Sutton, N. Nishiyama, T. Uchida, and T. Sanehira, *Phys. Earth Planet In.* **174**, 270 (2009).

[18] M. Avdeev, S. Yakovlev, A. A. Yaremchenko, and V. V. Kharton, *J. Solid State Chem.* **180**, 3535 (2007).

[19] J. M. Perez-Mato, R. L. Withers, A. K. Larsson, D. Orobengoa, and Y. Liu, *Phys. Rev. B* **79**, 064111 (2009).

[20] B. B. V. Aken, T. T. M. Palstra, A. Filippetti, and N. A. Spaldin *Nat. Mater.* **3**, 164 (2004).

[21] J.-H. Lee, P. Murugavel, H. Ryu, D. Lee, J. Y. Jo, J. W. Kim, H. J. Kim, K. H. Kim, Y. Jo, M.-H. Jung, Y. H. Oh, Y. -W. Kim, J. -G. Yoon, J. -S. Chung, and T. W. Noh, *Adv. Mater.* **18**, 3125 (2006).

[22] L. B. McCusker, R. B. Von Dreele, D. E. Cox, D. Louër, and P. Scardi, *J. Appl. Cryst.* **32**, 36 (1999).

[23] J. Rodriguez-Carvajal, FULLPROF a Rietveld and pattern matching analysis program, Laboratoire Leon Brillouin (CEA–CRNS), Paris France (2007).

[24] J. F. Watts, and J. Wolstenholme, *An Introduction to Surface Analysis by XPS and AES*, John Wiley & Sons, 2003.

[25] J. Y. Baek, L. T. Duy, S. Y. Lee, and H. Seo, *J. Mater. Sci. Technol.* **42**, 28 (2020).

- [26] A. Sacchetti, M. Baldini, F. Crispoldi, P. Postorino, P. Dore, A. Nucara, C. Martin, and A. Maignan, *Phys. Rev. B* **72**, 172407 (2005).
- [27] A. Sacchetti, M. Baldini, P. Postorino, C. Martin, and A. Maignan, *J. Raman Spectrosc.* **37**, 591 (2006).
- [28] R. E Rojas-Hernandez, W. More, F. Rubio-Marcos, and J. F. Fernandez, *J Raman Spectrosc.* **50**, 91 (2019).
- [29] N. G. Eror, T. M. Loehr, and B. C. Cornilsen, *Ferroelectrics* **28**, 321 (1980).
- [30] H. Yamaguchi, H. Uwe, T. Sakudo, and E. Sawaguchi, *Phys. Soc. Jpn.* **56**, 589 (1987).
- [31] H. M. Nguyen, N. V. Dang, P. Y. Chuang, T. D. Thanh, C. W. Hu, T. Y. Chen, V. D. Lam, C. H. Lee, and L. V. Hong, *Appl. Phys. Lett.* **99**, 202501 (2011).
- [32] G. Kresse and J. Furthmüller, *Phys. Rev. B* **54**, 11169 (1996).
- [33] J. P. Perdew, K. Burke, and M. Ernzerhof, *Phys. Rev. Lett.* **77**, 3865 (1996).
- [34] P. E. Blochl, *Phys. Rev. B* **50**, 17953 (1994).

Chapter 6

Fabrication of freestanding single-crystalline perovskite films

6.1 Importance of freestanding films

In complex oxides, strain engineering comes from the lattice-mismatch of a single-crystalline thin film and the substrate is provided to control the structural and functional properties in the material [1-3], however, it cannot produce large and continuously variable strain states [3,4]. The initiation of freestanding complex oxide membranes have got enormous attention these days due to their tunability, potential integration with the flexible substrate, enticing opportunities to address the challenges due to substrate growth, and develop additional degrees of freedom to manipulate material properties [1-7].

6.2 Inversion symmetry breaking by mechanical stress

In this study, our focus is to break the inversion symmetry of the single-crystalline perovskite SrRuO_3 (SRO) membrane via external stimuli (i.e., stretching or bending via mechanical force), explore, and understand the unknown functional properties which are not achievable by direct epitaxial growth (variable strain states). To manipulate the inversion symmetry of the SrRuO_3 oxides via tensile strain, we need to transfer the high-quality freestanding SrRuO_3 membrane to the stretchable polymer substrate [4,5,8]. The strain of the SrRuO_3 membrane can be controlled by applying external tensile forces [4,5,8]. The external force will be applied on the four sides of the polymer layer by stretching the micromanipulators uniformly [4,5]. Moreover, bend the membrane is another possible way to manipulate the inversion symmetry in

the SRO membrane. To bend the SRO membrane the scanning probe microscope (SPM) can be used to apply the strain gradient [9,10].

6.3 Strategy

Many techniques have been used to transfer the oxides membranes, involving the ion implantations, dissolving the NaCl substrate using water, chemical wet-etching of a sacrificial layer using different acids. However, these techniques are challenging to be generalized for a broad range of perovskites. In recent years, Lu et al., presented a synthetic route for a successful transfer of the perovskite film using hygroscopic oxide $\text{Sr}_3\text{Al}_2\text{O}_6$ (SAO) as a sacrificial layer, which has got numerous attention and utilizes for different perovskite oxides free-standing films [7].

To achieve a high-quality SrRuO_3 (SRO) free-standing perovskite membrane, we introduce the SrCuO_2 (SCO) perovskite oxide as a sacrificial layer. The SrCuO_2 is an oxygen-deficient perovskite which makes it very sensitive to the humidity [11]. Also, the in-plane lattice constant of the SrCuO_2 ($a_{\text{SCO}} = 3.94 \text{ \AA}$) is nearly identical to the SrTiO_3 ($a_{\text{STO}} = 3.905 \text{ \AA}$) substrate with the 0.6% [12,13]. The structural similarity between the SCO and STO substrate allows the epitaxial growth of both SCO and the SRO/SCO heterostructure on the STO substrate. After the successful growth, subsequently, we begin to perform the etching and transfer by attaching the polymer (Polydimethylsiloxane; PDMS) as a mechanical support and dipping the SRO/SCO/STO heterostructure into an aqueous (diluted-acidic potassium iodide) solution [KI (8 mg) + HCl (10 ml) + H_2O (100 ml)] [14,15]. Once the dissolution process completes the SrRuO_3 film is transferred to another [quartz or Pt(111)/ TiO_2 / SiO_2 /Si(100) or polymer] secondary substrate for further measurements.

6.4 Experimental methods

(1) Synthesis of SrCuO₂ (SCO) ceramic targets.

The SrCuO₂ ceramic target was synthesized by the solid-state-reaction method. We purchased the powders, SrCO₃ (99.9%) and CuO (99.9%) from Sigma-Aldrich and High Purity Chemicals, respectively. first of all, rough weighing of the powders (i.e., SrCO₃ and CuO) was performed and then dried at 100 °C to remove the moisture. Next, the powders were weighed at an exact mole ratio of 1:1 for chemical reaction, respectively. The weighed powders were put in the bottles, mixed with the yttria-zirconia (1:2) and the ethanol balls (1:3) of the powders, then ball-milled at 140 rpm for 24 h. After, the ball-milling process, the powders were put in the oven and dried at 100 °C for 24 h. Thereafter, we transfer the dried powders to aluminum-crucibles and start calcination from room temperature to 600 °C with the increasing rate of 5 °C/min, remains constant for 4 h at 600 °C, and then reduced temperature down to room temperature with the decreasing rate of 5 °C/min. The obtain calcined powders were again ball-milled at the same speed 140 rpm for the next 24 h, dried in an oven at 100 °C, and then ground. Subsequently, we pelletized the resulted dried powders to a diameter of 1 inch at a pressure of 19.34 MPa. Sintering of the SrCuO₂ target was completed at 900 °C in an alumina boat (capped with the alumina plate) for 24 h with an increasing/decreasing temperature of 5 °C/min. The whole synthesis process is schematized in Figure 6.1.

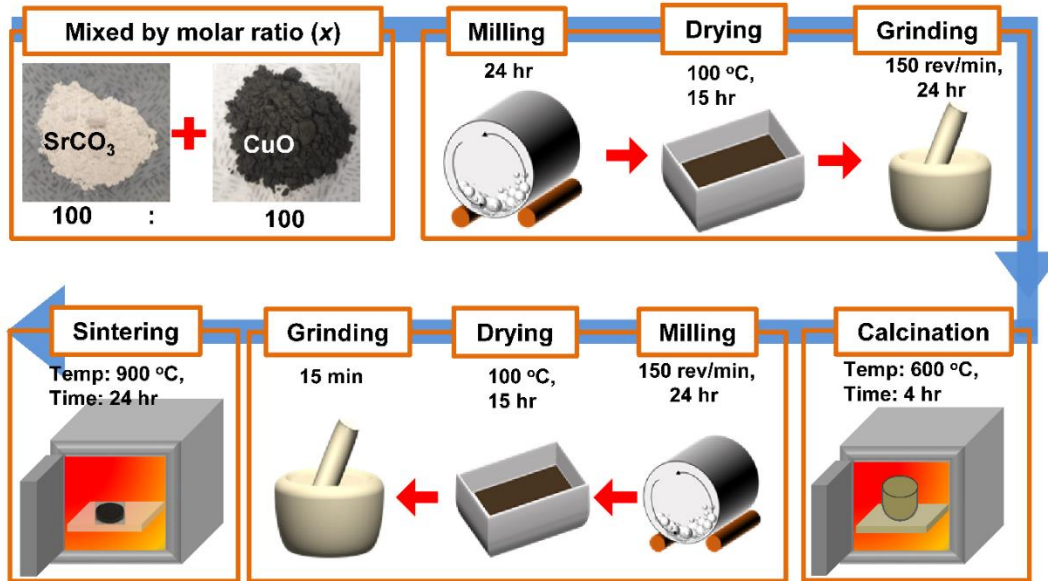


Figure 6.1 Synthesis process of a SrCuO_2 target using a traditional solid-state-reaction technique.

(2) The preparation of the freestanding complex oxide membranes

The preparation of the freestanding complex oxide membranes consists of the growth, solution preparation, transfer process. To obtain the free-standing epitaxial oxide films, we first achieved the optimum growth conditions for the SrRuO_3 film on the SrTiO_3 (001) substrate via pulsed-laser-deposition (PLD). An epitaxial SrRuO_3 film with well crystalline quality is grown, can be seen in the x-ray diffraction (XRD) analyses and atomic force microscopy (AFM) images (Figure 6.2). Then, to exfoliate a free-standing SrRuO_3 film, $\text{SrRuO}_3/\text{SrCuO}_2/\text{SrTiO}_3$ (001) heterostructures were grown via PLD. The SrCuO_2 film, used as a sacrificial buffer layer for the succeeding release of an epitaxial SrRuO_3 film layer from the SrTiO_3 (001) substrate. Before film deposition on the STO (001) substrate, the mounted ceramic target was pre-ablated at a laser energy density of 1.05 J/cm^2 and the laser (pulses) frequency of 5 Hz for 10 min. The heater temperature (for deposition) was fixed at $620 \text{ }^\circ\text{C}$ in an oxygen partial pressure of 100 mTorr at a laser fluence of 1.05 J cm^{-2} and a laser frequency rate of 1 Hz. The SrRuO_3 film grew from a

SrRuO₃ target (ceramic) at a fixed heater temperature of 580 °C in the same oxygen partial pressure (used for the SrCuO₂) of 100 mTorr, a laser repetitive frequency 3 Hz, and laser (energy density) fluence of 1.05 J cm⁻². Following growth, the heterostructures were cooled down to room temperature (RT) at a decreasing rate of 10 °C min.⁻¹ in a 1 atmospheric pressure (1 atm ~760 Torr).

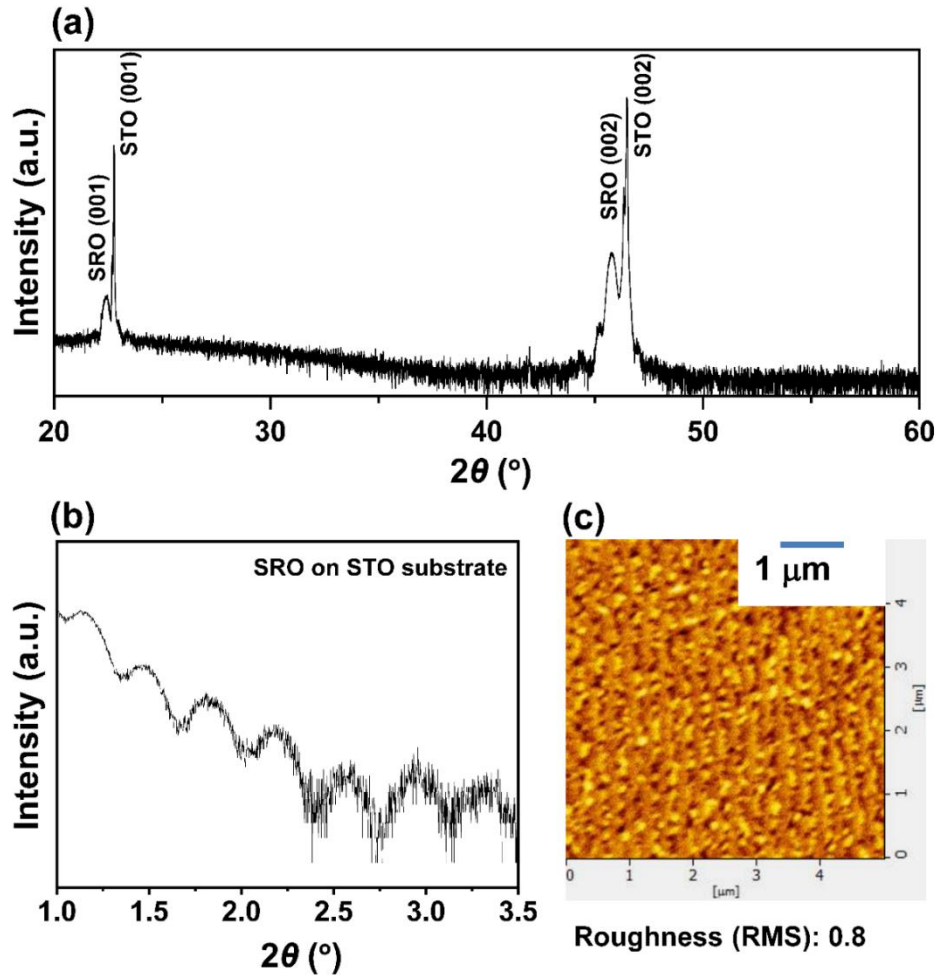


Figure 6.2 (a) The x-ray diffraction (XRD) analysis of the epitaxially grown SrRuO₃ (SRO) film on the SrTiO₃ (001) substrate. (b) The thickness (23.3 nm) of the SRO film is estimated by the x-ray Reflectometry (XRR) analysis. (c) Surface topography of the as-synthesized epitaxial SRO film.

(3) Transfer of the epitaxial SrRuO₃ perovskite film

After the successful epitaxial film growth, the SrRuO₃ film was freed from the STO (001) substrate using selective chemical etching of a sacrificial SrCuO₂ (SCO) layer. To perform the etching process of an SCO layer, the SrRuO₃/SrCuO₂/SrTiO₃ heterostructure is placed in the aqueous (diluted potassium iodide) solution of HCl (10 ml) + KI (8 mg) + H₂O (100 ml) [10,11] [Figure 6.3]; this solution dissolves the SCO with a high etch rate while having a negligible effect on the SrRuO₃ films [10,11]. After the complete etching of the SCO film layer, the released SrRuO₃ epitaxial film was transferred to another secondary substrate (i.e., quartz or Pt(111)/TiO₂/SiO₂/Si(100)) via polydimethylsiloxane (PDMS) polymer support [Figure 6.3]. The transfer films were then used for the structural, surface, and electrical measurements.

6.5 Results

The x-ray diffraction (XRD) theta-2theta (θ - 2θ) examinations of the SrRuO₃/SrCuO₂/SrTiO₃ heterostructure and the transferred SrRuO₃ membrane on Pt(111)/TiO₂/SiO₂/Si(100) were measured [Figure 6.3]. The SCO diffraction peak (before etching) identified in the XRD pattern [Figure 6.3 (a)] is completely dissolved in the aqueous KI solution and has no identification peak in the transferred SRO membrane [Figure 6.3 (c)]. The diffraction peak of the SrRuO₃ before and after the transfer are identical [Figure 6.3].

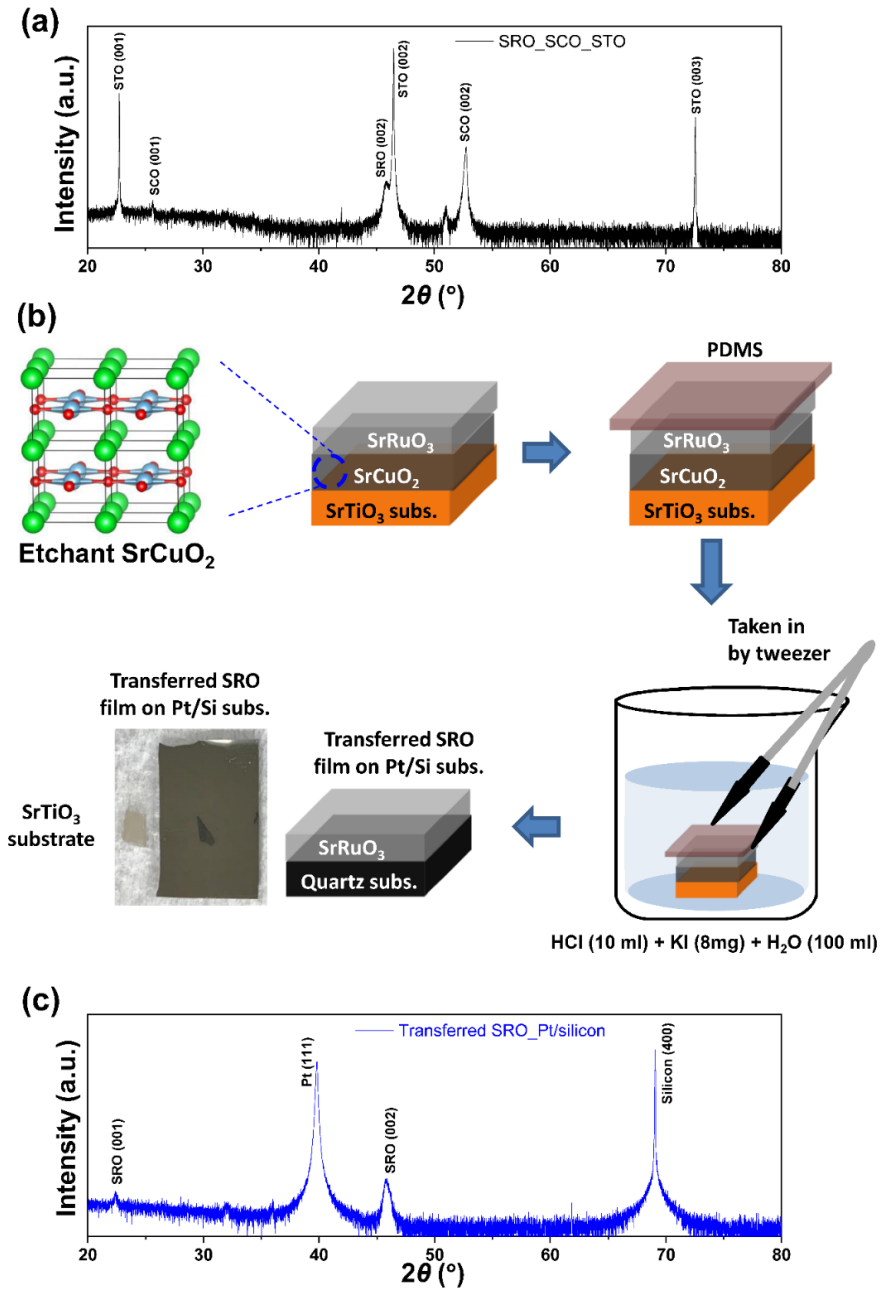


Figure 6.3 (a) The x-ray diffraction (XRD) results of an epitaxially grown SrRuO₃ (SRO)/SrCuO₂ (SCO) on the SrTiO₃ (001) substrate. (b) The etching of the SrCuO₂ film layer and transfer of the SrRuO₃ film. (c) The XRD of the as-transferred film on a secondary Pt(111)/TiO₂/SiO₂/Si(100) substrate. A clear (001) and (002) diffraction of the transferred SRO film can be seen in Figure 6.3(c).

6.6 Discussion

In this work, we have synthesized the good-quality SrRuO₃/SrCuO₂ on the SrTiO₃ (001) substrate and successfully transfer the free-standing SrRuO₃ membrane to another substrate by dissolving the sacrificial layer of the SrCuO₂. The crystalline quality of the SrRuO₃ film is confirmed by the XRD data. At this of the project, we are performing other chemical and electrical measurements to study the elemental analysis and electrical conductivity of the perovskite SrRuO₃ epitaxial film in the as-grown state (before transfer) and after transfer membranes.

6.7 Potential applications

The high-quality free-standing membranes without thickness limitation and flexibility nature (under extreme strain and bending) have exotic potential applications. The inversion symmetry breaks in the free-standing oxide membranes under the high strain gradient via bending leads towards the flexoelectric and flexomagnetic research. Moreover, with bending and stretching the electronic ground state could break the inversion symmetry in centrosymmetric (insulators and conductor) oxides to realize exotic properties such as superconductivity.

References

- [1] J. H. Haeni, P. Irvin, W. Chang, R. Uecker, P. Reiche, Y. L. Li, S. Choudhury, W. Tian, M. E. Hawley, B. Craigo, A. K. Tagantsev, X. Q. Pan, S. K. Streiffer, L. Q. Chen, S. W. Kirchoefer, J. Levy, and D. G. Schlom, *Nature* **430**, 758 (2004).
- [2] Y. L. Li, S. Choudhury, J. H. Haeni, M. D. Biegalski, A. Vasudevarao, A. Sharan, H. Z. Ma, J. Levy, V. Gopalan, S. T.-McKinstry, D. G. Schlom, Q. X. Jia, and L. Q. Chen, *Phys. Rev. B* **73**, 184112 (2006).
- [3] A. Vasudevarao, A. Kumar, L. Tian, J. H. Haeni, Y. L. Li, C.-J. Eklund, Q. X. Jia, R. Uecker, P. Reiche, K. M. Rabe, L. Q. Chen, D. G. Schlom, and V. Gopalan, *Phys. Rev. Lett.* **97**, 257602 (2006).
- [4] S. S. Hong, M. Gu, M. Verma, V. Harbola, B. Y. Wang, D. Lu, A. Vailionis, Y. Hikita, R. Pentcheva, J. M. Rondinelli, and H. Y. Hwang, *Science* **368**, 71 (2020).
- [5] R. Xu, J. Huang, E. S. Barnard, S. S. Hong, P. Singh, E. K. Wong, T. Jansen, V. Harbola, J. Xiao, B. Y. Wang, S. Crossley, D. Lu, S. Liu, and H. Y. Hwang *Nat. Commun.* **11**, 3141 (2020).
- [6] D. Pesquera, E. Parsonnet, A. Qualls, R. Xu, A. J. Gubser, J. Kim, Y. Jiang, G. Velarde, Y.-L. Huang, H. Y. Hwang, R. Ramesh, and L. W. Martin *Adv. Mater.* 2003780, (2020).
- [7] D. Lu, D. J. Baek, S. S. Hong, L. F. Kourkoutis, Y. Hikita, and H. Y. Hwang, *Nat. Mater.* **15**, 1255 (2016).
- [8] L. Han, Y. Fang, Y. Zhao, Y. Zang, Z. Gu, Y. Nie, and X. Pan, *Adv. Mater. Interfaces* 1901604 (2020).
- [9] D. Lee, *APL Mater.* **8**, 090901 (2020).
- [10] S. Das, B. Wang, T. R. Paudel, S. M. Park, E. Y. Tsymbal, L. Q. Chen, D. Lee, and T. W. Noh, *Nat. Commun.* **10**, 537 (2019).

- [11] M.A. Augustyniak-Jablokow, Y. V. Tablokov, T. A. Ivanova, I. J. Onyszkiewicz, and V. A. Shustov, *Acta Phys. Pol. A* **108**, 345 (2005).
- [12] D. Samal, T. Haiyan, H. Molegraaf, B. Kuiper, W. Siemons, S. Bals, J. Verbeeck, G. V. Tendeloo, Y. Takamura, E. Arenholz, C. A. Jenkins, G. Rijnders, and G. Koster, *Phys. Rev. Lett.* **111**, 096102 (2013).
- [13] B. Kuiper, D. Samal, D. H. A. Blank, J. E. t. Elshof, G. Rijnders, and G. Koster, *APL Mater.* **1**, 042113 (2013).
- [14] S. R. Bakaul, C. R. Serrao, O. Lee, Z. Lu, A. Yadav, C. Carraro, R. Maboudian, R. Ramesh, and S. Salahuddin, *Adv. Mater.* **29**, 1605699 (2017).
- [15] H. Elangovan, M. Barzilay, S. Seremi, N. Cohen, and Y. Jiang, L. W. Martin, and Y. Ivry, *ACS Nano* **14**, 5053 (2020).

Chapter 7

Summary

Spatial inversion symmetry, defined as $a = -a$, where a is a position of a point in a crystal symmetry from the center of the crystal symmetry. The spatial inversion symmetry of the complex oxides greatly holds the functional properties of the materials. When the spatial inversion symmetry of the complex oxides break it generates a polar displacement between the cations and anions of material, resulting in an enhancement in the functional properties (i.e., ferroelectric, piezoelectric, multi-ferroic, and flexoelectric) in complex oxides. Thus, controlling the spatial inversion symmetry in complex oxides can lead us to achieve the required functional properties in a material. In this research work, we enhanced the functional properties in complex oxides by controlling the spatial inversion symmetry using various experimental methods like anion substitution and stress/strain engineering at the grain boundaries.

In this work, substituting the sulfur atom at the apical oxygen site, we enhanced the ferroelectric polarization in perovskite oxysulfides with controlled spatial-inversion symmetry. By manipulating the sulfur concentration (x), we systematically examine the structural and physical properties of sulfur-doped $\text{Pb}(\text{Zr,Ti})\text{O}_{3-x}\text{S}_x$ films. An enhancement in the tetragonality and ferroelectricity by sulfurization is observed with the band-gap reduction, which is consistent with our theoretical predictions. In the sulfurized films, the ferroelectric phonon modes become softened progressively, probably due to the substitution of apical oxygens with sulfur atoms. The sulfur (S) makes a strong covalent bond with the titanium (Ti) element (Ti 3d-S 3p) compared with the Ti 3d-O 2p bonding due to the lower electronegativity of the sulfur element than the oxygen atom. The strong covalency of the Ti-S (apical) bonding lifted the spatial inversion symmetry uniformly in PZT oxysulfide.

To achieve the high piezoelectric response in the BNT-based ceramics at a low applied electric field with spatial inversion symmetry control, we add the ferroelectric BNKT seeds (at different volume concentrations) to the relaxor BNT-ST ceramics using the solid-state reaction method. At a given applied electric field in BNT-28ST/BNKT composite, the polarization and strain loops indicated that ferroelectric plate-type BNKT particles promote a transition from relaxor to ferroelectric phase accompanied by significant decrease in the poling field. The successive reduction in the relaxor/ferroelectric phase transition field highly suggests the analysis of electrostrain at low driving field. Thus, at the grain boundary of the relaxor BNT-28ST and ferroelectric BNKT, the non-centrosymmetric BNKT particle stressed the centrosymmetric BNT-28ST to its manipulate the inversion symmetry, resulting in a high piezoelectric response upon the structural transition from the pseudocubic BNT-28ST to tetragonal.

The realization of the ferroelectric polarization in the hexagonal complex (like YMnO_3) oxide material is of great interest, comes from the tilting of the MnO_5 trigonal bipyramid rather than the off-centering displacement in perovskites. In this work, we plan to produce the ferroelectric polarization in the 6H-hexagonal ($P6_3/mmc$) SrMnO_3 ceramics with controlled inversion symmetry in the Aluminum (Al) doped SrMnO_3 . By doping the Al to the SrMnO_3 ceramic uniformly, we constructed the hexagonal SrAl_2O_4 grains locally in the proximity to the 4H-hexagonal SrMnO_3 grains. Al-doping would enable the 4H-hexagonal ($P6_3/mmc$) phase in pure SrMnO_3 to be pressurized by the stress (~ 6 GPa) arising from the lattice mismatch between the 4H SrMnO_3 polymorph and the isosymmetric SrAl_2O_4 ($P6_322$) at the grain boundary. Using the interfacial strain mechanism, a 6H-hexagonal polymorph is realized in the SrMnO_3 polymorph identified in the x-ray diffraction and Raman spectroscopy measurements. We plan to generate the

ferroelectric ordering by octahedral tilting in a 6H-hexagonal SrMnO_3 oxide. Then, the inversion symmetry in 6H-hexagonal SrMnO_3 is expected to be broken and generate a new polar symmetry.

In this study, we demonstrated the high-quality SrRuO_3 thin film on the $\text{SrCuO}_2/\text{SrTiO}_3$ (001) substrate. The epitaxial SRO film layer was then released by dissolving the SrCuO_2 sacrificial layer using the aqueous solution [KI (8 mg) + HCl (10 ml) + H_2O (100 ml)] and finally transferred to another substrate using the mechanical support (PDMS). By comparing the structural, surface, and chemical characterization of the epitaxial SrRuO_3 membrane, before and after the transfer to another substrate, we confirm that the quality of the membrane is preserved by comparing it with the bulk results.

Our results in this thesis provide a better understanding of the enhanced functional properties in complex oxides by controlling their spatial inversion symmetry. We believe that this work can play a crucial role in device applications like non-volatile memories, actuators, and flexible electronics.

Appendix A: Experimental and theoretical methods

A.1 Theoretical calculations

We have performed the first principle study of the pure tetragonal $\text{Pb}(\text{Zr}_{0.5}\text{Ti}_{0.5})\text{O}_3$ and sulfur substituted $\text{Pb}(\text{Zr}_{0.5}\text{Ti}_{0.5})\text{O}_3$ with a uniform distribution of zirconium (Zr) and titanium (Ti). All the calculations were computed using the Vienna *ab initio* Simulation Package (VASP) based on the density functional theory (DFT). The projected augmented wave (PAW), the PBEsol exchange-correlation functional, and a kind of generalized gradient approximation (GGA) were used to optimize the structure of the sulfur substituted $\text{Pb}(\text{Zr}_{0.5}\text{Ti}_{0.5})\text{O}_3$. In these calculations, we used the 800 eV cut-off energy, and the atomic positions were relaxed with the conjugated gradient method until each atom force was smaller than 0.001 eV/Å. The cell volume relaxation was also performed. To examine the effect of sulfur substituted density, we considered one or two sulfur substitutions in $2 \times 2 \times 2$, $2\sqrt{2} \times 2\sqrt{2} \times 2$, $2\sqrt{2} \times 2\sqrt{2} \times 4$, and $4 \times 4 \times 4$ $\text{Pb}(\text{Zr}_{0.5}\text{Ti}_{0.5})\text{O}_3$ supercells. For two sulfur substituted case, the second sulfur site was determined far away from the first sulfur substituted site. The first Brillouin zone was divided by a $4 \times 4 \times 4$ k -mesh for the $2 \times 2 \times 2$ supercell. The k -mesh was properly controlled according to the cell size. The hybrid functional (HSE06) was also used to obtain the more accurate band gap values of the sulfur substituted $\text{Pb}(\text{Zr}_{0.5}\text{Ti}_{0.5})\text{O}_3$ at higher sulfur substitution densities. The Berry phase calculations are used to achieve the spontaneous polarization of the tetragonal $\text{Pb}(\text{Zr}_{0.5}\text{Ti}_{0.5})\text{O}_3$ and sulfur substituted $\text{Pb}(\text{Zr}_{0.5}\text{Ti}_{0.5})\text{O}_3$.

A.2 Ferroelectric $\text{Pb}(\text{Zr}_{0.52}\text{Ti}_{0.48})\text{O}_3$ film fabrication

To fabricate ferroelectric $\text{Pb}(\text{Zr}_{0.52}\text{Ti}_{0.48})\text{O}_3$ (PZT) thin films with high crystallinity, we first prepared a PZT sol-gel solution (with 0.2 mole liter⁻¹) by diluting the pristine PZT (0.4 mole liter⁻¹)

¹) solution in equal volume ratio to the acetic acid/2-methoxyethanol mixture solvent. To grow a pure PZT film, we spin-coated the diluted PZT sol-gel solution on a SrRuO₃ (10 nm)/ SrTiO₃ (001) film [3000 rpm for 30 s], cured the spin-coated PZT solution on a hot plate [450 °C for 7 min], and annealed in a box furnace [650 °C for 3 min]. These three steps of the spin-coating, curing, and thermal-annealing were repeated four times to deposit a PZT film with a thickness of about 170 nm (Fabrication process in chapter 2). For the crystallization, we finally annealed the as-deposited PZT film at 650 °C for in box-furnace for 30 min.

A.3 Transmission electron microscopy measurements and analyses

The crystallinities of pure and sulfurized PZT films grown on SrRuO₃ (10 nm)/ SrTiO₃ (001) substrate were investigated by using high-resolution transmission electron microscopy (HRTEM) analyses. Selected area electron diffraction (SAED) was also recorded in the zone axis of [100]. The chemical analysis and mapping at the nanometer level were performed via energy-dispersive x-ray spectroscopy (EDX). In detail, the cross-sectional samples were prepared for TEM observations. The PZT thin films were cut along the growth direction of [001] and mechanically polished down to about ~15 μm. For the electron transparency, the mechanically thinned sample was further Ar-ion milled (Gatan Precision Ion Polishing System, PIPS[®] II, Gatan, USA). The microstructural investigation was further carried out using transmission electron microscopy (TEM, TECNAI F20 S-TWIN, FEI, Netherlands) to identify the film structure. In TEM measurements, the sulfurized PZT film was fabricated by method A.

A.4 X-ray photoelectron spectroscopy measurements and analyses

X-ray photoelectron spectroscopy (XPS) was conducted using a K-Alpha⁺ XPS system (Thermo Fisher Scientific Inc., U.K) equipped with a monochromated Al Kα x-ray source ($h\nu = 1486.6$ eV) of spot size 400 μm. And charge compensation of the XPS samples was performed

during analysis. The carbon C 1s peak of hydrocarbon at the binding energy of 284.6 eV was used as a reference to make corrections of all the obtained spectra. The pure and sulfurized PZT films for XPS analyses were synthesized using method A.

A.5 Synchrotron x-ray diffraction measurements

Synchrotron x-ray diffraction (XRD) experiments were performed in the 3A beamline of Pohang Accelerator Laboratory (PAL). In the XRD measurements, a 6-circle x-ray goniometer was used for the XRD θ - 2θ scans and the reciprocal space mappings (RSMs) of pure and sulfurized PZT films. To obtain the in-plane and out-of-plane lattice constants of the pure and sulfur-doped PZT films, we carried out RSMs around the (103) Bragg peak of the SrTiO₃ (001) substrate. From the RSM measurements, a monoclinic-to-tetragonal structural transition was visualized with the increasing sulfur-doping concentration. To measure the Curie (T_C) temperature of the pure and sulfurized PZT films, XRD θ - 2θ scans around the (002) Bragg peak of the SrTiO₃ (001) substrate were also performed in a wide range of temperature from 300 to 770 K. By monitoring the temperature dependence of out-of-plane lattice constants in the pure and sulfurized PZT films, we extracted the T_C of a ferroelectric-to-paraelectric phase transition. We fabricated the pure and sulfurized PZT films for the room-temperature XRD analyses via method A. The PZT oxysulfide films with the controlled concentration of sulfur dopants were prepared by method B for the room-temperature RSMs.

A.6 Ferroelectric hysteresis measurements

The polarization (P)-electric field (E) hysteresis loops were obtained at room temperature using a ferroelectric tester (PRECISON LC Material Analyzer, Radiant Technologies, USA) by applying a triangular electric pulse with an amplitude of 10 V and frequency of 1 kHz to a ferroelectric capacitor. For ferroelectric hysteresis measurements, Pt top electrodes with a diameter

of 90 μm were deposited on pure and sulfurized PZT films using the direct current (DC) sputtering machine (Cressington 108, Cressington, Inc., U.S.A). The deposition of the Pt electrodes was performed at the pressure rate of 0.06 mbar under the argon environment. To investigate the sulfurization effect on ferroelectricity, we prepared the pure and sulfurized PZT films for the P - E hysteresis measurements via method A. To examine the sulfur doping-level dependence of ferroelectric hysteresis loops, we fabricated the PZT oxysulfide films with the controlled concentration of sulfur dopants via method B.

A.7 Piezoresponse force microscopy measurements

An atomic force microscopy (AFM) machine (NX-10; Park system) with the point probe plus electrostatic force microscopy (PPP-EFM) nano-sensors tip was used for piezoresponse force microscopy (PFM). The amplitudes and phase components of the as-grown pure and sulfurized PZT films were taken by applying DC bias of ± 7 V through a conductive tip. The pure and sulfurized PZT films for PFM measurements were fabricated by method A.

A.8 Ellipsometry measurements and analyses

The elliptic constants (Ψ and Δ) of the pure and sulfurized PZT films were measured using a spectroscopic ellipsometer (SE, Horiba-Jobin Yvon, Uvisel UV/NIR) with a photon energy range of 0.75 to 4.5 eV at an incident angle of 70° . SE data were analyzed by using the double new amorphous (DNA) dispersion formula with two oscillators. The pure and sulfurized PZT films for the ellipsometry analyses were prepared by method A.

A-9 Ellipsometry measurements of pure and sulfurized PZT films grown on SrRuO₃/SrTiO₃ (001) substrates fabricated by method A

The thicknesses and the optical constants of the pure and sulfurized PZT films synthesized by method A were measured by a spectroscopic ellipsometer (SE, Hobira-Jobin Yvon, Uvisel UV/NIR) with a photon energy range of 0.75–4.5 eV at an incident angle of 70°. The spectroscopic ellipsometer data for the films were analyzed via an optical model based on the Bruggeman effective medium approximation (BEMA). The optical model of the pure and sulfurized PZT films consisted of three layers: a surface layer, a film layer, and a substrate. The double new amorphous (DNA) dispersion formula, combined with two oscillators, was utilized to describe the dispersion in the optical constants of the films.

The measured ellipsometric data and best fit lines determined by the double new amorphous (DNA) dispersion formula of the pure and sulfurized PZT films are shown in the Figure A1(a) and (b). Ellipsometric parameters (ψ , Ψ and Δ) were recorded at an incidence angle of 70°. To obtain the optical constants of the pure and sulfurized PZT films, we used a three-layer model to represent the film system which consists of a surface layer, a film layer, and a substrate. The surface layer, introduced for improving the fit result, indicates roughness of the film and consists of PZT (50%) and void (50%). The film layer only has PZT, and SrRuO₃/SrTiO₃ substrate is treated as isotropic material with infinite thickness. To obtain the optical constants of the SrRuO₃/SrTiO₃ substrate, the ellipsometric parameters of both substrates were measured and used for fitting.

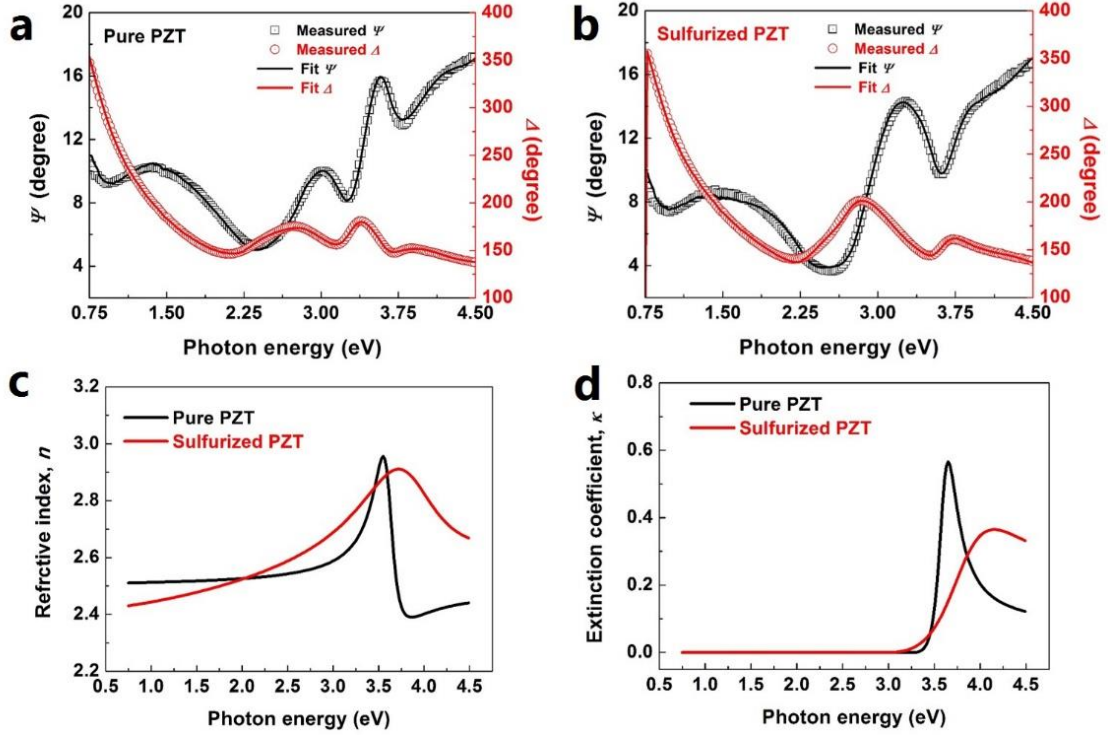


Figure A1. Spectroscopic ellipsometry data of pure PZT and sulfurized PZT films. (a) and (b) Comparison of the measured ellipsometric data (Ψ and Δ , open symbols) and best-fit lines obtained using the DNA dispersion formula: (a) pure PZT and (b) sulfurized PZT films. (c) Refractive indices and (c) extinction coefficients of pure PZT and sulfurized PZT films extracted from the ellipsometric data.

The DNA dispersion formula with two oscillators was utilized to describe the dispersion in the optical constants of the pure and sulfurized PZT films over the entire spectral range. The DNA formula is as follows [12,13]

$$n(\omega) = n_{\infty} + \sum_{j=1}^2 \frac{B_j(\omega - \omega_j) + C_j}{(\omega - \omega_j)^2 + \Gamma_j^2}, \quad (1)$$

$$\kappa(\omega) = \begin{cases} \sum_{j=1}^2 \frac{B_j(\omega - \omega_j) + C_j}{(\omega - \omega_j)^2 + \Gamma_j^2} & \omega > \omega_g, \\ 0 & \omega \leq \omega_g, \end{cases} \quad (2)$$

and

$$B_j = \frac{f_j}{\Gamma_j} \left(\Gamma_j^2 - (\omega_j - \omega_g)^2 \right), \quad (3)$$

$$C_j = 2f_j \cdot \Gamma_j (\omega_j - \omega_g) \quad (4)$$

where, n_∞ is the refractive index at high frequency, ω_g is the angular frequency related to the optical bandgap, f_j is the strength of the j th oscillator, ω_j is the resonance angular frequency of the j th oscillator, and Γ_j is the j th peak broadening. The fitting parameters of the pure and sulfurized PZT films grown on SrRuO₃/SrTiO₃ substrates are shown in Table A1. The unit of all parameters is eV except for n^∞ .

Table A1. Fitting parameters of the films grown on SrRuO₃/SrTiO₃ substrates.

Films	n^∞	ω_g	f_1	ω_1	Γ_1	f_2	ω_2	Γ_2
Pure PZT	2.491	3.276	0.065	3.606	0.119	0.000	7.726	4.783
Sulfurized PZT	2.558	3.000	0.097	3.809	0.509	0.330	2.639	4.536

The thicknesses of the pure and sulfurized PZT films were obtained 120 nm and 119 nm, respectively. The optical constant spectra of the films are displayed in Figures A1(c) and (d). The refractive index and extinction coefficient spectra of the films show a considerable change due to the sulfurization. The peaks of both spectra of sulfurized PZT film broaden compared with those of the pure PZT film, and the absorption edge shifts toward lower energy (Figure A1(d)). The direct band gap energies of the films were calculated using the extinction coefficient and are presented in Figure 7(a). The sulfurization process is found effective in reducing the band gap of the sulfurized PZT compared to pure PZT. The values of the pure and sulfurized PZT films are 3.41 and 3.32 eV, respectively.

A.10 Raman spectroscopy

Room-temperature Raman spectroscopy of pure and sulfurized PZT films was performed at a wavelength of 532 nm by using a conventional Raman spectrometer (LabRam HR800, Horiba, Co.). An optical microscope (BX41, Olympus) was used for measuring the spectrum at the backscattering geometry. The power of the laser was set to be of about 40 mW. The setup combined with a super-notch filter allowed us to measure Raman spectra in the 10–1200 cm^{-1} range. Diffraction grating for UV-NIR range was set at 1800 lines/mm. We synthesized the pure and sulfurized PZT films for the Raman measurement using method A.

A.11 Characterization of BNT–28ST/BNKT ceramic composites

The crystal structure of NBiT15 particles, plate-type BNKT particles, and sintered composite ceramics were determined using an x-ray diffractometer (XRD, Ultima4, Rigaku, Japan) with Cu radiation. Field-emission scanning electron microscope (FE-SEM, JSM6500F, Jeol, Japan) imaging was used to study the surface morphology. The surfaces of all samples were polished and thermally etched at 1050 °C for 1 h to get good quality morphology images. Ferroelectric properties were measured using a Sawyer–Tower circuit, and strain measurements were performed using a linear variable differential transducer (LVDT, MCH-331 & M401, Mitutoyo, Japan). The bipolar and unipolar strain hysteresis loops were measured at the frequency of 0.2 Hz at room temperature.

A.12 Computational Method

We used the Vienna Ab Initio Simulation Package (VASP), for density functional theory (DFT) calculations. The generalized gradient approximation (GGA) within Perdew-Burke-Ernzerhof (PBE) parameterization is used for the electron-electron exchange correlations, and the projector augmented wave (PAW) method is used for ion-electron interactions [%%]. Cutoff

energy of 540 eV is considered for the plane-wave expansion of the electronic eigenfunction. The Brillouin zone was sampled with Monkhorst Pack k-point mesh of $15 \times 15 \times 9$ and $15 \times 15 \times 7$ in the case of a unit cell and reduced to $2 \times 4 \times 4$ and $5 \times 5 \times 3$ in the case of supercells, for 4H SrMnO₃ and 6H SrMnO₃ respectively. The force and total energy criteria used for structure full relaxation are 0.001 eV/Å and 10^{-8} eV, respectively. To have an equal number of the atom and homogeneous Sr-deficiencies, $3 \times 2 \times 1$ and $2 \times 2 \times 1$ supercells are constructed for the 4H and 6H SrMnO₃, respectively.

A.13 Characterization of pure, Al-doped SrMnO₃ ceramics

The crystalline structure of pure, Al-doped SrMnO₃ and Sr-deficient SrMnO₃ ceramic samples was identified by x-ray diffractometer (Cu K α_1 , X'pert PRO MRD, Philips) at room temperature. A field emission scanning electron microscope (FE-SEM, JSM-7600, JEOL, Japan) with an EDS detector was used to visualize the surface morphology and analyze the chemical stoichiometry of the as-sintered pure and Al-doped SrMnO₃ ceramics. The Raman spectrums were taken at room temperature at 473 nm light excitation source. The spot size of the laser was about 5 μ m. A ~50 cm focal length spectrometer (Dongwoo Optron, MonoRa501i) equipped with an 1800 lines/mm grating was used to analyze the light scattered from the sample and detected by a thermoelectric cooled CCD detector (ANDOR iDus, DU420A).

Appendix B: Manual for x-ray diffraction techniques in the beamline of the Pohang Accelerator Laboratory

B.1 Reciprocal Space Mapping (RSM) in the 3A-beamline in PAL.

B.1.1 "Half cut" and "zero-align"

(1) Initializing theta, delta, and chi motor positions.

```
uan 0 0: umv chi 90
```

(2) Sample loading.

(3) Counting the total number of photons of the direct beam entering the detector.

```
wmvr shold -1: ct (In this case, the obtained beam count becomes the maximum value.)
```

(4) Direct beam, align on a straight line of the detector and set the zero point.

```
lup del -.1 .1 20 1; umv del CEN; set del 0
```

```
set-dial del 0
```

(5) "Half-cut" so that half of the beam can pass through the sample.

```
ascan should -1 .5 30 1: umv shold half_intensity; ct
```

(sample stage in the z-direction, increase it little by little and repeat it until the beam count reaches half of the maximum value).

(6) Zero alignment between the sample and the beam.

(Beam and sample are parallel so that as many beams pass as possible).

```
lup th -1 1 30 1 [press enter]
```

```
umv th pl_xMAX [press enter]
```

```
set th 0; set-dial th 0 [press enter]
```

ct [Enter] (Check "half-cut", make sure that the beam count is half of the maximum value).

setlat [Enter] {to give the lattice parameters and angles (alpha, beta and gamma) information (unit cell) to a computer, eg SrTiO₃ (STO) substrate is cubic having a = b = c = 3.905 and angles = 90 all}.

B.1.2 Out-of-plane alignment [Bragg's peak (002) alignment of the substrate]

(1) (002) Calculation and shift of substrate peak

ca 0 0 2 [(002) delta, theta, chi, phi values for Bragg peak].

uan 46.5232 23.3633: umv chi 90

[If you hit ubr 0 0 2, delta, theta, chi, phi are automatically moved to the calculated position].

(2) (002) Precise alignment of the substrate peak

lup del -1 1 30 0.5

umv del CEN (detector alignment)

lup th -1 1 30 0.5

umv th CEN (sample alignment)

lup chi -1 1 30 0.5

umv chi CEN (chi alignment)

lup del -1 1 30 0.5

umv del CEN [It is better to finish the last scan for alignment with a detector scan].

(3) Re-memorize the aligned current position as a calculated value

set del 46.5232; set_dial del 46.5232

(Aligned delta value is displayed as a calculated value.)

set th 46.5232 / 2 [theta value is delta, It should be half of the value].

set-dial th -46.5232/2 [I'm not sure why, but for theta, in hardware].

The value in the software is memorized with the opposite sign.)

set chi 90; set-dial chi 90 [Remember the aligned chi value, (002) In the case of the Bragg plane, the chi value is 90 degrees because it is parallel to the lattice plane].

or0 (The current position is $(hkl) = (002)$ peak of the engine)

Pa [(002) Check the aligned result].

B.1.3 Out-of-plane and in-plane alignment [(103) Bragg peak align of the substrate]

(1) (103) Calculation and shift of the peak

cal 1 0 3 [(103) The 2θ , θ , χ , and ϕ values for the Bragg peak can be found].

ubr 1 0 3 (Go to the calculated (103) Bragg peak below.)

(2) (103) precise alignment of the peak

lup del -0.1 0.1 30 0.3

umv del CEN (detector alignment)

umv th CEN/2 [(002) After aligning, θ is half of 2θ separately, sample alignment can be done by moving θ motor, but in this case, θ is slightly different from half of 2θ , so there is a difficulty of recognizing θ as half of 2θ].

lup chi -0.5 0.5 30 0.3

umv chi CEN (chi align)

lup phi -0.5 0.5 30 0.3

umv phi CEN

lup del - 0.1 0.1 30 0.3

umv del CEN

umv th CEN/2

[It is better to finish the last scan for alignment with a detector scan].

(3) Re-memorize the aligned current position as the calculated value.

set phi 0; set-dial phi 0

or1 (Recognizes that the current position is (hkl) = (103) peak.)

B.3.3 Specifying Scan Area and Performing RSM

(1) Determining the RSM measurement range.

cal 0.95 0 2.65 (Check the position to start hkimesh with "cal" command.)

cal 1.05 0 3.1 (Check the position to end hkimesh with "cal" command.)

For each position delta, theta, chi, phi) It is important to check the value and make sure that it is within the limit, if it is out of range, the motor may collide with the inlet where the beam is injected and the RSM may not be properly performed.)

(2) Determine the RSM measurement mode.

setmode [Enter]

freeze [Enter] (Confirm the selected current mode)

(3) Measure RSM.

fi0000

Publication List

[1] “Stabilization of 6H-hexagonal SrMnO₃ polymorph by Al insertion”

M. Sheeraz, H. J. Lee, A. Ali, M. U. Rasheed, F. Akram, J. S. Choi, J.-S. Bae, Y.-H. Shin, Y. S. Kim, C. W. Ahn, and T. H. Kim

(In preparation 2020)

[2] “Constructing polymorphic nanodomains in BaTiO₃ films via epitaxial symmetry engineering”

W. Peng, J. A. Zorn, J. Mun, **M. Sheeraz**, C. J. Roh, J. Pan, B. Wang, K. Guo, C. W. Ahn, Y. Zhang, K. Yao, J. S. Lee, J.-S. Chung, T. H. Kim, L.-Q. Chen, M. Kim, L. Wang, and T. W. Noh
Adv. Funct. Mater. 1910569 (2020).

[3] “Enhanced ferroelectricity in perovskite oxysulfides”

M. Sheeraz, H. J. Kim, K.-H. Kim, J.-S. Bae, A. Y. Kim, M. Kang, J. Lee, J. Song, A. Khaliq, J. Kim, B.-G. Cho, S.-Y. Joe, J. H. Jung, J.-H. Ko, T. Y. Koo, T. W. Noh, S. Cho, S. Lee, S. M. Yang, Y.-H. Shin, I. W. Kim, C. W. Ahn, and T. H. Kim
Phys. Rev. Mater. **3**, 084405 (2019).

[4] “Stress driven high electrostrain at low field in incipient piezoelectrics”

M. Sheeraz, A. Khaliq, A. Ullah, H.-S. Han, A. Khan, A. Ullah, I. W. Kim, T. H. Kim, C. W. Ahn
J. Eur. Ceram. Soc. **39**, 4688 (2019).

[5] “Effect of ceramic-target crystallinity on metal-to-insulator transition of epitaxial rare-earth nickelate films grown by pulsed laser deposition”

J. S. Choi, **M. Sheeraz**, J.-S. Bae, J. H. Lee, J. Lee, J. Lee, S. Lee, H. Jeon, Y. S. Oh, C. W. Ahn, and T. H. Kim

ACS Appl. Electron. Mater. **1**, 1952 (2019).

(1st author equal contribution)

[6] “Polymorphic phase transition in BaTiO₃ by Ni doping”

N. X. Duong, J.-S. Bae, J. Jeon, S. Y. Lim, S. H. Oh, A. Ullah, **M. Sheeraz**, J. S. Choi, J.-H. Ko, S. M. Yang, K.-H. Kim, I. W. Kim, C. W. Ahn, T. H. Kim
Ceram. Int. **45**, 16305 (2019).

[7] “Giant room-temperature electrostrictive coefficients in lead-free relaxor ferroelectric ceramics by compositional tuning”

A. Ullah, H. B. Gul, A. Ullah, **M. Sheeraz**, J.-S. Bae, W. Jo, C. W. Ahn, I. W. Kim, and T. H. Kim
Appl. Mater. **6**, 016104 (2018).

Patent List

[1] “화학적 용해법에 기반한 황이온 치환 기술”

김태헌 (Tae Heon Kim), 안창원 (Chang Won Ahn), 김일원 (Ill Won Kim), 시라즈 무하마드 (Muhammad Sheeraz)

등록번호 : 특허 제 2137238 호

등록일 : 2020-07-17

[2] “알루미늄 이온 치환된 스트론튬 망간 산화물에 의한 6H-육방정계 대칭구조를 갖는 스트론튬 망간 산화물의 합성방법”

김태헌 (Tae Heon Kim), 안창원 (Chang Won Ahn), 시라즈 무하마드 (Muhammad Sheeraz),

이호정 (Ho Jeong Lee)

(Submitted)

Acknowledgments

First of all, I would like to express my profound gratitude to **Professor Tae Heon Kim** for offering me a Ph.D. position in his research group. I wish to thank **Prof. T.H. Kim** for his supervision both academically and morally. **Prof. T.H. Kim** extensive knowledge in the condensed matter physics was an inspiration to me, his endless support and continuous guideline means a lot to me and help me to complete my doctorate (Ph.D.) degree successfully.

I would like to acknowledge the Research Professors, **Prof. Kim Ill Won**, and **Dr. Chang Won Ahn** for their continuous help and suggestions during the past four years. **Dr. C.W. Ahn's** experimental expertise in the oxides materials helps me to design experiments and then performing a systematic characterization.

I would like to extend my heartiest gratefulness to all colleagues in the Quantum Materials Laboratory at the department of physics for their contribution, discussion, and providing a friendly environment in the lab; **Dr. Bong Chan Park, Dr. Fazli Akram, Mr. Nguyen Xuan Duong, Mr. Jin San Choi, Mr. Jae Hun Jo, Mr. Yong Jin Jo, Mr. Ho Jeong Lee, Ms. Nguyen Bich Thuy, and Mr. Hawn Min Kim.** I want to give my appreciation to all the Professors and staff members at the Department of Physics for helping me both academically and officially.

Of course, special thanks to the University of Ulsan for offering me a Brains Korea (BK-21) plus, a scholarship for extending financial support. My entire research study was supported by the National Research Foundation of Korea (NRF) grants funded by the government of the Republic of Korea.

I humbly extend my regards to all the Pakistan community members at the University of Ulsan, especially, **Dr. Sheraz Ali Khan, Dr. Saeed Ahmad, Dr. Hurmat Ali Shah, Dr. Farman Ullah, Dr. Abdus Samad, Dr. Sana Ullah Jan, Dr. Usman Yaqoob, Dr. Fazli Akram, Mr. Zeeshan Tahir, Mr. Abdul Khaliq, Mr. Asad Ali, Mr. Mamoon Ur Rasheed, Mr. Zahoor**

Ahmad, and Mr. Umer Saeed for their care, moral support, and help in the entire doctorate (Ph.D.) time.

Most importantly, I want to thank my parents (Daji and Ami) for their love, support, guidance, and encouragement throughout my education life. My brothers (**M. Shahzad Siddique and M. Farooq Siddique**), sisters (**Tahira Siddique and Haseeba Siddique**), aunts (Specially **Shagul**), uncles, and cousins deserve my wholehearted thanks as well. I could not have done this without the love and care of my whole family.

Muhammad Sheeraz